STUDYING COSMOLOGICAL SOURCES OF GRAVITATIONAL WAVES

by

Vincent Dominique André Corbin

A dissertation submitted in partial fulfillment
of the requirements for the degree

of

Doctor of Philosophy

in

Physics

MONTANA STATE UNIVERSITY
Bozeman, Montana

August, 2010

APPROVAL

of a dissertation submitted by

Vincent Dominique André Corbin

This dissertation has been read by each member of the dissertation committee and has been found to be satisfactory regarding content, English usage, format, citations, bibliographic style, and consistency, and is ready for submission to the Division of Graduate Education.

Dr. Neil Cornish

Approved for the Department of Physics

Dr. Richard Smith

Approved for the Division of Graduate Education

Dr. Carl A. Fox

STATEMENT OF PERMISSION TO USE

In presenting this dissertation in partial fulfillment of the requirements for a doctoral degree at Montana State University, I agree that the Library shall make it available to borrowers under rules of the Library. I further agree that copying of this dissertation is allowable only for scholarly purposes, consistent with "fair use" as prescribed in the U.S. Copyright Law. Requests for extensive copying or reproduction of this dissertation should be referred to ProQuest Information and Learning, 300 North Zeeb Road, Ann Arbor, Michigan 48106, to whom I have granted "the exclusive right to reproduce and distribute my dissertation in and from microform along with the non-exclusive right to reproduce and distribute my abstract in any format in whole or in part."

Vincent Dominique André Corbin

August, 2010

DEDICATION

To my parents, for all they have done for me,
and to Jacky, who helped me understand so many things.

"L'adulte est un grand enfant qui croit qu'il sait
l'enfant est un petit adulte qui sait qu'il croit"
Fabien Marsaud

The adult is a great child who believes he knows,
the child is a small adult who knows he believes.

ACKNOWLEDGEMENTS

I have been influenced and inspired by many great teachers throughout my 25 years as a student. They have guided me to where I stand today, and I am deeply grateful to all of them.

I would like to thank my thesis advisor, Dr Neil Cornish, who taught me to become a physicist. During my graduate student years he helped me approach the challenges of learning and research, as a teacher and an advisor. By showing great tolerance and understanding he allowed me to remain independent in my research, and he gave me the time and resources to find my own way. I am also appreciative of my committee for being patient during the process of writing my thesis, in particular Dr Carla Riedel for all her positive comments and encouragement. I also would like to thank my undergraduate advisor, Dr Joseph Dwyer, who was the first to reveal how exciting physics can be, both in the classroom and in the laboratory. His teaching and work ethic remain a model for me. I am thankful to my peers Harsh, Laura, Patricia, Silvina, Mehmet and all the students of my incoming year for their precious friendship and collegiality. I am grateful for Dr Jacqueline Hewitt and Dr David Fouchard in reviewing my thesis.

Mes pensées vont aussi aux instituteurs de l'école Saint-Michel à la Haye-Pesnel, qui dès mon plus jeune âge ont su éveiller en moi la curiosité nécessaire pour devenir un chercheur. En particulier, je tiens à remercier Mlle Bellanger pour avoir fait preuve d'une extrême patience, et pour avoir toujours cru en moi. Enfin, un grand merci a ma famille et mes amis pour leurs conseils et leur soutien. Ils ont toujours été présents quand j'en ai eu le plus besoin, et bien que loin de mon pays pendant toutes ces années, grâce à eux, je n'ai jamais été seul.

TABLE OF CONTENTS

TABLE OF CONTENTS – CONTINUED

LIST OF TABLES

Table Page

LIST OF FIGURES

Figure Page

LIST OF FIGURES – CONTINUED

Figure Page

LIST OF FIGURES – CONTINUED

Figure Page

ABSTRACT

This dissertation presents two aspects of the study of cosmology through gravitational waves. The first aspect involves direct observation of past eras of the Universe's formation. The detection of the Cosmic Microwave Background Radiation was one of the most important cosmological discoveries of the last century. With the development of interferometric gravitational wave detectors, we may be in a position to detect its gravitational equivalent in this century. The Cosmic Gravitational Background is likely to be isotropic and stochastic, making it difficult to distinguish from instrument noise. The contribution from the gravitational background can be isolated by cross-correlating the signals from two or more independent detectors. Here we extend previous studies that considered the cross-correlation of two Michelson channels by calculating the optimal signal to noise ratio that can be achieved by combining the full set of interferometry variables that are available with a six link triangular interferometer. We apply our results to the detector design described in the Big Bang Observer mission concept study and find that it could detect a background with $\Omega_{gw} > 2.2 \times 10^{-17}$.

The second aspect consists in studying astrophysical sources that detain crucial information on the Universe's evolution. We focus our attention on black holes binary sytems. These systems contain information on the rate of merger between galaxies, which in turn is key to unlock the mystery of inflation. Pulsar timing is a promising technique for detecting low frequency sources of gravitational waves, such as massive and supermassive black hole binaries. Here we show that the timing data from an array of pulsars can be used to recover the physical parameters describing an individual black hole binary to good accuracy, even for moderately strong signals. A novel aspect of our analysis is that we include the distance to each pulsar as a search parameter, which allows us to utilize the full gravitational wave signal. This doubles the signal power, improves the sky location determination by an order of magnitude, and allows us to extract the mass and the distance to the black hole binary.

CHAPTER 1

INTRODUCTION

Physics strives to explain how the Universe functions on every scale, from the mechanisms dictating the behaviour of the tiniest particle to the ones ruling the largest astrophysical objects. One particular question remains puzzling to scientists: how did everything start? What happened at the beginning of time to create the Universe that we see today? For this reason the field of cosmology has been attracting a lot of attention in the past few decades.

Today the Big Bang theory is widely accepted as providing the best description of the birth of the Universe. However, very little is known about the fractions of seconds that followed this fundamental explosion. Experiments in particle physics and observation of astrophysical structures yielded a roughly sketched theory that divides the evolution of the Universe from the Big Bang to the present days into epochs (figure 1.1).

- Quantum gravity epoch ($0 - 10^{-43}\,sec$): the Universe is extremely hot and confined. The spacetime structure seethed with quantum fluctuations.. All the forces (i.e. gravity, strong force, weak force and electromagnetism) are still unified (figure 1.2).
- Grand unification epoch ($10^{-43} - 10^{-35}\,sec$): gravity is dissociated from the other forces. Inflation takes place and the Universe expands very rapidly. As a consequence, the large anisotropies of the previous epoch are erased, to be

replaced by smaller quantum fluctuations that occured during inflation and got imprinted as classical density variations at the end of inflation, which will allow for their observation by telescopes.

- Electroweak or quark epoch ($10^{-34} - 10^{-10}\, sec$): the strong force decouples from the electroweak force. The Universe becomes a hot "soup" of quarks.
- Lepton epoch ($10^{-12} - 10^{2}\, sec$): this epoch begins with the separation of the weak and electromagnetic forces. The Universe is now cold enough for the quarks to be confined to form protons and neutrons.
- Nucleosynthesis ($1\, sec - 17\, min$): the protons and neutrons start binding with each others creating deuterium. Then as the temperature decreases, the deuterium becomes stable enough for the synthesis of helium to occur, followed by lithium and beryllium. No element heavier than beryllium is created during nucleosynthesis as the temperature falls below the threshold required for nuclear fusion.
- photon epoch ($100\, sec - 379000\, years$): the Universe is then a dense plasma of nuclei created by nucleosynthesis, electrons and photons. The energy is dominated by the photons. The end of the photon epoch is referred to as the surface of last scattering (SLS). Around 379000 years after the big bang, the lower temperature of the Universe implies photons do not interact as frequently with matter. They can therefore "escape" without being constantly reabsorbed by matter.

- atom and galaxy epoch ($379000\,years - today$): electrons combine with nuclei to form neutral atoms. This process is called recombination. The newly formed matter is attracted in larger scale structures, eventually forming stars and galaxies ($\sim 1\,billion\,years$).

The timeframe of the different epochs is only a rough estimation, and many pieces of the puzzle are missing. In particular the earliest stages of the evolution, such as inflation and the quantum gravity epoch, remain for the greatest part a mystery.

So far, standard astronomy (i.e. astronomy based on the observation of light) has made great contribution to the field of cosmology. By observing deep into space, it has been possible to detect electromagnetic waves emitted long ago, and as such to "look" a long way back in time, into the origin of the Universe. In 1964 Robert Wilson and Arno Penzias revolutionized cosmology, when they first detected the cosmic microwave background (CMB). The CMB is composed of electromagnetic waves (i.e. microwaves) emitted at the surface of last scattering, about 379000 years after the big bang. It is almost isotropic but small anisotropies, which are relic of quantum fluctuations from inflation, have been observed. The discovery of the CMB was thus a direct observation of the SLS, and a strong argument in favour of inflation.

Astronomy has also made indirect contributions to the field of cosmology. The study of astrophysical phenomena has given clues about the different stages of the Universe. For example, the precise measurement of the composition of stars has allowed

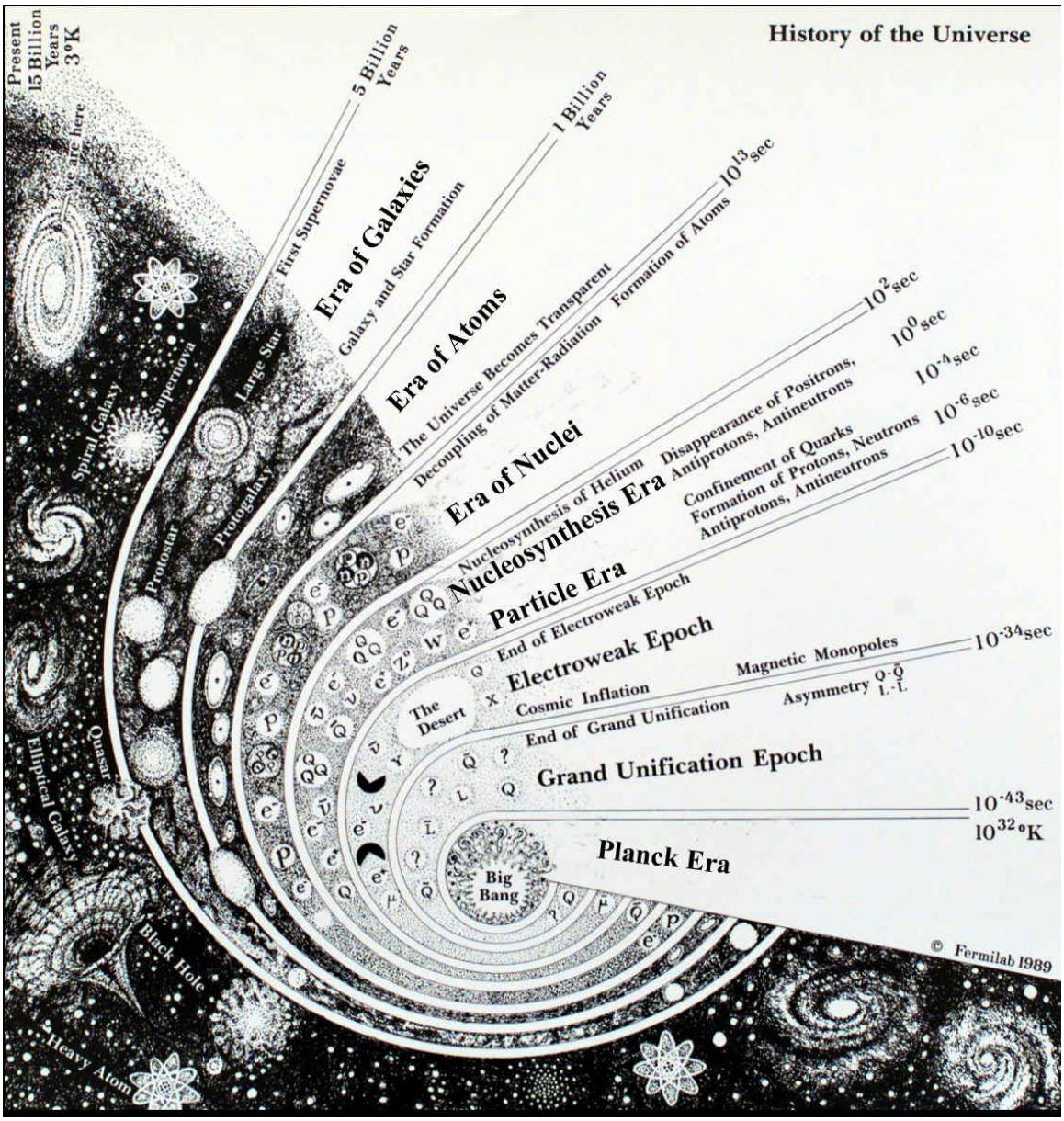

Figure 1.1: This figure describes the different stages or epochs the Universe underwent from the big bang to present days. As time increases, the Universe expands, and its temperature decreases (From R. U. Buehler,http://www.hgb-leipzig.de/weltbilder/)

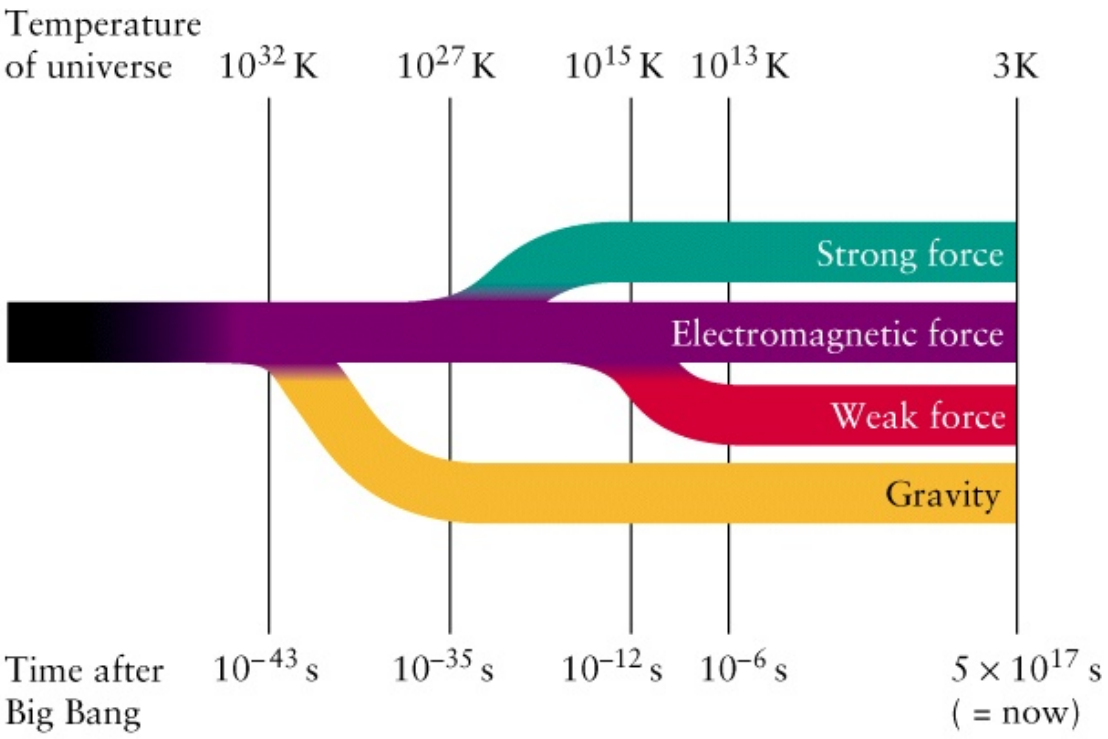

Figure 1.2: The dissociation of the 4 fundamental forces (gravity, strong force, weak force, and electromagnetism) from each other is shown as a function of time and temperature (www.williams.edu)

for the determination of the initial density ratio of early elements (e.g. deuterium, helium), and thus for a better understanding of nucleosynthesis.

Traditional astronomy is however limited by the fact it relies on the detection of electromagnetic waves. It is impossible for telescopes to look back past the surface of last scattering, where photons started to escape from matter without being reabsorbed. Hence, the CMB is composed of the oldest photons present in the Universe. A direct observation of an event predating SLC is therefore impossible with telescopes aimed at detecting electromagnetic waves. Furthermore, some of the most interesting astrophysical objects, which potentially contain crucial information about the genesis of the Universe, do not emit light. Dark matter and black holes belong to this category, and are both very important for cosmology. Dark matter, which accounts for most of the matter in the Universe, is a crucial aspect of cosmology. Black holes may hold the key to understanding the formation of the Universe. In particular, it is now known that massive black holes are located at the centre of galaxies. When two galaxies merge, their respective central black holes can form a binary system and orbit around each other. To detect and study such binaries would give a clear idea of the population and frequency of occurrence of galaxy mergers, which in turn would place constraints on the different theories of cosmology.

Fortunately, in the past decades, a new type of astronomy has been proposed, which relies on the detection of gravitational waves instead of electromagnetic waves. Gravitational waves are ripples propagating through spacetime, and are created by

matter (for a description of gravitational waves see chapter 3). One of their properties is their extremely weak interaction with matter. This is both a blessing and a curse, as it implies that gravitational waves have freely propagated through space without being absorbed and are still present for us to observe and study; it also means they are extremely difficult to detect. Furthermore, due to their strong gravitational field, black hole binaries are major sources of gravitational waves. Other exotic objects, such as cosmic strings which are possible consequences of inflation, are potential sources of gravitational waves, relevant to the exploration of the beginning of time. Gravitational wave astronomy is therefore an ideal tool to study cosmology.

This thesis focuses on determining the potential of gravitational wave astronomy for the study of two particular sources: the cosmic gravitational background, which is formed by relic gravitational radiation from early stages of the Universe and in particular inflation, and massive black hole binaries. It is organized as follows: chapter 2 is a review of the physics leading to gravitational radiation and of the different apparatuses that have been proposed and constructed to detect them. A derivation of the effect of gravitational waves on a photon travelling between two points in space is also outlined. A description of the cosmic gravitational background is given in chapter 3, while in chapter 4 an optimal strategy to detect it is laid out, which leads to the calculation of the lowest energy density that could be detected by the Big Bang Observer. Chapter 5 derives the gravitational waveform produced by a general mass distribution, and applies it specifically to binary systems. Chapter 7 is dedicated to

the analysis of gravitational waves radiated by massive black hole binaries. A novel approach to the analysis is presented, which leads to a major improvement in the potential characterization of massive black hole binary systems with pulsar timing arrays.

This thesis follows Einstein's convention on the summation of tensor indices; therefore a summation over up and down repeating indices (e.g. $A^{\mu}B_{\mu}$) is implied. Also natural units are used (i.e. the speed of light c and the gravitational constant G equal unity).

CHAPTER 2

GRAVITATIONAL WAVES AND DETECTORS

2.1 Introduction

In order to study and detect gravitational waves, one first needs to understand their origin. Gravitational waves do not follow from a theory complementary to general relativity - they are in fact an inherent part of the theory of Einstein. General relativity cannot exist in its current form without the existence of gravitational waves. To understand their properties and origin, we need to look into the fundamentals of general relativity. The core of general relativity is contained in the Einstein equations:

$$G^{\mu\nu} = 8\pi T^{\mu\nu} \,. \tag{2.1}$$

$T^{\mu\nu}$ is the stress-energy tensor. It is a description of matter. More precisely, it contains information about density and flux of energy and momentum in spacetime. It describes the source of the gravitational field. $G^{\mu\nu}$, often called Einstein tensor, is an attribute of the curvature of spacetime. It is given in term of Ricci tensor $R^{\mu\nu}$ and the metric $g^{\mu\nu}$ by

$$G^{\mu\nu} = R^{\mu\nu} - \frac{1}{2} g^{\mu\nu} R \,. \tag{2.2}$$

The Ricci tensor and its contraction, the Ricci scalar, are functions of the Christoffel symbols,

$$R^{\mu\nu} = \partial_\alpha \Gamma^\alpha_{\mu\nu} - \partial_\nu \Gamma^\alpha_{\mu\alpha} + \Gamma^\alpha_{\beta\alpha} \Gamma^\beta_{\mu\nu} - \Gamma^\alpha_{\beta\nu} \Gamma^\beta_{\mu\alpha} \tag{2.3}$$

and

$$R = g^{\mu\nu} R_{\mu\nu} \,, \tag{2.4}$$

which depend themselves on the first derivative of the metric:

$$\Gamma^{\alpha}_{\mu\nu} = \frac{1}{2} g^{\alpha\beta} \left(\partial_\nu g_{\mu\beta} + \partial_\mu g_{\nu\beta} - \partial_\beta g_{\mu\nu} \right) \,. \tag{2.5}$$

The Einstein tensor is a function of the metric and its first and second derivatives. It contains therefore all the information on the geometry of spacetime. The Einstein equations are ten non-linear differential equations. They are then very complicated to solve, and analytical solutions have only been found for a few particular and simple cases. Gravitational waves are simply a solution to the Einstein equations. This is best illustrated in the weak gravitational field approximation.

2.2 Weak Gravitational Fields

When one travels far enough from any strong gravitational source, the gravitational field will become almost null, and the spacetime will consequently be almost flat, or Minkowskian. This is to say we can describe spacetime with a "flat" metric $\eta_{\mu\nu}$ on which we add a small perturbation $h_{\mu\nu}$. The metric takes the form

$$g_{\mu\nu} = \eta_{\mu\nu} + h_{\mu\nu} \,, \tag{2.6}$$

where there exists a coordinate system in which $h_{\mu\nu} \ll 1$. The weak gravitational theory has a lot of symmetries. First, it is gauge invariant, as long as the local transformations are infinitesimal, as will be demonstrated here. The gauge transformations

are transformations of coordinates:

$$x'^{\mu} = x^{\mu} + \xi^{\mu}(\vec{x})\,. \tag{2.7}$$

To the lowest order in the derivatives of $\xi^{\mu}(x)$, the metric remains the same,

$$g_{\mu'\nu'} = \eta_{\mu'\nu'} + h_{\mu'\nu'}\,, \tag{2.8}$$

where the prime indicate by convention a new coordinate system. The perturbation term in the new coordinate system can be expressed in term of the perturbation in the old coordinate system as

$$h_{\mu'\nu'} = h_{\mu\nu} - (\partial_{\mu}\xi_{\nu} + \partial_{\nu}\xi_{\mu})\ . \tag{2.9}$$

If the derivatives of $\xi^{\mu}(x)$ are small enough (of the same order as $h_{\mu\nu}$), then the metric equations retain the same structure, and is indeed invariant under gauge transformations. Another symmetry of the system is shown through its invariance under finite Poincare transformation (translation, and Lorentz transformation). The perturbation transforms as a tensor under Lorentz transformation and remains small:

$$h_{\mu'\nu'} = \Lambda^{\alpha}_{\mu'}\Lambda^{\beta}_{\nu'}h_{\alpha\beta}\,. \tag{2.10}$$

Extensive use of these symmetries will be made in order to simplify Einstein equations. Since the derivatives of the flat part of the metric are null, the Ricci tensor can be given solely in terms of the perturbation:

$$R_{\mu\nu} = \frac{1}{2}\left(\partial_{\mu}\partial^{\alpha}h_{\alpha\nu} + \partial_{\nu}\partial^{\alpha}h_{\alpha\mu} - \partial_{\mu}\partial_{\nu}h^{\alpha}{}_{\alpha} - \partial^{\alpha}{}_{\alpha}h_{\mu\nu}\right)\ . \tag{2.11}$$

Equation 2.11 could then be plugged into equation 2.2 in order to find the Einstein equations as a function of the perturbation. It would yield, however, an unnecessarily complicated expression. Instead, in an attempt to simplify the notation, the trace reverse tensor is defined as

$$\bar{h}_{\mu\nu} = h_{\mu\nu} - \frac{1}{2}\eta_{\mu\nu}h\,. \tag{2.12}$$

h is simply the contraction $h^{\alpha}{}_{\alpha}$. The trace reverse tensor still satisfies $\bar{h}_{\mu\nu} \ll 1$. The Einstein tensor can now be written in a more compact manner:

$$G_{\mu\nu} = -\frac{1}{2}\left[\partial^{\alpha}\partial_{\alpha}\bar{h}_{\mu\nu} + \eta_{\mu\nu}\partial^{\alpha}\partial^{\beta}\bar{h}_{\alpha\beta} - \partial^{\alpha}\partial_{\nu}\bar{h}_{\mu\alpha} - \partial^{\alpha}\partial_{\mu}\bar{h}_{\nu\alpha}\right]\,, \tag{2.13}$$

where the higher order terms were dropped. Even after introducing the trace reverse tensor, equation 2.13 is not particularly enlightening. It is now time to make good use of the symmetries of the system. It can be shown [2, 3], that there always exists a vector ξ_{μ} such that the gauge transformation associated with it (eq. 2.7) will lead to $\partial^{\nu}\bar{h}_{\mu\nu} = 0$. This particular choice of coordinates is called the Lorentz gauge. Under this convenient choice of gauge, the Einstein equations greatly simplify:

$$\partial^{\alpha}\partial_{\alpha}\bar{h}_{\mu\nu} = 16\pi T_{\mu\nu}\,. \tag{2.14}$$

When matter is not present, equation 2.14 reduces to

$$\frac{\partial^2}{\partial t^2}\bar{h}^{\alpha\beta} = \nabla^2\bar{h}^{\alpha\beta}\,, \tag{2.15}$$

which is the well-known three dimensional wave equation. Plane waves (eq. 2.16) are solutions to the equations, and since they form a complete basis, all solutions can be

expressed as a superposition of plane waves.

$$\bar{h}^{\mu\nu} = A^{\mu\nu} e^{ik_\mu x^\mu} \text{ with } \eta^{\mu\nu} k_\mu k_\nu = 0\,. \tag{2.16}$$

The dispersion equation leads to $\omega^2 = |\tilde{k}|^2$ where ω is the time component of the wave four-vector k^μ, and $\tilde{k}$ its spatial components. The wave group and phase velocity are equal to unity. The wave propagates at the speed of light.

To understand the effects of the gravitational wave on test particles, we want to choose the best gauge available. To do so, we first notice that the coordinate transformation required to satisfy the conditions of the Lorentz gauge, $\partial^\nu \bar{h}_{\mu\nu} = 0$, is not unique. Those conditions are conserved under any additional coordinate transformation satisfying

$$\eta_{\mu\nu} \partial^\mu \partial^\nu \xi_\mu = 0\,. \tag{2.17}$$

Hence, the transformation vector ξ^μ only needs to satisfy the wave equation itself, which can be achieved with arbitrary amplitude. A specific value for the time component of the amplitude vector can be chosen to further fix the gauge so that the trace of the perturbation tensor in the new coordinate system vanishes, or equivalently the contraction of the amplitude tensor of the plane wave vanishes:

$$A^\alpha{}_\alpha = 0\,. \tag{2.18}$$

This also implies that the perturbation tensor becomes its own trace reverse tensor:

$$\bar{h}^{\mu\nu} = h^{\mu\nu}\,. \tag{2.19}$$

The spatial component of the transformation amplitude can still be freely chosen. This can be done in such a way that $h_{0i} = 0$. This together with the Lorentz condition, $\partial^\nu \bar{h}_{\mu\nu} = 0$, means

$$h_{0\alpha} = 0\,. \tag{2.20}$$

To summarize, the symmetries of the spacetime have been used to choose a convenient coordinate system, in which the following properties are satisfied:

$$h_{0\mu} = 0 \tag{2.21}$$

$$h^i{}_i = 0 \tag{2.22}$$

$$\partial^j h_{ij} = 0\,. \tag{2.23}$$

This particular choice of coordinates is called the transverse-traceless gauge (TT-gauge). If one consider a wave propagating in the $\hat{z}$-direction in the reference frame defined by the TT-gauge (i.e. $k^i = k\hat{z}$), then equation 2.23 yields

$$A_{iz} = 0\,. \tag{2.24}$$

Together wit $h^i{}_i = 0$ and the required symmetry of the tensor (i.e. $h_{\mu\nu} = h_{\nu\mu}$), it is found that the amplitude tensor of the wave can be represented by the matrix

$$A^{TT}_{\mu\nu} = \begin{pmatrix} 0 & 0 & 0 & 0 \\ 0 & A_{xx} & A_{xy} & 0 \\ 0 & A_{xy} & -A_{xx} & 0 \\ 0 & 0 & 0 & 0 \end{pmatrix}. \tag{2.25}$$

A_{xx} and A_{xy} are the amplitudes of the two polarization modes of the gravitational wave. To best understand this, one considers two test particles at rest in the frame defined by the TT-gauge. They are infinitesimally close to each other, and separated only in the $\hat{x}$-direction:

$$\begin{aligned} \vec{x}_0 &\rightarrow (0,0,0,0) \\ \vec{x}_1 &\rightarrow (0,\epsilon,0,0)\,. \end{aligned} \tag{2.26}$$

Under the influence of a gravitational wave propagating through space in the $\hat{z}$-direction, their separation becomes

$$\begin{aligned} \Delta l &= \int |g_{\alpha\beta} dx^\alpha dx^\beta|^{\frac{1}{2}} \\ &= \left(1 + \frac{1}{2} h_{xx}^{TT}\right) \epsilon\,, \end{aligned} \tag{2.27}$$

where h_{xx} was assumed to be a very small perturbation of the flat spacetime. The integration is performed along a pre-defined path that does not coincide with a photon geodesic. Δl is not the distance travelled by a photon propagating from one mass to the other (see section 2.4). Since $h_{\mu\nu}$ describes a wave, the distance between the two masses will oscillate around its original value ϵ. It is trivial to show that two masses separated in the y-direction undergo a similar oscillation:

$$\Delta l = \left(1 - \frac{1}{2} h_{xx}^{TT}\right) \epsilon. \tag{2.28}$$

Similarly, for two masses separated by a distance ϵ at 45° with respect to the $\hat{x}$-axis,

$$\Delta l = \left(1 + \frac{1}{2} h_{xy}^{TT}\right) \epsilon. \tag{2.29}$$

For a ring of independent particles, those three equations (2.27, 2.28 and 2.29) describe the well known deformation of the ring along the two polarization axes of the gravitational wave (figure 2.1). The two polarization modes are now obvious,

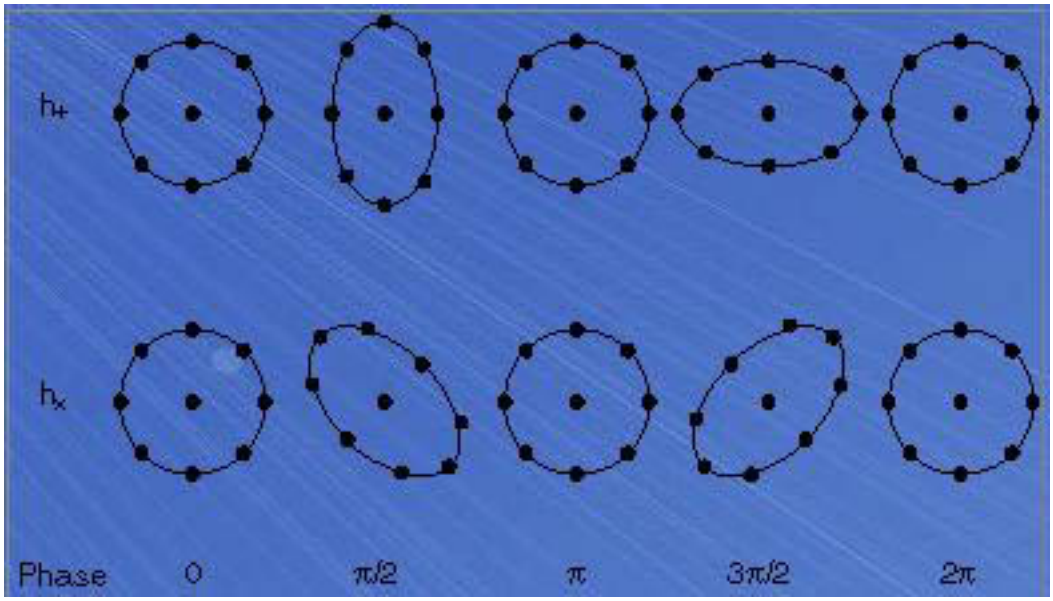

Figure 2.1: The deformation of a ring of test particles under the influence of the two polarization modes of a gravitational wave. The two polarization main axes are clearly separated by 45 degrees (astron.berkeley.edu)

and their axes are rotated by 45° with respect to each other. This differs from the electromagnetic waves whose two polarization axes are 90° apart. The difference finds its roots in the fact that gravitational waves arise from tensor perturbations (i.e. perturbations in the spacetime metric), while electromagnetic waves are due to vector perturbations (i.e. perturbation in the vector potential A^{μ}).

2.3 Gravitational Wave Detectors

It has been shown that gravitational waves must exist, and propagate through flat spacetime at the speed of light. What happens when a gravitational wave disturbs the flat spacetime in which two small masses sit is also known in theory: the distance separating them oscillates. The question is: is it possible and realistic to detect those oscillations? It turns out that it is indeed possible, albeit extremely difficult. For a gravitational wave with a typical amplitude $h = 10^{-20}$, a distance of four kilometers, corresponding to the arm length of the interferometer LIGO (see below), will undergo an oscillation of order 10^{-18} meters. As a comparison, the size of an atom is roughly of the order of 10^{-10} meters, and the diameter of a nucleus is about 10^{-15} meters. This underscores the challenge of achieving a direct detection. However, some indirect observational insights have already been achieved. In 1974, Hulse and Taylor discovered a neutron star binary system [4, 5, 6], PSR B1913+16, the study of which gave the strongest evidence in favor of the existence of gravitational waves.

Like any other waves, gravitational waves can carry energy, linear momentum and angular momentum [7]. A source of gravitational waves will therefore lose energy and momentum. This loss of energy can be theoretically predicted for sources such as binary systems. Careful observations of PSR B1913+16 confirmed that its orbit is decaying by the precise amount expected from the emission of gravitational radiation. Even though these results leave little doubt on the validity of general relativity in such a scenario, there are some caveats. First, this is not a direct observation of

gravitational waves and, though unlikely, it leaves the possibility that the energy is lost via another physical mechanism. Also, and more importantly, this binary system does not generate a strong gravitational field. Hence, the Hulse-Taylor observations only confirm the presence of gravitational waves as predicted by general relativity in a weak field environment. It is possible that general relativity fails to correctly describe a strong gravitational fields. Direct observation of gravitational waves would allow for a test of Einstein theory in both weak and strong fields.

Many devices have been proposed in the quest to make the first direct detection. They can be separated into two categories. The first category of detectors monitors deformation in solids caused by the propagating disturbance of spacetime. In a sense, the idea is to create and observe a "test ring" such as figure 2.1. Instead of a ring of independent particles, solid bars or spheres are used. The Weber bars and the MiniGRAIL (Mini Gravitational Radiation Antenna In Leiden) fall into that group. The second category intends to measure the variations in the time of arrival at a detector of photons emitted from a source. The source can be a laser or astrophysical in nature. Since photons travel at the speed of light in all frames, a variation in the source-detector distance will entail a change in the travel time of the photon, which can be detected. This change can be detected in two ways:

- using an interferometer (figure 2.2). A laser sends light toward two mirrors, located at equal distances and at an angle from each other. The photons are reflected back. If they traveled the same distance, the two signals will have the

same phase. In the presence of gravitational waves, the distances to the two mirrors will vary, and a phase difference can be detected.

- using extremely precise clocks to record the time of emission and the time of arrival of photons. Fortunately, the Universe provides us with such clocks: pulsars. By studying the periodicity of pulses emitted from pulsars and arriving at Earth, we can infer the variations in the Earth-pulsar distance.

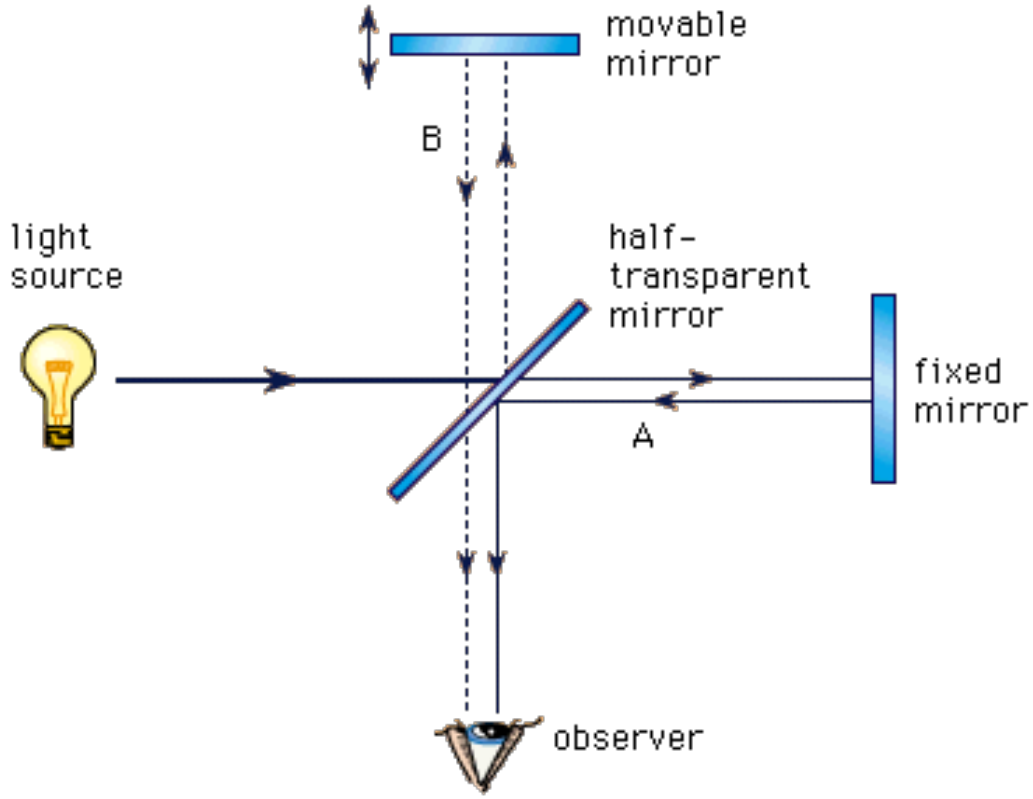

Figure 2.2: Schematic of a Michelson interferometer. A light beam from a source, usually a laser, is split into two beams, which are in turn reflected by two separate mirrors toward an observer. The two beams interfere at the observation point. The interference can range from fully destructive if the beams are totally out of phase to fully constructive if the beams are in phase. The interference pattern records the difference in the path length of the two beams (kspark.kaist.ac.kr)

2.3.1 Weber Bars and MiniGRAIL

Weber bars were the first type of gravitational wave detector to be built. Joseph Weber at University of Maryland created the first one. They typically consist of heavy metal cylinders (e.g. aluminum). Extremely sensitive piezoelectric sensors detect changes in the length of the cylinder. Only extremely strong sources would produce gravitational waves that would affect the length of the cylinders significantly enough for the sensors of Weber's instruments to record it. However, for a narrow range of frequency, the gravitational wave can provoke a resonance in the bar. The variation in the length of the antennas is amplified, which increases the detector sensitivity significantly.

MiniGRAIL is a more modern version of the Weber bar. It exploits the same principles, but is composed of metal spheres, instead of cylinders. The antenna pattern is then uniform, meaning that its sensitivity does not depend on the source location. It has a resonance frequency of $2.9kHz$. It could potentially detect signal from sources such as rotating neutron star instabilities and small black holes mergers.

While using the resonance properties of the detectors increases its sensitivity, the current generation of detectors have modest sensitivity, and only the strongest signals might trigger detection. It also means that the range of frequencies observable is very limited around the resonance frequency. For these two reasons, other types of detectors are more commonly used nowadays.

2.3.2 Interferometers

Interferometers are the most common and the most studied type of gravitational wave detectors. They can be very sensitive. Today's interferometers can detect gravitational waves as small as $h = 10^{-20} - 10^{21}$, but a more sensitive generation of detectors is currently being developed and should be operational in coming years. Their frequency range of operation depends on their arm length. By using arrays of interferometer with different arm lengths, a very broad range of sources could be studied. Interferometers come in two flavors, ground-based and space-based.

Ground-based detectors are easier to build. They need to be more compact, however, and deal with a lot more noise (e.g. seismic activity, environmental vibrations) which limits their sensitivity at low frequency. Since the arm length of the ground based detectors are constrained for practical reasons to an order of a few kilometers, they are ideal to detect higher frequency waves ($10Hz - 10kHz$). Potential sources include merging of smaller binary systems (neutron stars and stellar mass black hole binaries), magnetic mountains on the surface of fast rotating pulsars, and supernovae. Here is a brief description of the current generation of ground-based detectors:

- the Laser Interferometer Gravitational-Wave Observatory (LIGO) consists of two L-shaped observatories located in Livingston, Louisiana and Hanford, Washington. Each arm measures four kilometers (figure 2.3).

- VIRGO has three kilometers arms, but thanks to a system of multiple reflectors, its effective arm length ranges from about 3 to 100 km. It is located in Cascina, Italy (figure 2.4)
- GEO 600 near Sarstedt, Germany is designed to be capable of measuring smaller changes in distance ($\sim 10^{-21}$ meters). It is also smaller than LIGO and VIRGO, with its arms measuring 600 meters.
- TAMA 300 at the National Astronomical Observatory of Japan is a short 300 meters interferometer.

Figure 2.3: The two L-shaped observatories of LIGO, in Hanford,Washington (left) and Livingston, Louisiana (right). The arms are four kilometres in length (astro.berkeley.edu)

Additional ground-based detectors, such as the Australian International Gravitational Observatory (AIGO), have been proposed. They could form, with the already existing detectors, arrays of interferometers, which would improve the chance of a successful detection.

Figure 2.4: Virgo observatory in Cascina, Italy. Each arm measure three kilometres in length (www.apc.univ-paris7.fr)

Space-based detectors allow for a reduction in environmental noise, especially at low frequencies. They are also less limited in size and can explore much lower frequencies but they are more complicated to set up. None have been built yet, but a few designs have been proposed. The main candidate is the Laser Interferometer Space Antenna, or most commonly named, LISA. It is planed to be operational in the next decade. It consists of three spaceships shielding identical free falling masses. The separation between the masses will be about 5×10^9 meters, only 28 times less than the distance from Earth to the Sun. Lasers going from one spaceship to another will precisely monitor the exact relative distance between the free masses. The spaceships will be in orbit around the Sun, trailing about 20° behind Earth (figure 2.5). The enormous size of this interferometer makes its sensitivity peak for frequencies ranging

from $10^{-4}Hz$ to $10^{-2}Hz$. It will be therefore ideal to study binary star systems in our galaxy, extreme mass ratio inspirals (EMRI), which consist of a stellar mass object (e.g. neutron star, small black hole) being captured by a massive or supermassive black hole, and massive black hole mergers.

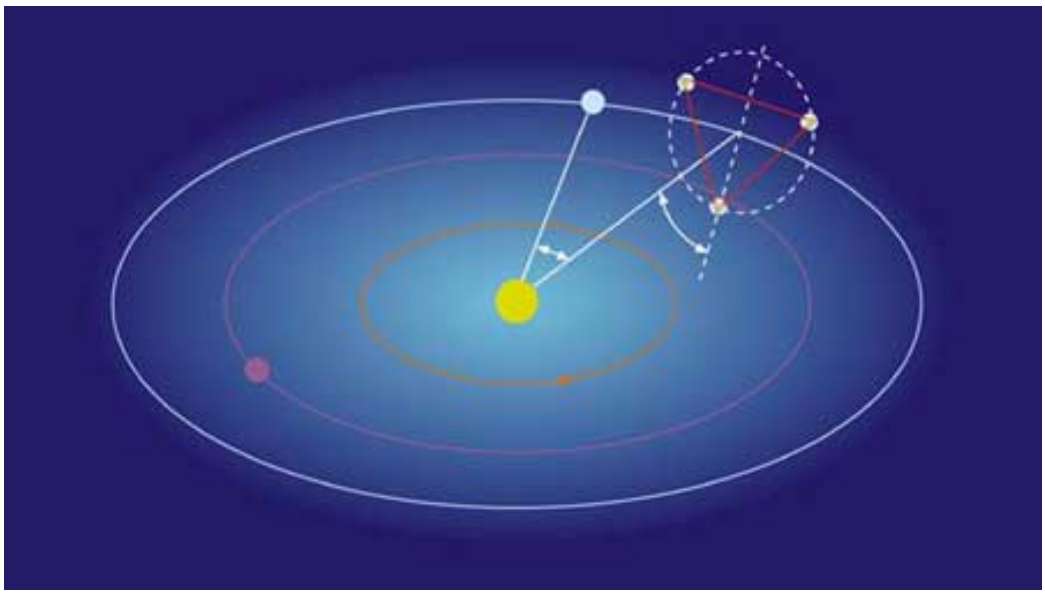

Figure 2.5: LISA is composed of three spaceships orbiting around the Sun, trailing 20° behind Earth. The spaceships are separated from each other by 5 million kilometres (astro.berkeley.edu)

The Big Bang Observer (BBO) is an advanced space based detector that has been proposed as a follow-on to the LISA mission. Its main goal is to detect the cosmic gravitational background (CGB) issued from the Big Bang. To that effect, BBO needs a good sensitivity to $0.1 - 1Hz$ gravitational waves, a frequency range that contains few astrophysical sources, implying low confusion noise. Its design is therefore similar to LISA's but with twice as many proof masses separated by a shorter distance (~ 100 times shorter), which form a "star of David" design. It would also possibly possess

two additional LISA-like telescope, on either side of the main cluster of spaceship, to help with angular resolution (figure 2.6). More about the Big Bang Observer and its application to the detection of the CGB can be found in chapters 3 and 4.

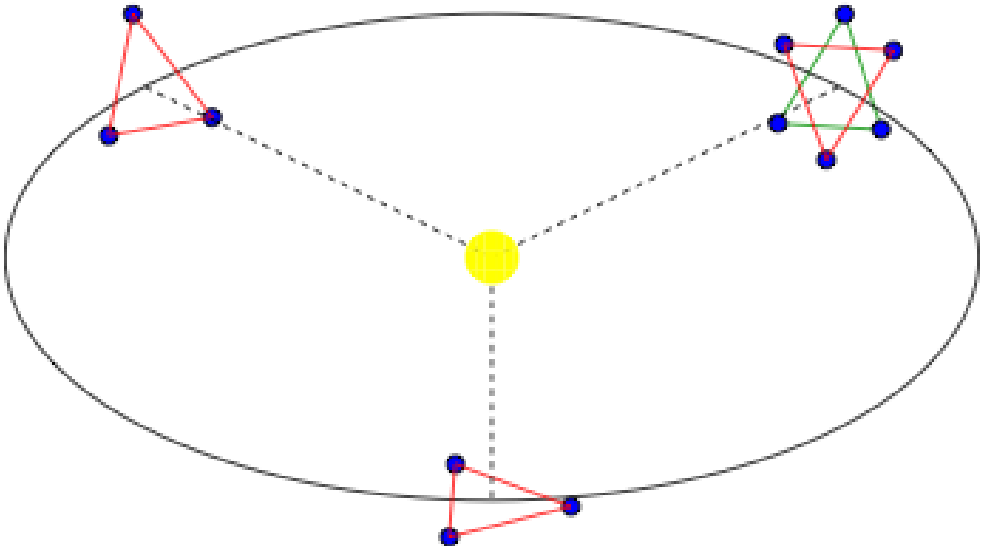

Figure 2.6: This figure is taken from [1]. It shows the proposed design for the Big Bang Observer

2.3.3 Pulsar Timing Arrays

Pulsars are very rapidly rotating, highly magnetized neutron stars that emit a beam of photon. As the star rotates, so does the orientation of the beam. The electromagnetic radiation can only be observed with radio telescopes when the beam sweeps across the Earth. The signal received on Earth is therefore a pulse. Since neutron stars are extremely dense objects, their rotation is very regular, and the period of the pulses, ranging from milliseconds to seconds, remains constant to very high accuracy.

Pulsars are the Universe's clocks. They are actually some of the most accurate clocks, competing with the best atomic clocks on Earth. When a gravitational wave passes through space, the distance between a pulsar and a telescope on Earth will contract and expand in an oscillatory manner. This will cause a discrepancy between the actual and expected time of arrival of the photons on Earth. The difference between the two times is called a residuals. By looking at the residuals from data collected by radio telescopes, one can study gravitational waves. However, this is a complex matter as residuals can be created by many other phenomena (e.g. dispersion through interstellar medium, Earth orbital motion around the Sun) that need to be modeled and predicted in order to isolate the contribution from the gravitational waves. Combining the residuals from different pulsars greatly increases the chances of detecting gravitational waves, and would allow locating a source in the sky. Only few pulsars are timed precisely enough (up to a $100\,ns$ precision), but the list is growing fast. The detector formed by the array of timed pulsars and the timing device on Earth is called a pulsar timing array, or PTA (figure 2.7). Since the timed pulsars are located so far away from Earth (0.5 to $1.5\,kpc$), pulsar timing arrays are particularly sensitive to very low frequency, from $10^{-9}Hz$ to $10^{-7}Hz$. They are best-suited to study massive and supermassive black holes binaries (chapters 5 and 7).

Interferometer type detectors (LIGO, LISA, BBO...) and pulsar timing arrays are the best candidate for the first gravitational waves detection, and the only one studied in this thesis. Though their mechanisms are slightly different, they both rely

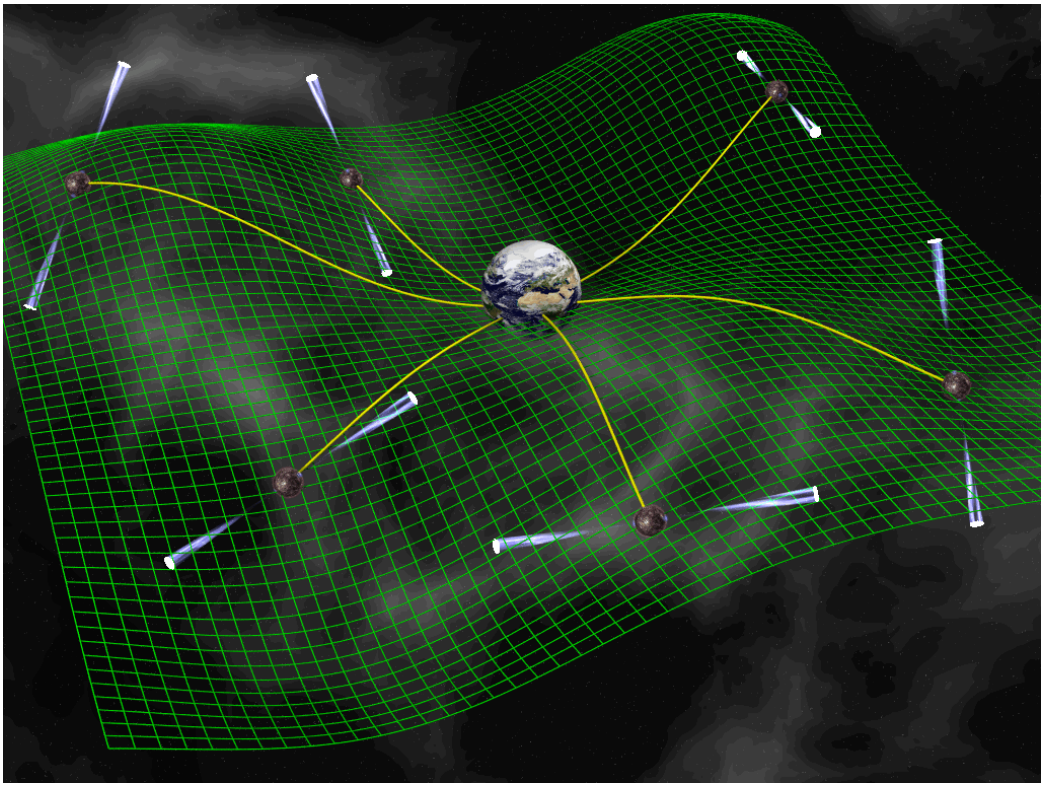

Figure 2.7: The figure shows how an array of 6 pulsars is affected by a gravitational waves. The pulsars are typically located 0.5 to 1.5 kpc away from Earth (www.mpifr-bonn.mpg.de)

on the knowledge of the disturbance in the travel time of a photon going from a source to a receiver, or residuals to borrow the terminology of PTAs. A derivation of the residuals is given in next section.

2.4 Residuals Along a Photon Trajectory: a Derivation

We want to find the difference in the time it takes a photon to go from point $\vec{x_1} \rightarrow (0,0,0,0)$ to point $\vec{x_2} \rightarrow (t_f, x_f, y_f, z_f)$ with and without the presence of a gravitational wave on the otherwise flat metric. There is more than one valid way to approach that problem. Finn [8] tackles the problem by solving the geodesic equations in their differential form. Estabrook and Wahlquist's approach [9], recently revisited by Cornish [10], makes use of the invariance of the perturbed metric under coordinate changes to form a set of four constraint equations. The solution to this system of equations yields the residuals. The derivation given here closely follows the outline given by Cornish.

Assuming that the photon trajectory is far from any significant source of gravitational field, the gravitational wave can be treated as a perturbation, whose amplitude is very small, on a otherwise flat metric. The wave is chosen to propagate in the $\hat{z}$ direction. The line element along the photon trajectory is

$$ds^2 = -dt^2 + dx^2 + (1 + h_{xx})dx^2 + (1 + h_{yy})dy^2 + 2h_{xy}dxdy\,., \tag{2.30}$$

with

$$h_{xx} \;=\; -h_{yy} = A_{xx}e^{-i\omega(z-t)}\,,$$

$$h_{xy} \;=\; -h_{yx} = A_{yx} e^{-i\omega(z-t)}\,, \tag{2.31}$$

being the components of the wavelike perturbation tensor. The symmetries become more obvious after a simple rotation of the coordinate system:

$$\begin{aligned} u &= t - z \\ v &= t + z\,. \end{aligned} \tag{2.32}$$

The perturbation is now dependent on one variable only, as its exponential becomes $e^{i\omega u}$. The line element is rewritten in the new coordinate system:

$$ds^2 = -dudv + (1 + h_{xx})dx^2 + (1 + h_{yy})dy^2 + 2h_{xy}dxdy\,. \tag{2.33}$$

The metric elements clearly don't depend on x,y and v. Three Killing vectors can then be formed, $\vec{\xi} = \hat{x}$,$\vec{\zeta} = \hat{y}$ and $\vec{\eta} = \hat{v}$, each satisfying the Killing equations

$$\nabla_\alpha \xi_\beta + \nabla_\beta \xi_\alpha = 0\,, \tag{2.34}$$

where ∇_α is the covariant derivative defined by

$$\nabla_\alpha \xi_\beta = \partial_\alpha \xi_\beta + g_{\beta\mu}\Gamma^\mu_{\alpha\nu}\xi^{nu}\,. \tag{2.35}$$

The presence of Killing vectors underlines the invariance of the metric under some coordinate changes. Here, the metric is clearly invariant under translations in the x, y and v-direction. Consequently, the action

$$S = -\frac{1}{16\pi}\int d^4x\, R\sqrt{-g} \tag{2.36}$$

is similarly invariant. From Noether's theorem, each invariance implies a conserved quantity. These quantities can be expressed in term of the Killing vectors:

$$p_\mu \xi^\mu = a_1$$

$$p_\mu \zeta^\mu = a_2$$

$$p_\mu \eta^\mu = a_3 \,. \tag{2.37}$$

p_μ are the one-form components of the photon momentum. a_1, a_2 and a_3 are constant along the photon path:

$$\frac{\partial a_1}{\partial \lambda} = \frac{\partial a_2}{\partial \lambda} = \frac{\partial a_3}{\partial \lambda} = 0 \,. \tag{2.38}$$

λ is a variable parametrizing the photon trajectory from $\vec{x_1}$ to $\vec{x_2}$. Photons are massless, and this condition adds yet another constraint on their momentum , $p^\mu p_\mu = 0$. Along with equations 2.37, it gives four constraints that can be rewritten as

$$\begin{aligned}
&(1 + h_{xx})\frac{dx}{d\lambda} + h_{xy}\frac{dy}{d\lambda} = a_1 \\
&(1 + h_{yy})\frac{dy}{d\lambda} + h_{xy}\frac{dx}{d\lambda} = a_2 \\
&\frac{du}{d\lambda} = -2a_3 \\
&2a_3\frac{dv}{d\lambda} + a_1\frac{dx}{d\lambda} + a_2\frac{dy}{d\lambda} = 0 \,.
\end{aligned} \tag{2.39}$$

The constant of proportionality between the momentum p^μ and the photon "4-velocity" $\frac{dx^\mu}{d\lambda}$ was absorbed in the constants a_i. Since h is very small, a perturbative method can be used to solve this system of equations. The constraints can be expressed in terms of

$$x^\mu = {x_0}^\mu + \delta x^\mu \text{ and } a_i = {a^0}_i + \delta a_i \,, \tag{2.40}$$

where ${x_0}^\mu$ and ${a^0}_i$ satisfy the constraints in flat space, where $h = 0$:

$$\begin{aligned}
{a^0}_1 &= \frac{dx_0}{d\lambda} \quad \Longrightarrow \quad {a^0}_1 = \frac{x}{\lambda_2 - \lambda_1} \\
{a^0}_2 &= \frac{dy_0}{d\lambda} \quad \Longrightarrow \quad {a^0}_2 = \frac{y}{\lambda_2 - \lambda_1} \\
{a^0}_3 &= -\frac{1}{2}\frac{dx_0}{d\lambda} \quad \Longrightarrow \quad {a^0}_3 = -\frac{1}{2}\frac{L - z}{\lambda_2 - \lambda_1}\,.
\end{aligned} \tag{2.41}$$

L is the non-perturbed distance between the two points $\vec{x_1}$ and $\vec{x_2}$. a_i must be perturbed as well. Even though the components of the photon momentum one-form p_x, p_y and p_v are still constant along the photon path in the presence of a gravitational wave, they might be different from their values associated with the photon traveling in flat space. That is equivalent to saying the direction of propagation of the photon has been changed by the perturbation. It is referred to as gravitational lensing of the photon path by the gravitational wave. Rewriting the equations 2.39 to first order in perturbation using 2.40 and 2.41, one obtains

$$\begin{aligned}
\delta a_1 &= h_{xx}{a^0}_1 + h_{xy}{a^0}_2 + \frac{d\delta x}{d\lambda} \\
\delta a_2 &= h_{xx}{a^0}_2 + h_{xy}{a^0}_1 + \frac{d\delta y}{d\lambda} \\
\frac{d\delta u}{d\lambda} &= -2\delta a_3 \\
2\delta a_3\frac{dv_0}{d\lambda} &+ \delta a_1\frac{dx_0}{d\lambda} + \delta a_2\frac{dy_0}{d\lambda} + 2{a^0}_3\frac{d\delta v}{d\lambda} + {a^0}_1\frac{d\delta x}{d\lambda} + {a^0}_2\frac{d\delta y}{d\lambda} = 0\,.
\end{aligned} \tag{2.42}$$

In the transverse-traceless gauge, the spatial coordinates (i.e. x, y and z) of the test particles are not affected by the gravitational wave, $\delta x^i(\lambda_1) = \delta x^i(\lambda_2) = 0$. Therefore

$$\int_{\lambda_1}^{\lambda_2}\frac{d\delta x}{d\lambda} = \int_{\lambda_1}^{\lambda_2}\frac{d\delta y}{d\lambda} = 0 \text{ and } \int_{\lambda_1}^{\lambda_2}\frac{d\delta u}{d\lambda} = \int_{\lambda_1}^{\lambda_2}\frac{d\delta v}{d\lambda} = \delta t(\lambda_2 - \lambda_1)\,. \tag{2.43}$$

Upon integration by λ, it is easily shown that the constraints become

$$\begin{aligned}
\delta a_1 &= a^0{}_1 H_{xx} + a^0{}_2 H_{xy} \\
\delta a_2 &= a^0{}_2 H_{xx} + a^0{}_1 H_{xy} \\
\delta a_3 &= -\frac{1}{2}(\lambda_2 - \lambda_1)\delta t \\
2\delta a_3 v_f + \delta a_1 x_f + \delta a_2 y_f &= 0\,,
\end{aligned} \tag{2.44}$$

with $H_{ij} = \int_0^{t_f - z_f} h_{ij}(u)\mathrm{d}u$. This system of 4 equations, when combined with equation 2.41, yields the residuals

$$\delta t = \frac{1}{2L(L-z)}\left(x^2 H_{xx} + y^2 H_{yy} + 2xy H_{xy}\right)\,, \tag{2.45}$$

which, in a coordinate-independent form, becomes:

$$\delta t = \frac{\hat{x}\otimes\hat{x} : \mathbf{H}}{2\left(1 - \hat{k}\cdot\hat{x}\right)}\,, \tag{2.46}$$

where by convention the colon implies a double contraction ($A : B = A^{ij}B_{ij}$). All the tools necessary to make sense of the signals received by gravitational waves interferometers and pulsar timing arrays have now been laid out. In following chapters, it will be shown how such detectors can be used to study cosmological sources of gravitational waves.

CHAPTER 3

COSMIC GRAVITATIONAL BACKGROUND

3.1 Introduction

In 1964, Robert Wilson and Arno Penzias, two radio engineers working at Bell labs, discovered that the Universe is almost uniformly filled by electromagnetic radiation, particularly in the microwave regime. This almost uniform glow is now called the cosmic microwave background (CMB). It is formed by radiation issued from very early stages of the Universe. It contains tiny fluctuations, which are the result of density fluctuations imprinted by inflation. The study of these fluctuations gave strong evidence in favor of the Big Bang theory. Unfortunately, at its beginning the Universe was opaque, meaning that any radiation created would have been re-absorbed. It became transparent 379000 years after its creation. It is therefore not possible to observe older electromagnetic radiation. This considerably reduces the scientific insight on the birth of our Universe that one can achieve using traditional astronomy. It particularly affects our knowledge of some key phases of its evolution that occurred much earlier than 400000 years after the Big Bang (e.g. inflation). It is important to find other means to "observe" earlier stages of the Universe, to unlock knowledge about some crucial concepts in high-energy physics. Gravitational waves might be the answer to that problem. Gravitational waves interact very weakly with matter, which is also why they are so challenging to detect. While the Universe was opaque to electromagnetic waves, gravitational waves were able to propagate

freely. Gravitational waves emitted during and after the Big Bang would still fill the Universe, and could in theory be detected. In the same manner as the cosmic microwave background, they form the cosmic gravitational wave background (CGB). Hogan [11] describes the CGB as an "unobstructed view of our past light cone".

Gravitational waves are redshifted by the continuous expansion of the Universe. Consequently the frequency of the gravitational waves forming the cosmic background is going to be dependent on the time at which they were produced. By observing the CGB in different frequency windows, different eras of the expansion can be explored. A rough estimate is given by [11]:

$$\omega_0(z) \equiv \frac{H(z)}{(1+z)} \approx 2 \times 10^{-5} Hz \frac{T(z)}{100GeV}\,, \tag{3.1}$$

where z is the cosmological redshift, and T the temperature of the Universe. $\omega_0(z)$ would be the wave angular frequency observed today if it had been emitted at horizon scale when the Universe had a temperature T. T therefore indicates what is the hottest (oldest) time of the Universe that can be studied by observing gravitational waves of frequency ω_0 or lower. LISA whose optimum sensitivity is located between $10^{-4} - 10^{-2}\,Hz$ would be able to probe at 10^{-2} to 10^4 seconds after the Big Bang. The Big Bang observer, whose peak sensitivity is higher (0.1-1Hz), will probe even farther into the genesis of the Universe.

The cosmic gravitational background is likely to be isotropic and stochastic. It will therefore be difficult to extract it from the noise in the instruments. It is also

expected to be stationary and unpolarized [12]. It has a wide variety of possible sources [13, 14]:

- Amplification by inflation of primordial fluctuations in the Universe geometry [15]. The properties of this type of background are dependent on the inflation model. For a description of four different inflation models (power-law inflation, chaotic inflation, symmetry breaking inflation,hybrid inflation) and their implications on the CGB, see [16].
- Phase transitions as previously unified interactions separate.
- Condensation of a brane from a higher dimensional space.
- Cosmic string [17, 18, 19, 20, 21],
- Large population of indiscernible astrophysical (younger) sources such as binary systems.

3.2 Characterization of the CGB

All the sources mentioned above could potentially produce a stochastic gravitational wave background that is isotropic, stationary and unpolarized. Yet, they will differ from each other through their energy spectra. In other words, the manner in which the amplitude of the background varies as a function of frequency will allow for a distinction between the different types of backgrounds. It is customary to characterize the gravitational wave background by its energy density per unit logarithmic

frequency interval, which is derived from the energy density:

$$\Omega_{gw}(f) = \frac{1}{\rho_c}\frac{d\rho_{gw}}{d(logf)}\,. \tag{3.2}$$

ρ_c is the critical energy needed to close the Universe as it stands today. It is a function of the Hubble constant:

$$\rho_c = \frac{3{H_o}^2}{8\pi}\,. \tag{3.3}$$

The energy density Ω_{gw} can therefore be written in term of the Hubble constant. The Hubble constant is not a well-known quantity. Its value has been subject to many revisions [22, 23, 24], and while new measurements have constrained its bounds more tightly, the debate is still ongoing. The latest estimation [25], which makes use of Hubble Space Telescope to measure gravitational lensing along with the WMAP data set, quotes

$$H_o = h_o \times 100\frac{km}{sec.Mpc} \text{ with } 0.648 < h_o < 0.747\,, \tag{3.4}$$

assuming a flat Universe. h_o is a unitless quantity representing the uncertainty in the Hubble constant. It is often associated to Ω_{gw}, as to define a new energy density quantity that will only be dependent on the type of background it is used to describe:

$${h_o}^2\Omega_{gw}(f) = \frac{8\pi}{3\times 10^4}\frac{d\rho_{gw}}{d(logf)}\,. \tag{3.5}$$

The gravitational wave background is often characterized in the literature by its power spectral density $S_h(f)$. In chapter 4, both the energy density $\Omega_{gw}(f)$ and spectral density $S_h(f)$ will be used to describe the properties of the CGB. Since they are both

a description of how strong the background is, it is possible to express one in term of the other. It is briefly shown here how they are related.

First the energy density ρ_{gw} is found as a function of the background amplitude:

$$\rho_{gw} = \frac{1}{32\pi}\langle \dot{h}_{ij}\dot{h}^{ij}\rangle \,. \tag{3.6}$$

As usual, the dots represent time derivatives, and the brackets an average over one period. The background can in turn be expanded in term of plane waves propagating in the $\hat{\Omega}$-direction, or their Fourier transform:

$$h_{ij}(t) = \sum_p \int_{-\infty}^{+\infty} df \int d\hat{\Omega}\, \tilde{h}\left(f,\hat{\Omega}\right) e^{-2\pi i f t} e^p_{ij}\left(\hat{\Omega}\right) \,. \tag{3.7}$$

The index p represents the two polarization modes $(+,\times)$, and $e^p_{ij}\left(\hat{\Omega}\right)$ is the polarization tensor. $d\hat{\Omega}$ is the solid angle: $d\hat{\Omega} = d\cos(\theta)d\phi$.

If $\hat{m}$ and $\hat{n}$ are unit vectors forming an orthonormal basis with $\hat{\Omega}$, the polarization tensor becomes:

$$\begin{aligned} e^+_{ij} &= \hat{m}_i\hat{m}_j - \hat{n}_i\hat{n}_j \,, \\ e^\times_{ij} &= \hat{m}_i\hat{n}_j - \hat{n}_i\hat{m}_j \,. \end{aligned} \tag{3.8}$$

The contraction in equation 3.6 becomes

$$\dot{h}_{ij}\dot{h}^{ij} = \sum_{p,p'} \int_{-\infty}^{+\infty} df df' \int d\hat{\Omega} d\hat{\Omega}' \left(-4\pi^2 f f'\right) \tilde{h}\left(f,\hat{\Omega}\right) \tilde{h}\left(f',\hat{\Omega}'\right) e^{-2\pi i (f+f')t} e^p_{ij} e^{p',ij} \,. \tag{3.9}$$

First, from equation 3.8, we see that $e^p_{ij}e^{p',ij} = 2\delta(pp')$. Also the complex conjugate of the plane wave in the frequency domain at frequency f is the same plane wave

evaluated at frequency $-f$:

$$\tilde{h}^* \left(f, \hat{\Omega}\right) = \tilde{h} \left(-f, \hat{\Omega}\right) . \tag{3.10}$$

So we can use the symmetry of the integral in f' to rewrite equation 3.6 as

$$\rho_{gw} = \frac{\pi}{2} \int_{-\infty}^{+\infty} df df' \int d\hat{\Omega} d\hat{\Omega}' \, f f' \langle \tilde{h} \left(f, \hat{\Omega}\right) \tilde{h} \left(f', \hat{\Omega}'\right) \rangle e^{-2\pi i (f - f')t} \tag{3.11}$$

For a stochastic, isotropic, stationary and unpolarized background, the spectral density $S_h(f)$ is defined as:

$$\langle \tilde{h} \left(f, \hat{\Omega}\right) \tilde{h} \left(f', \hat{\Omega}'\right) \rangle = \frac{1}{4\pi} \delta \left(f - f'\right) \delta \left(\cos\theta - \cos\theta'\right) \delta \left(\phi - \phi'\right) \frac{1}{2} S_h(f) . \tag{3.12}$$

The energy density ρ_{gw} becomes

$$\begin{aligned} \rho_{gw} &= \frac{\pi}{2} \int_{-\infty}^{+\infty} df df' \frac{1}{2} f f' S_h(f) e^{-2\pi i (f - f')t} \delta \left(f - f'\right) \int d\hat{\Omega} d\hat{\Omega}' \frac{1}{4\pi} \delta \left(\cos\theta - \cos\theta'\right) \delta \left(\phi - \phi'\right) \\ &= \frac{\pi}{2} \int_{0}^{+\infty} df \, f^2 S_h(f) . \end{aligned} \tag{3.13}$$

By taking the derivative of ρ_{gw} with respect to the natural logarithm of f, and by dividing by the critical energy density, the energy density per unit logarithmic frequency interval is finally obtained in terms of the power spectral density:

$$\Omega_{gw}(f) = \frac{4\pi^2}{3{H_o}^2} f^3 S_h(f) . \tag{3.14}$$

In the following section, a short review of the known limits on the maximum energy density Ω_{gw} allowed for the gravitational wave background will be given.

3.3 Existing Bounds on the CGB Energy Density

Some bounds have already been placed on the energy density of the cosmic gravitational wave background. Here some of these bounds, and the concepts behind them, are briefly described. More detailed descriptions can be found in the literature.

3.3.1 Nucleosynthesis

Primordial nucleosynthesis, sometimes called nucleogenesis or Big Bang nucleosynthesis (BBN), occurred during the first three minutes of the Universe. It is the process of creating new atomic nuclei from nucleons (neutrons and protons). It is responsible for the primordial relative density of protium (^1H), deuterium (^2H), helium-3 (^3He), helium-4 (^4He) and Lithium (^7Li). It is believed that most of the current mass of these elements has been created during nucleogenesis. The current theory for the primordial nucleosynthesis reproduces very accurately the primordial abundance of these elements. It predicts that during the nucleosynthesis the ratio of the number density of neutrons with the number density of protons will decay exponentially with the inverse of the Universe temperature:

$$\frac{n_n}{n_p} = e^{-\frac{m_n - m_p}{T}} . \tag{3.15}$$

This ratio is guaranteed by the following reactions:

$$p^+ + e^- \longleftrightarrow n^0 + \nu_e \tag{3.16}$$

A proton and an electron will combine to give a neutron and a neutrino, and inversely. This reaction, however, can only secure the relative density of protons and neutrons

if the Universe is energetic enough. As the Universe cools down, it cools to a critical temperature T_f at which this reaction will cease to be able to compete with the expansion of the Universe, and the thermal equilibrium is broken. It is the end of the nucleogenesis. The relative density of protons and neutrons is then frozen at

$$\frac{n_n}{n_p} = e^{-\frac{m_n - m_p}{T_f}} , \tag{3.17}$$

and light atomic elements (^1He,^2He...) cease to be produced. Since the primordial abundance of those elements is known, the time at which the Universe reached the temperature T_f can be predicted. It marks the end of the nucleogenesis, which in turns is dependent on the total energy density of the Universe today, part of which comes from gravitational waves. It is therefore possible to use our knowledge of nucleosynthesis to give an upper bound on the energy density of the cosmic background formed by the gravitational waves emitted before or during nucleosynthesis. Due to ongoing debate on observational errors [26, 11, 27, 28], it is difficult to give an exact constraint from the Big Bang nucleosynthesis, but recent estimates [29] give

$$\Omega_0^{\mathrm{gw}}(f) < 1.5 \times 10^{-5} \text{ for } f_{\mathrm{bbn}} < f < f_{\mathrm{end}} \, . \tag{3.18}$$

This constraint only applies to gravitational waves produced before the Universe cools down below T_f, and therefore is limited to waves whose wavelength is smaller than the horizon at that time ($f > f_{\mathrm{bbn}}$), and bigger than the horizon at the time of the first gravitational wave emission ($f < f_{end}$).

3.3.2 Sachs-Wolfe Effect

The study of the cosmic microwave radiation can give an upper bound on the energy density of the cosmic gravitational wave background for some frequencies. If the CGB is strong, then a noticeable redshift of the photons from the microwave background is expected. Therefore fluctuations in the temperature of the CMB ($2.7K$) will become apparent. The gravitational redshifting of the photons from the CMB is called Sachs-Wolfe effect. It is the main source of large angular scale fluctuations ($> 10°$). Smaller angle fluctuations, on the other hand, refer to regions causally connected and can have been caused by microphysical process on the surface of last scattering [13]. For a more in depth description see [30, 31].

The Sachs-Wolfe effect can be caused by both scalar and tensor perturbations, the later being of course gravitational waves. The proportion of large-scale fluctuations caused by gravitational waves is therefore model dependent. But independently of the model one can already give an optimistic upper bound [32, 33]:

$$\Omega_0^{\mathrm{gw}}(f) < 7 \times 10^{-11} \left(\frac{H_0}{f}\right)^2 \text{ for } 3 \times 10^{-18}\, Hz < f < 10^{-16}\, Hz\,. \tag{3.19}$$

3.3.3 Pulsar Timing

It was mentioned in chapter 2 that pulsars can be used as clocks in order to detect gravitational waves. In particular the millisecond pulsars (whose period of rotation is of the order of the milliseconds) are very precise clocks. In recent years, the precision in the timing by radio telescope of the signals arriving from pulsars

has improved so much that a renewed interest in using pulsar timing arrays has compelled many researchers to study what can be extracted from already existing data sets. It appears that pulsars timing is particularly sensitive to continuous sources such as gravitational backgrounds. Actually the sensitivity of the pulsar timing to a gravitational wave increases linearly with time for a frequency inversely proportional to the time of observation [13]. Using a few years of observations worth of data from PSR B1855+09 Thorsett and Dewey [34] claimed a constraint on the gravitational wave background at a frequency $f = 4.4 \times 10^{-9}\, Hz$ of the order

$$h_0^2 \Omega_{gw} \left(f = 4.4 \times 10^{-9}\, Hz \right) < 10^{-8}\,, \tag{3.20}$$

for a 95% detection rate. From this result one can calculate a similar limit for higher frequencies:

$$h_0^2 \Omega_{gw}(f) < 10^{-8} \left(\frac{f}{4.4 \times 10^{-9} Hz} \right)^2 . \tag{3.21}$$

This constraint places an upper limit on the background in the scenario of a non-detection by pulsar timing after a time of observation $T_{obs} = 1/f$. It applies to all kind of backgrounds, including an isotropic and stochastic background formed by astrophysical sources. In a more recent study, Jenet et al. [35] analyzed data from seven different pulsars. Using a novel analysis method, they were able to give a separate upper bound for three types of background (relic GW from inflation, cosmic string and supermassive black holes) at three different frequencies (3.2×10^{-8}, 4.0×10^{-9} and 1.6×10^{-9} Hertz). Table 3 in [35] summarizes their results. For a relic gravitational wave background, which is the type of background considered in

chapter 4, a constant constraint across those frequencies is quoted:

$$h_0^2 \Omega_{gw}(f) < 2.0 \times 10^{-8} \,. \tag{3.22}$$

It is believed that the relic gravitational waves from inflation will be very weak ($\Omega_{gw} < 10^{-15}$ in the LIGO frequency range [36, 14]). The testing of the different models of inflation (power-law inflation, chaotic inflation...) with gravitational waves requires highly sensitive detectors. The Big Bang observer seems to be perfectly fit for such a mission. Being space-based, it is not affected by environmental noise. Then it observes at frequencies ($0.1Hz$) at which only very few astrophysical sources emit. The inflationary background will most likely be dominant at these frequencies. Also, its particular design, six spaceships forming a Star of David, allows for using novel analysis methods consisting of multiple cross-correlations of detectors with uncorrelated noises. In Chapter 4 the maximum constraint that observations with BBO could place on the CGB energy density per unit logarithmic frequency interval will be calculated.

CHAPTER 4

DETECTING THE COSMIC GRAVITATIONAL BACKGROUND WITH THE BIG BANG OBSERVER

4.1 Introduction

Most theories describing the formation of the Universe (Inflation, Qflation, etc.) predict that processes in the early Universe will lead to the copious production of gravitational waves. The detection of such a cosmic gravitational background (CGB) would allow us to probe the earliest moments in the history of the Universe, and place strong constraints on the competing theories [37]. However, detecting the CGB will not be easy since it will be hidden behind the signals from astrophysical sources (binaries systems...) and buried in the instrumental noise. Our current understanding of compact binary systems suggests that there is a window above 0.1 Hz where the number of astrophysical sources is small enough that their contribution can be isolated and removed from the detector data streams [38, 39]. The CGB signal can then be dug out of the instrument noise by cross-correlating the outputs of two or more independent detectors [40, 41]. The Big Bang Observer (BBO) [42] has been proposed as a future space based mission designed to operate in the range $0.1 \rightarrow 1\,\mathrm{Hz}$. The BBO proposal calls for a fleet of triangular interferometers operating on the same principle as the Laser Interferometer Space Antenna (LISA). The BBO detectors will be ~ 100 times smaller than the LISA detector, and will be considerably more sensitive. It is possible to synthesize three independent data channels [43] (labeled

(A, E, T)) in each detector. In principle one could cross correlate these channels using data from a single detector as the channels are nominally noise orthogonal. However, the A and E channels are also signal orthogonal, and the T channel has poor sensitivity to waves with wavelengths larger than the detector. Moreover, the three channels are constructed from links that share common noise sources, so it will be difficult to achieve exact noise orthogonality in practice. The BBO design overcomes these obstacles by employing multiple detector units. A pair of co-planar detectors yields the greatest sensitivity as the antenna patterns have significant overlap. The BBO design also calls for two widely separated "outrigger" constellations that give enhanced angular resolution for detecting astrophysical sources [44], but the wide separation ($\sqrt{3}$AU = 866 sec) renders them useless for performing cross correlated detection of the CGB in the $0.1 \rightarrow 1\,\mathrm{Hz}$ range.

Here we study the optimal cross correlation of co-planar triangular interferometers. This work generalizes earlier studies [45, 46, 47] that only considered the cross correlation of two Michelson channels. By cross-correlating all possible combinations of the A, E, T channels in the two detectors the overall sensitivity is improved by a factor of $\sqrt{2}$ at low frequencies and by a factor of $\sqrt{3}$ at high frequencies. In contrast to the single channel case [47], the optimal sensitivity is independent of the relative angle between the two co-planar detectors. We find that the fiducial BBO design [42] will permit the detection of a scale invariant CGB with $\Omega_{gw} = 2.2 \times 10^{-17}$ at 95% confidence, which is lower than the existing upper bounds described in chapter 3.

We begin in Section II by describing the gravitational wave response of the A, E and T channels. This is followed in Section III by a calculation of the noise transfer functions in each channel. Section IV describes the optimal cross correlation of the independent data channels in a pair of co-planar detectors. Section V covers the numerical evaluation of the overlap functions and a calculation of the optimal BBO sensitivity. We use geometric units with $G = c = 1$.

4.2 Detector Response

The noise orthogonal data channels A, E and T are formed from linear combinations of the three Sagnac channels s_1, s_2, s_3:

$$A = \frac{1}{\sqrt{2}}(s_3 - s_1) \qquad E = \frac{1}{\sqrt{6}}(s_1 - 2s_2 + s_3) \qquad T = \frac{1}{\sqrt{3}}(s_1 + s_2 + s_3) \qquad (4.1)$$

The Sagnac interferometer measures the phase difference of two laser beams starting from the same location and going around the triangle formed by the three spacecraft, one traveling clockwise, the other counterclockwise. Ideally the phase difference is due only to the variations of the interferometer arms' length caused by the gravitational waves. Therefore if the beams start from spacecraft 1, the signal is simply

$$s_1(t) = \frac{1}{3L}[l_{13}(t-3L)+l_{32}(t-2L)+l_{21}(t-L)-l_{12}(t-3L)-l_{23}(t-2L)-l_{31}(t-L)], \quad (4.2)$$

where $l_{ij}(t - nL)$ is the distance at time $t - nL$ between spacecraft i and j and L is the length of the interferometer arms (assuming all the arms have the same length). For a plane gravitational wave propagating in $\hat{\Omega}$ direction, this can be shown [47] to

reduce to

$$s_1(t) = \mathbf{D}_s(\vec{a}_1, \vec{b}_2, \vec{c}_3, \hat{\Omega}, f) : \mathbf{h}(f, t, \vec{x_1}), \tag{4.3}$$

where $\vec{a}_1, \vec{b}_2, \vec{c}_3$ are vectors that point along the interferometer arms, $\mathbf{h}(f, t, \vec{x_1})$ is the tensor describing the wave in the transverse-traceless gauge at point $\vec{x_1}$,

$$\mathbf{D}(\vec{a}_1, \vec{b}_2, \vec{c}_3, \hat{\Omega}, f) = \frac{1}{6}\left(\vec{a} \otimes \vec{a}\; T_1(f, \vec{a}) + \vec{b} \otimes \vec{b}\; T_2(f, \vec{b}) + \vec{c} \otimes \vec{c}\; T_3(f, \vec{c})\right) \tag{4.4}$$

and

$$T_1(\vec{a}, f) = e^{-if_n(1+\vec{a}\cdot\hat{\Omega})}\text{sinc}\left(f_n(1 + \vec{a}\cdot\hat{\Omega})\right) - e^{-if_n(5+\vec{a}\cdot\hat{\Omega})}\text{sinc}\left(f_n(1 - \vec{a}\cdot\hat{\Omega})\right), \tag{4.5}$$

$$T_2(\vec{b}, f) = e^{-if_n\left[3+(\vec{a}-\vec{c})\cdot\hat{\Omega}\right]}\left[\text{sinc}\left(f_n(1 + \vec{b}\cdot\hat{\Omega})\right) - \text{sinc}\left(f_n(1 - \vec{b}\cdot\hat{\Omega})\right)\right], \tag{4.6}$$

$$T_3(\vec{c}, f) = e^{-if_n(5-\vec{c}\cdot\hat{\Omega})}\text{sinc}\left(f_n(1 + \vec{c}\cdot\hat{\Omega})\right) - e^{-if_n(1-\vec{c}\cdot\hat{\Omega})}\text{sinc}\left(f_n(1 - \vec{c}\cdot\hat{\Omega})\right), \tag{4.7}$$

with $f_n = \pi L f$. Similarly the Sagnac signal extracted at vertex 2 and 3 can be found from symmetry by rotating the system:

$$s_2(t) = \mathbf{D}_s(\vec{c}_1, \vec{a}_2, \vec{b}_3, \hat{\Omega}, f) : \mathbf{h}(f, t, \vec{x_2}),$$

$$s_3(t) = \mathbf{D}_s(\vec{b}_1, \vec{c}_2, \vec{a}_3, \hat{\Omega}, f) : \mathbf{h}(f, t, \vec{x_3}). \tag{4.8}$$

We are now ready to find the A, E and T detector responses to a plane gravitational wave. To simplify matters we write the signal in the form

$$s_n(t) = \mathbf{D}_n(\hat{\Omega}, f) : \mathbf{h}(f, t, \vec{x_0}), \tag{4.9}$$

where n takes the values A, E and T, which correspond to the three noise orthogonal data channels, and $T_n^a = T_n(f, \vec{a}$. The geometrical factor $\mathbf{D}_n(\hat{\Omega}, f)$ is given as

$$\mathbf{D}_n(\hat{\Omega}, f) = \vec{a} \otimes \vec{a}\ T_n^a + \vec{b} \otimes \vec{b}\ T_n^b + \vec{c} \otimes \vec{c}\ T_n^c. \tag{4.10}$$

We define our reference point $\vec{x_0}$ to be the center of the triangle, and write

$$\mathbf{h}(f, t, \vec{x}) = e^{-i2\pi f \hat{\Omega}\cdot(\vec{x}-\vec{x_0})}\mathbf{h}(f, t, \vec{x_0}). \tag{4.11}$$

The T channel, which is also called the symmetrized Sagnac, has an obvious cyclic symmetry:

$$T_T^a = T_T^b = T_T^c = T_T, \tag{4.12}$$

where

$$T_T(\vec{u_2}\cdot\hat{\Omega}, f) = \frac{e^{-i\frac{f_n}{3}\left(9+(\vec{u_1}-\vec{u_3})\cdot\Omega\right)}}{6\sqrt{3}}\Big(1+2\cos(2f_n)\Big)\Big[\mathrm{sinc}\Big(f_n(1+\vec{u_2}\cdot\hat{\Omega})\Big) - \mathrm{sinc}\Big(f_n(1-\vec{u_2}\cdot\hat{\Omega})\Big)\Big] \tag{4.13}$$

The variable A, on the other hand, does not have this nice symmetry:

$$T_A^a(\vec{a}\cdot\hat{\Omega}, f) = \frac{-i}{3\sqrt{2}}\sin(f_n)e^{-i\frac{f_n}{3}\left(6+(\vec{c}-\vec{b})\cdot\Omega\right)}\Big[\mathrm{sinc}\Big(f_n(1+\vec{a}\cdot\hat{\Omega})\Big) + e^{-2if_n}\mathrm{sinc}\Big(f_n(1-\vec{a}\cdot\hat{\Omega})\Big)\Big], \tag{4.14}$$

$$T_A^b(\vec{b}\cdot\hat{\Omega}, f) = \frac{-i}{3\sqrt{2}}\sin(f_n)e^{-i\frac{f_n}{3}\left(6+(\vec{a}-\vec{c})\cdot\Omega\right)}\Big[e^{-2if_n}\mathrm{sinc}\Big(f_n(1+\vec{b}\cdot\hat{\Omega})\Big) + \mathrm{sinc}\Big(f_n(1-\vec{b}\cdot\hat{\Omega})\Big)\Big], \tag{4.15}$$

$$T_A^c(\vec{c}\cdot\hat{\Omega},f)=\frac{-i}{3\sqrt{2}}\sin(f_n)e^{-i\frac{f_n}{3}\left(9+(\vec{b}-\vec{a})\cdot\Omega\right)}\Big[\mathrm{sinc}\Big(f_n(1+\vec{c}\cdot\hat{\Omega})\Big) +\mathrm{sinc}\Big(f_n(1-\vec{c}\cdot\hat{\Omega})\Big)\Big], \quad (4.16)$$

nor does the variable E:

$$\begin{aligned}T_E^a(\vec{a}\cdot\hat{\Omega},f)=\frac{1}{6\sqrt{6}}\Big[&\mathrm{sinc}\Big(f_n(1+\vec{a}\cdot\hat{\Omega})\Big)\Big(e^{-i\frac{f_n}{3}\left(9+(\vec{c}-\vec{b})\cdot\hat{\Omega}\right)}+e^{-i\frac{f_n}{3}\left(3+(\vec{c}-\vec{b})\cdot\hat{\Omega}\right)}\\&-2e^{-i\frac{f_n}{3}\left(15+(\vec{c}-\vec{b})\cdot\hat{\Omega}\right)}\Big)+\mathrm{sinc}\Big(f_n(1-\vec{a}\cdot\hat{\Omega})\Big)\Big(2e^{-i\frac{f_n}{3}\left(3+(\vec{c}-\vec{b})\cdot\hat{\Omega}\right)}\\&-e^{-i\frac{f_n}{3}\left(15+(\vec{c}-\vec{b})\cdot\hat{\Omega}\right)}-e^{-i\frac{f_n}{3}\left(9+(\vec{c}-\vec{b})\cdot\hat{\Omega}\right)}\Big)\Big], \quad (4.17)\end{aligned}$$

$$\begin{aligned}T_E^b(\vec{b}\cdot\hat{\Omega},f)=\frac{1}{6\sqrt{6}}\Big[&\mathrm{sinc}\Big(f_n(1+\vec{b}\cdot\hat{\Omega})\Big)\Big(e^{-i\frac{f_n}{3}\left(15+(\vec{a}-\vec{c})\cdot\hat{\Omega}\right)}+e^{-i\frac{f_n}{3}\left(9+(\vec{a}-\vec{c})\cdot\hat{\Omega}\right)}\\&-2e^{-i\frac{f_n}{3}\left(3+(\vec{a}-\vec{c})\cdot\hat{\Omega}\right)}\Big)+\mathrm{sinc}\Big(f_n(1-\vec{b}\cdot\hat{\Omega})\Big)\Big(2e^{-i\frac{f_n}{3}\left(15+(\vec{a}-\vec{c})\cdot\hat{\Omega}\right)}\\&-e^{-i\frac{f_n}{3}\left(9+(\vec{a}-\vec{c})\cdot\hat{\Omega}\right)}-e^{-i\frac{f_n}{3}\left(3+(\vec{a}-\vec{c})\cdot\hat{\Omega}\right)}\Big)\Big], \quad (4.18)\end{aligned}$$

$$\begin{aligned}T_E^c(\vec{c}\cdot\hat{\Omega},f)=\frac{1}{6\sqrt{6}}\Big[&\mathrm{sinc}\Big(f_n(1+\vec{c}\cdot\hat{\Omega})\Big)\Big(e^{-i\frac{f_n}{3}\left(3+(\vec{b}-\vec{a})\cdot\hat{\Omega}\right)}+e^{-i\frac{f_n}{3}\left(15+(\vec{b}-\vec{a})\cdot\hat{\Omega}\right)}\\&-2e^{-i\frac{f_n}{3}\left(9+(\vec{b}-\vec{a})\cdot\hat{\Omega}\right)}\Big)+\mathrm{sinc}\Big(f_n(1-\vec{c}\cdot\hat{\Omega})\Big)\Big(2e^{-i\frac{f_n}{3}\left(9+(\vec{b}-\vec{a})\cdot\hat{\Omega}\right)}\\&-e^{-i\frac{f_n}{3}\left(3+(\vec{b}-\vec{a})\cdot\hat{\Omega}\right)}-e^{-i\frac{f_n}{3}\left(15+(\vec{b}-\vec{a})\cdot\hat{\Omega}\right)}\Big)\Big]. \quad (4.19)\end{aligned}$$

4.3 Noise Spectral Density

Until now we have only considered the gravitational wave contribution, $\phi_{ij}(t)$, to the time-varying part of the phase $\Phi_{ij}(t)$. Our next task is to account for the

instrument noise contributions. There are three main noise sources: the laser phase noise $C(t)$, the position noise $n^p(t)$ and the acceleration noise $n^a(t)$.

The total phase variation is given by

$$\Phi_{ij}(t) = C_i(t - L_{ij}) - C_j(t) + \phi_{ij}(t) + n^p_{ij}(t) - \hat{x}_{ij} \cdot [\vec{n}^a_{ij}(t) - \vec{n}^a_{ji}(t - L_{ij})]. \quad (4.20)$$

The position noise $n^p_{ij}(t)$ includes shot noise and pointing jitter in the measurement of the signal sent by spacecraft i and measured by the photo-detector in spacecraft j. The acceleration noise $\vec{n}^a_{ij}(t)$ is from the gravitation reference system in spacecraft j along the axis that points toward spacecraft i. The phase noise associated with the laser on spacecraft i is denoted $C_i(t)$. It is easy to show that the phase noise cancels in a rigid, non-rotating Sagnac interferometer. More complicated second generation Sagnac variables can be constructed to account for the rotation and flexing of the array[48, 49]. For simplicity we work with the basic Sagnac variables as they give results that are almost identical to those found using the second generation variables.

We assume that all the interferometer arms are of approximately equal length ($L = 5 \times 10^7\,\mathrm{m}$), and that the noise spectral densities $S_n(f)$ are similar on each spacecraft. The noise transfer functions are then given by

$$S^T_n(f) = 2\left[1 + 2\cos(2f_n)\right]^2 \left[S^p_n(f) + 4\sin^2(f_n) S^a_n(f)\right], \quad (4.21)$$

where according to the fiducial BBO design

$$S^p_n(f) = \frac{2.0 \times 10^{-34}}{(3L)^2}\,\mathrm{Hz}^{-1},$$
$$S^a_n(f) = \frac{9.0 \times 10^{-34}}{(2\pi f)^4 (3L)^2}\,\mathrm{Hz}^{-1}. \quad (4.22)$$

This expression for the Symmeterized Sagnac noise transfer function was previously derived in Refs. [47, 43]. The noise transfer functions in the A and E channel share the same form, as first pointed out in Ref. [43]:

$$S_n^A(f) = S_n^E(f) = 8\sin^2(f_n)\Big[2\Big(3 + 2\cos(2f_n) + \cos(4f_n)\Big)S_n^a(f) \tag{4.23}$$

$$+\Big(2 + \cos(2f_n)\Big)S_n^s(f)\Big]. \tag{4.24}$$

4.4 Cross-Correlation of Two Detectors

The CGB signal can be extracted from the instrument noise by cross-correlating the outputs of two independent interferometers. The pair of co-planar interferometers of the BBO do not share any common components, so the noise in each detector should be largely uncorrelated. Possible correlated sources of noise include solar flares and fluctuations in the refractive index of the inter-planetary medium. Another potential source of correlated noise is the residual from subtracting foreground sources such as double neutron star binaries [38, 39]. Here we will assume that any correlated sources of noise are well below the level of the CGB.

We assume that the CGB is stationary, Gaussian, isotropic, and unpolarized. The background can be expanded in terms of plane waves:

$$h_{ij}(t,\vec{x}) = \sum_A \int_{-\infty}^{\infty} df \int d\hat{\Omega}\, \tilde{h}_A(f,\hat{\Omega}) e^{-2\pi i f(t-\hat{\Omega}\cdot\vec{x})} \epsilon_{ij}^A(\hat{\Omega}), \tag{4.25}$$

where $\epsilon^A(\hat{\Omega})$ are polarization tensors given in term of the basis tensors

$$\epsilon^+(\hat{\Omega},\psi) = \mathbf{e}^+(\hat{\Omega})\cos 2\psi - \mathbf{e}^\times(\hat{\Omega})\sin 2\psi,$$

$$\epsilon^{\times}(\hat{\Omega},\psi) = \mathbf{e}^{+}(\hat{\Omega})\sin 2\psi + \mathbf{e}^{\times}(\hat{\Omega})\cos 2\psi. \tag{4.26}$$

The basis tensors can be expressed in term of an orthonormal set of unit vectors $\hat{m}$, $\hat{n}$ and $\hat{\Omega}$ as

$$\mathbf{e}^{+}(\hat{\Omega}) = \hat{m}\otimes\hat{m} - \hat{n}\otimes\hat{n},$$

$$\mathbf{e}^{\times}(\hat{\Omega}) = \hat{m}\otimes\hat{n} + \hat{n}\otimes\hat{m}. \tag{4.27}$$

From the strain

$$S(\hat{\Omega},f,t) = \mathbf{D}(\hat{\Omega},f) : (h^{+}(f,t,\vec{x_0})\epsilon^{+}(\hat{\Omega},\psi) + h^{\times}(f,t,\vec{x_0})\epsilon^{\times}(\hat{\Omega},\psi)), \tag{4.28}$$

we find that after averaging over polarizations, the cross-correlated signal of two detectors in the presence of such a background is given by

$$\langle S_1(t)S_2(t)\rangle = \int_0^{\infty} df\, S_h(f)R_{12}(f), \tag{4.29}$$

where $S_h(f)$ is the total power spectral density due to both polarizations:

$$S_h(f) = S_h^{+}(f) + S_h^{\times}(f), \tag{4.30}$$

and

$$R_{12}(f) = \sum_{\alpha}\int \frac{d\Omega}{8\pi} F_1^{\alpha *}(\hat{\Omega},f)F_2^{\alpha}(\hat{\Omega},f), \tag{4.31}$$

where the sum is over the two polarization α. The transfer function R_{12} is a purely geometric factor that accounts for the overlap of the antenna patterns of the two detectors. The antenna pattern functions F are given by

$$F^{\alpha}(\hat{\Omega},f) = \mathbf{D}(\hat{\Omega},f) : \mathbf{e}^{\alpha}(\hat{\Omega}). \tag{4.32}$$

The optimal signal-to-noise ratio squared is given by [40, 41]

$$\mathrm{SNR}_C^2 = 2T \int_0^\infty df\, S_h^2(f) \frac{|R_{12}(f)|^2}{S_{n_1}(f) S_{n_2}(f)}. \tag{4.33}$$

where t is the time of observation, S_{n_1} is the noise spectral density of interferometer 1, S_{n_2} is the noise spectral density of for interferometer 2 and S_h is the spectral density of the CGB. A signal to noise ratio of SNR = 3.3 indicates that the CGB has been detected at 95% confidence, with a 5% false alarm probability [41].

The power spectral density of the CGB is related to the energy density in gravitational waves per logarithmic frequency interval, $\Omega_{gw}(f)$ (in units of the critical denisty), by

$$S_h(f) = \frac{3H_0^2}{4\pi^2} \frac{\Omega_{gw}}{f^3}. \tag{4.34}$$

Standard inflationary models predict that $\Omega_{gw}(f)$ will be roughly scale invariant, with an amplitude $\Omega_{gw} \sim 10^{-15}$ in the $f = 1\,\mathrm{Hz}$ region.

The contribution to the cross-correlated SNR per logarithmic frequency interval can be written as

$$\frac{d\,\mathrm{SNR}_C^2}{d\ln f} = \frac{h_{\mathrm{opt}}^4(f)}{h_{\mathrm{eff}}^4(f)} \tag{4.35}$$

where $h_{\mathrm{eff}}(f)$ is the effective sensitivity curve

$$\tilde{h}_{\mathrm{eff}}(f) = \sqrt{\frac{S_n(f)}{|R_{12}(f)|}} \tag{4.36}$$

and $h_{\mathrm{opt}}(f)$ is the optimally filtered CGB signal

$$h_{\mathrm{opt}}(f) = (2Tf)^{1/4} \sqrt{S_h(f)}\,. \tag{4.37}$$

These definitions are equivalent to the usual definitions used to plot sensitivity curves and gravitational wave signals for coherent gravitational wave sources. The main difference is that the optimally filtered signal strength grows as $T^{1/2}$ with coherent matched filtering, while it only grows as $T^{1/4}$ for cross-correlated stochastic signals.

4.5 Numerical Analysis

The optimal SNR for the BBO comes from combining the full set of independent interferometry channels in each of the two co-located detectors that form the star constellation:

$$\mathrm{SNR}^2_{\mathrm{opt}} = \sum_{\alpha=A_1,E_1,T_1} \sum_{\beta=A_2,E_2,T_2} \mathrm{SNR}^2_{\alpha\beta}\,. \tag{4.38}$$

Our first task is to calculated the geometrical overlap of each pair of channels, $R_{\alpha\beta}(f)$. The all-sky integral in equation 4.31 was performed numerically using the *HEALPIX* package [50]. Plots of the overlap factors are shown in figures 4.5-4.5 for the standard BBO configuration in which the two overlapping detectors form a symmetric six pointed star. The plots show the R's scaled by overall factors such as $\sin^2(f_n)$, which they share in common with the corresponding noise transfer functions.

We expect R_{12} to vanish for the cross terms as the A, E and T channels are approximately signal orthogonal. In the low frequency limit the A and E can be shown [44] to be equivalent to Cutler's s_I and s_{II} [51] variables, which describe two Michelson detectors rotated by an angle $\pi/4$. Combining the geometrical factors R_{12}

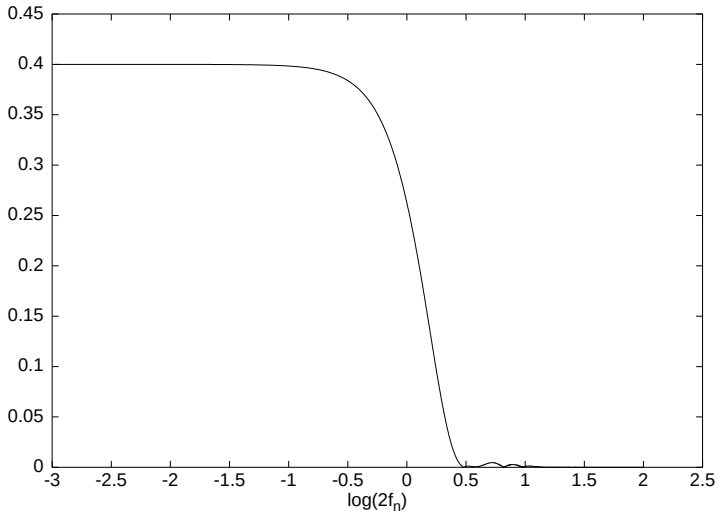

Figure 4.1: $R_{12}(f_n)/\sin^2(f_n)$ for $A_1 \times A_2$

with the noise transfer functions leads to the effective sensitivity curves shown in figures 4.5 and 4.5.

The combined effective sensitivity follows from the optimal signal to noise ratio (eq. 4.38) . Figure 4.5 shows the combined sensitivity curve using all channel combinations plotted against the optimal CGB signal for a scale invariant spectrum with $\Omega_{gw} = 10^{-15}$.

An alternative way of conveying the information contained in figure 4.5 is to plot $\mathrm{SNR}(f) = (d\mathrm{SNR}^2(f)/d\ln f)^{1/2}$: the contribution to the signal to noise ratio per logarithmic frequency interval. The optimal $\mathrm{SNR}(f)$ for $\Omega_{gw} = 10^{-15}$ is shown in Figure 4.5.

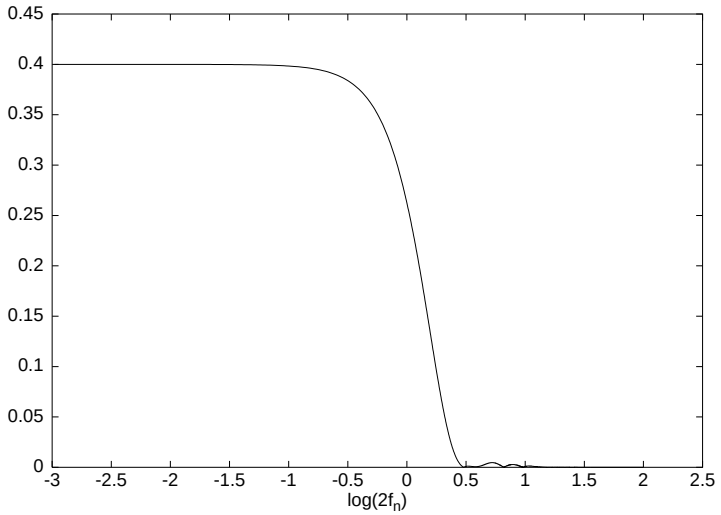

Figure 4.2: $R_{12}(f_n)/\sin^2(f_n)$ for $E_1 \times E_2$

The preceding graphs assumed that the two triangular interferometers formed a symmetrical six pointed star. However, one could consider alternative arrangements where the two detectors are rotated by an arbitrary angle λ with respect to one another. In our numbering convention for the vertices of each triangle the symmetric star corresponds to a rotation angle of $\lambda = \pi$. As we vary λ, the individual SNRs from $A_1 \times A_2$ and $E_1 \times E_2$ decrease, with minima at $\lambda = \pi/4$ and $\lambda = 3\pi/4$ as expected [47]. The SNR for $A_1 \times E_2$, on the other hand, increases, with maxima at $\lambda = \pi/4$ and $\lambda = 3\pi/4$. This behavior is illustrated in figures 4.5 and 4.5. The net effect is that the optimal SNR is independent of the relative orientation λ.

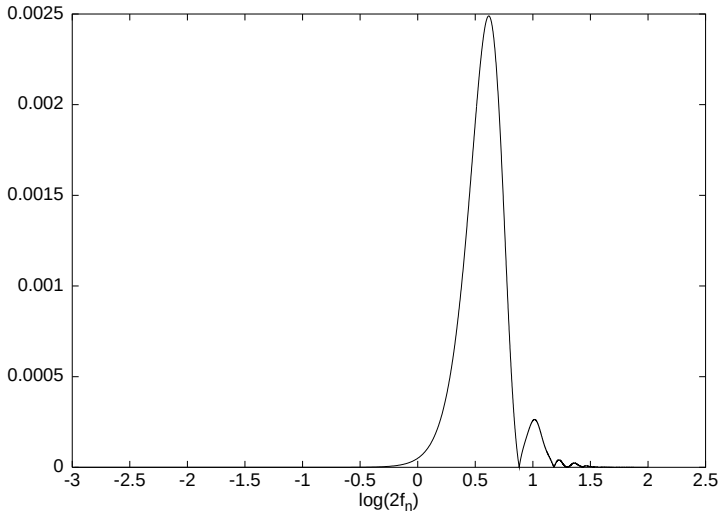

Figure 4.3: $R_{12}(f_n)/(1+2\cos(2f_n))^2$ for $T_1 \times T_2$

Using equation 4.33 and 4.38 we find that the optimal SNR for scale invariant CGB that can be achieved by the fiducial BBO design is equal to

$$\mathrm{SNR}_{\mathrm{opt}} = 155\sqrt{\frac{T}{5\mathrm{yr}}}\frac{\Omega_{gw}}{10^{-15}}\left(\frac{H_0}{70\,\mathrm{km\,s^{-1}\,Mpc^{-1}}}\right)^2, \tag{4.39}$$

which is well above the 3.3 threshold mentioned in section 4.4. Conversely, the minimum Ω_{gw} for which we could detect the CGB with the 95% confidence is equal to $2.2 \times 10^{-17}(5\mathrm{yr}/T)^{1/2}(70\,\mathrm{km\,s^{-1}\,Mpc^{-1}}/H_0)^2$. Our findings agree with the recent independent calculation by Seto [52].

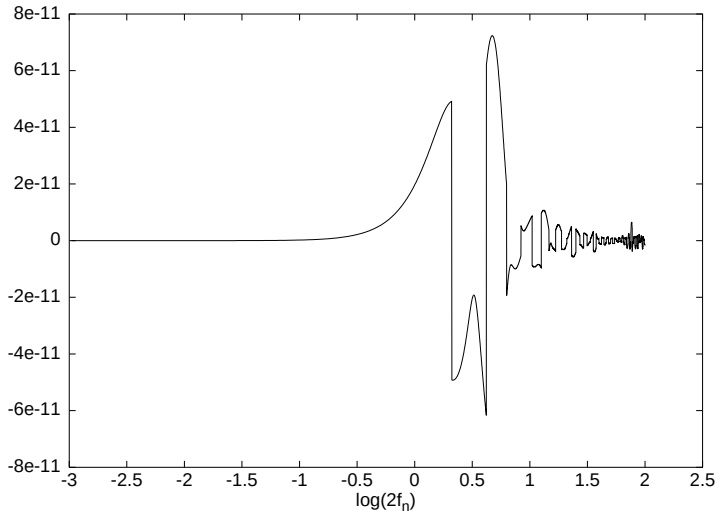

Figure 4.4: $R_{12}(f_n)/((1+2\cos(2f_n))\sin(f_n))$ for $A_1 \times T_2$ or $T_1 \times A_2$

4.6 Conclusion

We have determined that the fiducial BBO design would be able to detect a scale invariant CGB with an energy density as low as

$$\Omega_{gw} = 2.2 \times 10^{-17} (5\mathrm{yr}/T)^{1/2} (70\,\mathrm{km\,s^{-1}\,Mpc^{-1}}/H_0)^2\,, \tag{4.40}$$

which is much lower than any other existing limits. The BBO will either detect the CGB, or place a much stronger constraint than the one currently known (chapter 3). We found as well that the optimal sensitivity is independent of the relative orientation of the co-planar detectors used to perform the cross correlation.

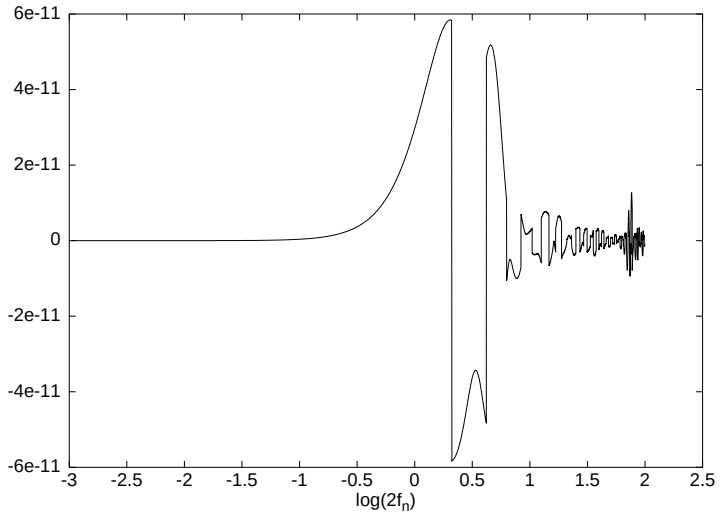

Figure 4.5: $R_{12}(f_n)/((1+2\cos(2f_n))\sin(f_n))$ for $E_1 \times T_2$ or $T_1 \times E_2$.

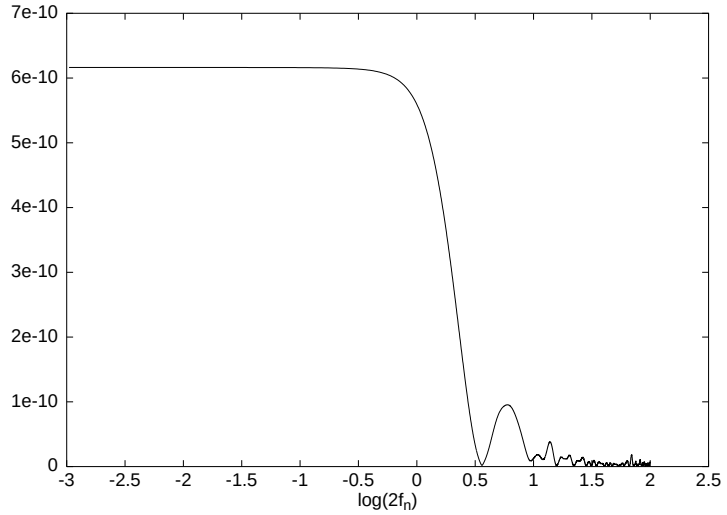

Figure 4.6: $R_{12}(f_n)/\sin^2(f_n)$ for $A_1 \times E_2$ or $E_1 \times A_2$.

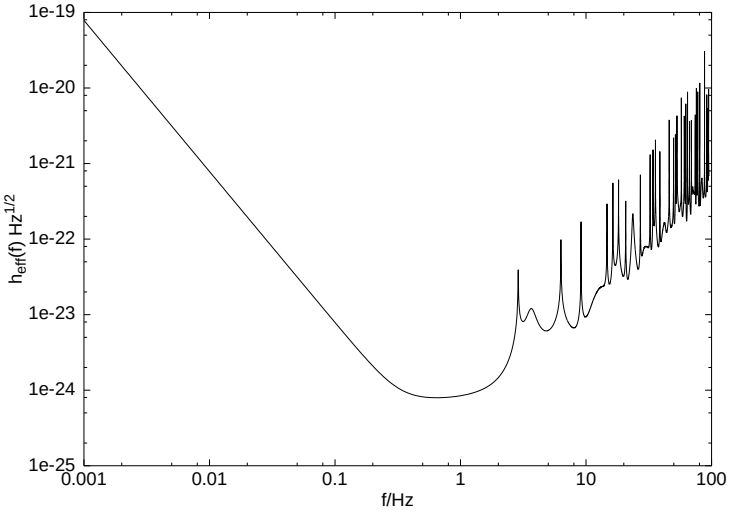

Figure 4.7: Effective sensitivity for $A_1 \times A_2$ ($E_1 \times E_2$)

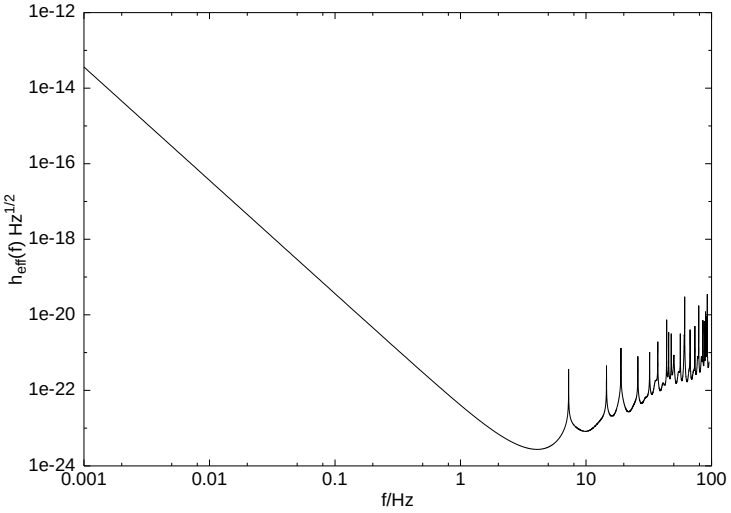

Figure 4.8: Effective sensitivity for $T_1 \times T_2$

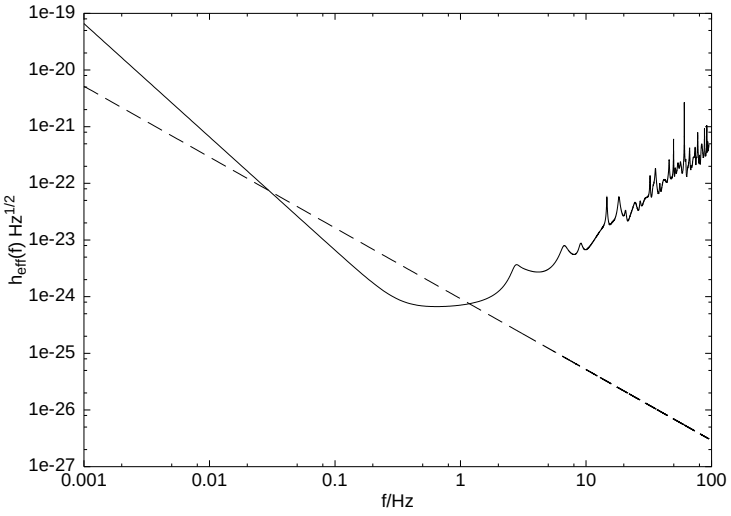

Figure 4.9: The combined sensitivity curve (solid line) plotted against the optimal CGB signal (dashed line) for an observation time of $T = 1$yr.

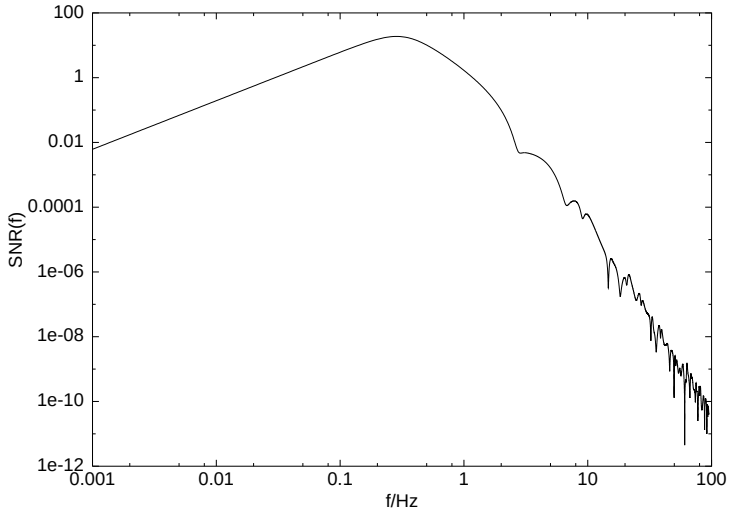

Figure 4.10: Optimal SNR(f)

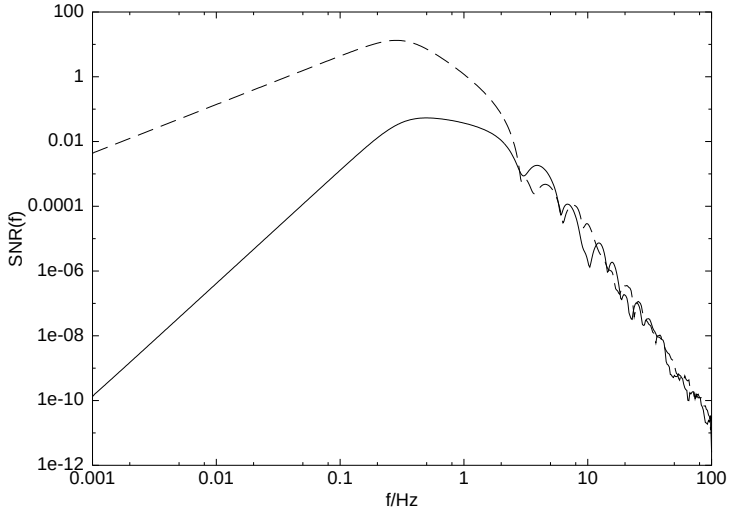

Figure 4.11: $\mathrm{SNR}_{A_1A_2}(f)$ for an angle of $\lambda = \pi$ (dashed line) and $\lambda = \pi/4$ (solid line).

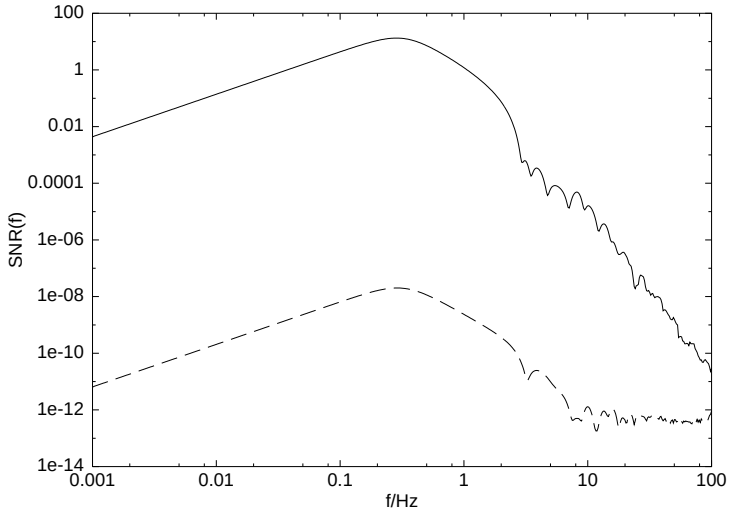

Figure 4.12: $\mathrm{SNR}_{A_1E_2}(f)$ for an angle of $\lambda = \pi$ (dashed line) and $\lambda = \pi/4$ (solid line).

CHAPTER 5

BINARY SYSTEMS: ASTROPHYSICAL SOURCES OF GRAVITATIONAL WAVES

5.1 Introduction

The fundamental mechanisms ruling the Universe can be explored by directly "looking" into the birth of the Universe. The studies on the CGB and CMB intend to do so. Valuable information about the early stages of the evolution of the Universe can be obtained from astrophysical sources as well, since they are direct consequences of early events. In particular, galaxy mergers are very dependent on galaxy population models, which are in turn issued from different cosmological models. There is strong evidence that black holes are present at the center of most galaxies. When two galaxies merge, the black holes will sink to the center and form a binary system. Eventually their orbit will decay due to the gravitational radiation, and the two black holes will merge. The survey and study of black hole binary systems will allow us to place constraints on models of cosmological structure formation. Black holes, by definition, are mostly black, and therefore observations with telescopes aimed at detecting light are limited. So far mostly indirect studies have been performed. Since they are infinitely dense, they disturb the gravitational field around them so much that close objects display unique behaviors (e.g. strong gravitational lensing, abnormal stellar orbits) that indicate the presence of black holes as well as provide details about their characteristics. The detection of gravitational waves would on the other hand be

a direct observation, and would likely provide richer information. To decrypt these signals and extract this information, one needs to be able to predict the waveform emitted by the system under study. This chapter is dedicated to the description of the gravitational waveform produced by a binary system.

5.2 Matter and Gravitational Waves

To find the gravitational waveform produced by a mass distribution, the perturbed Einstein equations need to be solved. It will be assumed that the observer is far away from the source and the source is not relativistic. Since the amplitude of the waveform is inversely related to the distance to the source, the first condition insures that the use of perturbation theory is adequate. The last condition is actually equivalent to saying that the wavelength of the gravitational wave emitted is much bigger than the source radius, as will be shown below. In the Lorentz gauge, the perturbed Einstein equations take the form (eq. 2.14):

$$\partial^{\alpha}\partial_{\alpha}\bar{h}_{\mu\nu} = 16\pi T_{\mu\nu}\,, \tag{5.1}$$

where $\bar{h}_{\mu\nu}$ is the trace reverse tensor (eq. 2.12). The stress energy tensor does not vanish inside the source. To solve the system of differential equations for a general source, the Green function needs to be found. It is the solution to the equation

$$\partial^{\alpha}\partial_{\alpha}G\left(x^{\mu}-y^{\mu}\right) = \delta^{(4)}\left(x^{\mu}-y^{\mu}\right)\,, \tag{5.2}$$

where the derivatives are taken with respect to x^μ. The solution to this equation is well known [53]:

$$G\left(x^\mu - y^\mu\right) = -\frac{1}{4\pi|\tilde{x}-\tilde{y}|}\delta\left[|\tilde{x}-\tilde{y}| - \left(x^0 - y^0\right)\right]\theta\left(x^0 - y^0\right) , \tag{5.3}$$

where it was taken into account that the wave is propagating forward in time. Hence, only the retarded Green function was retained as solution. $\tilde{x}$ and $\tilde{y}$ are spatial vectors and $\theta(x^0 - y^0)$ equals 1 if $x^0 > y^0$, and 0 otherwise. The solution to equation 5.1 is given in terms of the Green function:

$$\begin{aligned}
\bar{h}_{\mu\nu}\left(t,\tilde{x}\right) &= -16\pi\int d^4y\, G\left(x^\mu - y^\mu\right) T_{\mu\nu}(y^\mu) \\
&= 4\int d^3y \int_{-\infty}^{x^0} dy^0\, \frac{1}{|\tilde{x}-\tilde{y}|}\delta\left[y^0 - \left(x^0 - |\tilde{x}-\tilde{y}|\right)\right] T_{\mu\nu}\left(y^0,\tilde{y}\right) \\
&= 4\int d^3y\, \frac{1}{|\tilde{x}-\tilde{y}|} T_{\mu\nu}\left(x^0 - |\tilde{x}-\tilde{y}|,\tilde{y}\right) .
\end{aligned} \tag{5.4}$$

Since the observer is located at $\vec{x}$, time is defined as $t = x^0$, and the retarded time , $t_r = t - |\tilde{x}-\tilde{y}|$ is the time at which a photon would have been emitted at $\tilde{y}$ if it reached $\tilde{x}$ at t. In other words, all the energy and momentum sources in the past light cone of an observer at $\vec{x} \to (t,\tilde{x})$ contribute to the creation of the metric perturbation at $\vec{x}$, which indicates once more that gravitational waves travel at the speed of light.

The Fourier transform of equation 5.4 yields:

$$\begin{aligned}
\tilde{\bar{h}}_{\mu\nu}\left(\omega,\tilde{x}\right) &= \frac{4}{\sqrt{2\pi}}\int dt d^3y\, e^{i\omega t}\frac{T_{\mu\nu}\left(t-|\tilde{x}-\tilde{y}|,\tilde{y}\right)}{|\tilde{x}-\tilde{y}|} \\
&= \frac{4}{\sqrt{2\pi}}\int dt d^3y\, e^{i\omega t_r} T_{\mu\nu}\left(t_r,\tilde{y}\right)\frac{e^{i\omega|\tilde{x}-\tilde{y}|}}{|\tilde{x}-\tilde{y}|} ,
\end{aligned} \tag{5.5}$$

where a change of variable from t to t_r was performed between the first and second line. The former assumption concerning the wavelength of the gravitational wave and

the distance of the observer from the source can be used to simplify the integral, and find a solution. Since the wavelength ω^{-1} is big compared to the size of the source, the function $e^{i\omega|x-y|}$ does not vary much during the integration. Also, since the distance from the source to the observer is very big compared to the size of the source, the term $\frac{e^{i\omega|x-y|}}{|x-y|}$ can be considered constant upon integration, and equation 5.5 can be rewritten as

$$\tilde{\bar{h}}_{\mu\nu}(\omega, \tilde{x}) = 4\frac{e^{i\omega r}}{r}\int d^3y\, \tilde{T}_{\mu\nu}(\omega, \tilde{y}) \;, \tag{5.6}$$

Here r is the distance from the observer to a point of reference inside the source. In the case of a unequal mass binary system, the point of reference would usually be chosen to be the barycenter. The Lorentz condition, $\partial_\mu \bar{h}^{\mu\nu}(t, \tilde{x}) = 0$ can be expressed in the Fourier domain as:

$$\partial_\mu \bar{h}^{\mu\nu}(t, \tilde{x}) = \frac{1}{\sqrt{2\pi}}\int d\omega\, \partial_\mu \left(e^{i\omega t}\tilde{\bar{h}}^{\mu\nu}(\omega, \tilde{x})\right) = 0\,. \tag{5.7}$$

Since the perturbation in the frequency domain $\tilde{\bar{h}}^{\mu\nu}$ does not depend on t, the Lorentz condition becomes

$$\tilde{\bar{h}}^{0\nu} = -\frac{i}{\omega}\partial_j \tilde{\bar{h}}^{j\nu} \tag{5.8}$$

Hence, equation 5.6 needs only to be solved for the terms $\bar{h}^{j\nu}$. In turn, $\bar{h}^{j0}$ can be found with equation 5.8 in terms of $\partial_i \bar{h}^{ij}$, since the trace reverse tensor is symmetric in the Fourier space as well. In other words, all the components of the perturbation tensor in the Fourier space can be recovered from the sole knowledge of its spatial components.

The integral in equation 5.6 can be calculated using integration by parts:

$$\int d^3y\, \tilde{T}^{ij} = \int d^3y\, \partial_k \left(y^i \tilde{T}^{kj} \right) - \int d^3y\, y^i \partial_k \tilde{T}^{kj} \,. \tag{5.9}$$

Since the stress energy tensor vanishes at the surface of the source, and has the property $\partial_\mu T^{\mu\nu} = 0$, which leads to $-\partial_k \tilde{T}^{k\mu} = i\omega \tilde{T}^{0\mu}$, then

$$\begin{aligned} \int d^3y\, \tilde{T}^{ij} &= i\omega \int d^3y\, y^i \tilde{T}^{0j} \\ &= \frac{i\omega}{2} \int d^3y \left[y^i \tilde{T}^{0j} + y^j \tilde{T}^{0i} \right] , \end{aligned} \tag{5.10}$$

The second line was obtained by using the symmetry $\tilde{T}^{\mu\nu} = \tilde{T}^{\nu\mu}$. After integrating by parts a second time and removing the surface term, it becomes

$$\begin{aligned} \int d^3y\, \tilde{T}^{ij} &= -\frac{i\omega}{2} \int d^3y\, y^i y^j \left(\partial_l \tilde{T}^{0l} \right) \\ &= -\frac{\omega^2}{2} \int d^3y\, y^i y^j \tilde{T}^{00} \,. \end{aligned} \tag{5.11}$$

The resulting integral is usually defined as the quadrupole moment tensor:

$$I_{ij}(t) = \int d^3y\, y_i y_j T^{00}\left(t, \tilde{y}\right) \,. \tag{5.12}$$

In terms of the quadrupole moment, the gravitational wave tensor is written

$$\bar{\bar{h}}_{ij}\left(\omega, \tilde{x}\right) = -2\omega^2 \frac{e^{i\omega r}}{r} \tilde{I}_{ij}(\omega) \,, \tag{5.13}$$

It can now easily be Fourier transformed again to obtain an expression in the time domain:

$$\begin{aligned} \bar{h}_{ij}\left(t, \tilde{x}\right) &= \frac{2}{\sqrt{2\pi}} \int dt\, \omega^2 \frac{e^{i(\omega r - \omega t)}}{r} \tilde{I}_{ij}(\omega) \\ &= \frac{2}{\sqrt{2\pi}} \frac{1}{r} \frac{d^2}{dr^2} \int d\left(t - r\right) e^{-i\omega(t-r)} \tilde{I}_{ij}(\omega) \\ &= \frac{2}{r} \frac{d^2 I_{ij}}{dt^2}(t_r) \,. \end{aligned} \tag{5.14}$$

Equation 5.14 is the analytical expression for a gravitational wave emitted by any given source whose energy and momentum is described by the stress energy tensor $T^{\mu\nu}$. It can be applied to any system susceptible of producing gravitational radiation, such as binary systems.

5.3 Gravitational Radiation from Circular Binaries

Consider a binary system of two masses M_a and M_b, to which the assumptions from the previous section apply. For simplicity, their orbit is taken to be circular. The following calculations can be easily generalized to elliptical orbits. Given that the observer is located far away from the source, the masses can be treated as point sources. The coordinate system used is centered at the binary barycenter.

Since the source is slowly rotating, its orbit is Newtonian, and the time component of its stress energy tensor T^{00} is simply the mass density of the source. The positions of the two objects forming the binary are given by:

$$\begin{aligned} y_a^1 = R_a \cos\theta(t) \quad y_a^2 = R_a \sin\theta(t) \quad y_a^3 = 0 \\ y_b^1 = -R_b \cos\theta(t) \quad y_b^2 = -R_b \sin\theta(t) \quad y_b^3 = 0\,. \end{aligned} \tag{5.15}$$

The mass density is therefore

$$\begin{aligned} T^{00}\left(t,\tilde{x}\right) &= M_a \delta\left(y_a^3\right) \delta\left(y_a^1 - R_a\cos\theta(t)\right) \delta\left(y_a^2 - R_a \sin\theta(t)\right) \\ &\quad + M_b \delta\left(y_b^3\right) \delta\left(y_b^1 + R_b\cos\theta(t)\right) \delta\left(y_b^2 + R_b \sin\theta(t)\right)\,. \end{aligned} \tag{5.16}$$

The delta functions, due to the assumption the objects are point masses, make the calculation of the quadrupole moment tensor straight forward:

$$\begin{aligned} I_{11} &= \frac{1}{2}\left(M_a R_a^2 + M_b R_b^2\right)\left[1+\cos 2\theta(t)\right] \\ I_{22} &= \frac{1}{2}\left(M_a R_a^2 + M_b R_b^2\right)\left[1-\cos 2\theta(t)\right] \\ I_{12} &= I_{21} = \frac{1}{2}\left(M_a R_a^2 + M_b R_b^2\right)\sin 2\theta(t) \\ I_{i3} &= I_{3i} = 0\,. \end{aligned} \tag{5.17}$$

The radius of the orbit depends on the angular velocity. From Kepler's third law,

$$\begin{aligned} R_a &= \frac{M_b}{(M_a+M_b)^{\frac{2}{3}}\,\omega^{\frac{2}{3}}} \\ R_b &= \frac{M_a}{(M_a+M_b)^{\frac{2}{3}}\,\omega^{\frac{2}{3}}} \end{aligned} \tag{5.18}$$

It follows that the quadrupole moment tensor in matrix representation is

$$I_{ij} \longrightarrow \frac{1}{2} M_c^{5/3}\omega^{-4/3}\begin{pmatrix} 1+\cos 2\theta(t) & \sin 2\theta(t) & 0 \\ \sin 2\theta(t) & 1-\cos 2\theta(t) & 0 \\ 0 & 0 & 0 \end{pmatrix}, \tag{5.19}$$

where the chirp mass M_c is defined as

$$M_c = \left[\frac{M_a M_b}{(M_a+M_b)^{\frac{1}{3}}}\right]^{\frac{3}{5}}. \tag{5.20}$$

If the orbital frequency ω were constant, then the masses' angular positions with respect to the barycenter would simply be $\theta(t) = \omega t + \theta_0$, in which case the gravitational waves would be emitted at a frequency twice the orbital frequency. The assumption that the system is not relativistic would then directly imply

$$v_{orb} = \omega_{orb} R \ll 1 \quad \Longleftrightarrow \quad R \ll \lambda_{GW}\,, \tag{5.21}$$

where R is the radius of the source. As predicted at the beginning of this chapter, the non-relativistic assumption is equivalent to asking for the wavelength of the gravitational wave to be much bigger than the source.

For a non-relativistic system, gravitational waves are fairly weak, and do not carry away a lot of energy. Therefore, it is a good approximation to consider the orbital frequency to be constant over relatively short periods of time. When studying these kinds of systems with LIGO or LISA, the approximation is valid during the early stages of the inspiral. For pulsar timing arrays, however, it is not so. The integral in equation 2.46, $H_{ij} = \int_{t_p - z_p}^{t_e - z_e} h_{ij}(u)\mathrm{d}u$, implies that the response of the detector will depend on gravitational waves emitted at two different times. Without loss of generality the origin of the z-axis can be placed at Earth, and the time t_e at which the photon reaches Earth can become the reference time t. Then $t_p - z_p$ can be rewritten as $t - d(1 - \cos\mu)$, where μ is the angle between the line of sights to the pulsar and to the binary system. Since the length d of the "detector" (Earth-pulsar distance) is big, the two times at which the gravitational wave is evaluated are very different. The orbital frequency, and therefore the frequency of the gravitational wave emitted, will have greatly changed in this amount of time. In comparison, for LISA or LIGO, the frequency might evolve on the scale of the observation time, but not in the time it takes a photon to travel along the detector arm. The frequency of the wave disturbing one end of the detector will be the same as the one disturbing the other end, and the

signal will therefore be monochromatic. This is not the case for pulsar timing. The evolution of the frequency can be found analytically.

The power radiating away from a gravitational source is [54]

$$P = -\frac{1}{5}\langle \frac{d^3 J_{ij}}{dt^3}\frac{d^3 J^{ij}}{dt^3}\rangle \,. \tag{5.22}$$

J_{ij} is the reduced quadrupole moment

$$J_{ij} = I_{ij} - \frac{1}{3}\delta_{ij}\delta^{kl} I_{kl} \,. \tag{5.23}$$

The brackets denote an average over one period, and the minus sign indicates the system is loosing energy. Plugging equation 5.19 into equation 5.23, the reduced quadrupole moment is found to be

$$J_{ij} \longrightarrow \frac{1}{6} M_c^{5/3}\omega(t)^{-4/3} \begin{pmatrix} 1+3\cos 2\theta(t) & 3\sin 2\theta(t) & 0 \\ 3\sin 2\theta(t) & 1-3\cos 2\theta(t) & 0 \\ 0 & 0 & -2 \end{pmatrix} . \tag{5.24}$$

Both the angular position $\theta(t)$ and the angular velocity $\omega(t)$ depend on time. However, the angular velocity varies extremely slowly compared to the position. Over a complete orbit, $\omega(t)$ is constant to a very high accuracy. Therefore when calculating the power radiated away by the gravitational waves, the terms containing the time derivative of the angular velocity can be neglected. The third derivative of the reduced quadrupole moment is simply

$$\frac{d^3 J_{ij}}{dt^3} \longrightarrow 4 M_c^{5/3}\omega(t)^{5/3} \begin{pmatrix} \sin 2\theta(t) & -\cos 2\theta(t) & 0 \\ -\cos 2\theta(t) & -\sin 2\theta(t) & 0 \\ 0 & 0 & 0 \end{pmatrix} . \tag{5.25}$$

The power radiated away can readily be calculated:

$$P = -\frac{32}{5}\omega(t)^{10/3} M_c^{10/3} \,. \tag{5.26}$$

This is the rate at which the system loses its energy. The kinetic energy of the binary at instant t is

$$\begin{aligned} K(t) &= \frac{1}{2} M_a v_a(t)^2 + \frac{1}{2} M_b v_b(t)^2 \\ &= \frac{1}{2}\left(M_a R_a^2 + M_b R_b^2\right)\omega(t)^2 \\ &= \frac{1}{2} M_c^{5/3} \omega^{2/3} \,. \end{aligned} \tag{5.27}$$

Since the energy is approximately conserved over an orbital period, the Virial theorem applies:

$$E_{tot}(t) = -K(t) = -\frac{1}{2} M_c^{5/3} \omega^{2/3} \,. \tag{5.28}$$

The time derivative of the binary total energy is equivalent to the power radiated:

$$\frac{1}{3} M_c^{5/3} \omega^{-1/3} \dot{\omega} = \frac{32}{5} M_c^{10/3} \omega^{10/3} \tag{5.29}$$

This is a simple differential equation. Its solution is

$$\omega(t) = \left(\omega_o^{-8/3} - \frac{256}{5} M_c^{5/3}(t - t_o)\right)^{-3/8} \tag{5.30}$$

The orbital gravitational wave frequency will slowly increase with time. Equation 5.30 describes the evolution with respect to time of the orbital frequency of the system as long as it remains slowly evolving. As the system starts to evolve faster, the orbit

becomes relativistic, and post-Newtonian terms ($\sim M/r$) need to be included. The angular position can be found by integrating the angular velocity:

$$\begin{aligned}
\theta(t) &= \int_{t_o}^{t} dt\, \omega(t) \\
&= \int_{t_o}^{t} dt\, \left(\omega_o^{-8/3} - \frac{256}{5} M_c^{5/3}(t - t_o)\right)^{-3/8} \\
&= \theta_o + \frac{1}{32} M_c^{-5/3} \left(\omega_o^{-5/3} - \omega(t)^{-5/3}\right) . \qquad (5.31)
\end{aligned}$$

The results in this section along with the results from chapter 2.4 contain all the necessary tools to understand precisely how a circular non-relativistic binary system affects the timing of pulsars by radio-telescopes on Earth. The Next chapter discusses the current status of pulsar timing.

CHAPTER 6

PULSAR TIMING ARRAYS: A REVIEW

6.1 Introduction

It was theorized in the 1970's that gravitational waves could be detected by timing the pulses emitted by pulsars [55, 56, 57]. This could be achieved using radio telescope technologies in order to monitor the time of arrival of the pulses to Earth. These ideas were further developed by Hellings & Downs [58] and Foster & Backer [59]. Unfortunately, a gravitational perturbation would likely disturb the periodicity of a pulsar signal by at most 100 nanoseconds, which was far below the sensitivity that could be achieved in the 1980's. The challenges involved in detecting such a small change are significant. They consist of technical challenges, with precise instruments required, as well as theoretical challenges, as one needs to understand pulsar behaviour and other physical factors that will affect the periodicity of the signal independently from gravitational waves. However, recent improvements in instruments and theory have made of pulsar timing one of the most promising candidates for the first detection of gravitational waves. Consequently, there has been an international effort in the last decade toward the timing of pulsar arrays with existing or projected radio observatories. Currently there are three major pulsar timing array projects:

- The North American Nanohertz Gravitational Wave Observatory (NANOGrav) [60], featuring the Arecibo (Puerto Rico) and Green Bank (USA) telescopes. Of note,

the Arecibo observatory discovered the first binary pulsar in 1975, providing the strongest evidence for the existence of gravitational waves (see Chapter 2).

- The European Pulsar Timing Array project (EPTA) [61], ,which uses telescopes in Nancay (France), Jodrell Bank (United Kingdom), Effelsberg (Germany) and Westerbork (Netherlands). A fifth telescope currently under construction (Italy), will join the EPTA.
- The Parkes Pulsar Timing Array project (PPTA) [62, 63], located at the Parkes radio telescope (Australia). The PPTA has been collecting data for the past 5 years.

In addition to these three efforts, plans are being made to develop a much larger array of radio telescopes. The Square Kilometer Array (SKA) [64, 65] will likely be built in Australia or South Africa. It is expected that it will be able to reach much greater sensitivity than the older generation pulsar timing arrays.

Isolating the effect of gravitational waves on a pulsar signal requires a consistent period for pulse emission. Even though pulsars are very accurate "clocks" in general, their intrinsic accuracy is not sufficient. It is necessary to have 20 pulsars timed with an rms timing residual of $100\,ns$ or less over five years in order to detect a gravitational wave background [66]. The gravitational wave background is believed to be the most likely first detectable feature. Most pulsars don't have an orbit stable enough to ensure such measurements. To improve the quality of the measurement, PTAs use only millisecond pulsars. The short orbital period of millisecond pulsars implies they

have very large angular momenta, and are therefore more stable. They are thus less prone to starquakes or other astrophysical phenomena that might affect their orbital period. Currently, there are 37 millisecond pulsars being timed by PTAs [67]. Of these 37 only a few meet the required standard of $100\,ns$ rms. Of the others, 17 have uncertainties in the measurement of times of arrival larger than $500\,ns$, while the best has a rms of $60\,ns$ [68, 67]. The uncertainties in time of arrivals arise from the noise in the measurements and from irregularities in the orbital period of the pulsars. However as the time of observation increases, these irregularities are averaged out. That is to say, the longer the experiment, the lower the obtained rms timing residuals, though this effect can be limited in the presence of low frequency irregularities (e.g. 'timing noise") [69]. In the search for gravitational waves, the required observation time will be of the order of one decade. Over this time scale, it is predicted that an array of approximately 20 pulsars with rms around the $100\,ns$ threshold could be constructed [70].

6.2 Sources of Gravitational Waves Detectable by PTAs

Pulsar timing arrays (PTAs) are sensitive to gravitational wave frequencies between $f = 10^{-9}\,\text{Hz}$ and $f = 10^{-6}\,\text{Hz}$. The lower bound is set by the observation time, 30 years being a reasonable cut-off, while the upper bound is set by the sample rate, with once per week as the goal. There is little motivation to use higher sample rates as PTAs operate in the short wavelength limit - the distance to each pulsar is larger

than the wavelength of the gravitational waves - and therefore the sensitivity falls off as $1/f$ across the band.

A variety of sources are known to have the potential for emission in this range. They can be classified into three categories: individual persistent sources, individual burst sources and gravitational wave background.

6.2.1 Individual Persistent Sources

In chapter 5, it was shown that binary systems emit gravitational waves at a frequency twice as large as the orbital frequency. Massive and supermassive black hole binaries ($> 10^8\, M_\odot$) will emit in the detection range and may produce gravitational waves strong enough to be detected by PTAs. Chapter 7 addresses the detection of such sources.

6.2.2 Individual Burst Sources

Many astrophysical events will emit detectable bursts of gravitational waves, some of which will be in the frequency range explored by PTAs [67]:

- Birth of a supermassive black hole [71].
- Highly eccentric supermassive black hole systems [72].
- Close encounters of massive objects [73].
- Cusps and kinks on cosmic strings [74].

6.2.3 Gravitational Wave Stochastic Background

The potential detection of gravitational wave stochastic background with PTAs has been extensively described in the literature (e.g. REF). The background is composed of numerous sources, some astrophysical and some cosmological. The astrophysical background detectable by PTAs will be composed of massive and supermassive black hole binaries in the early stages of their orbital evolution, which emit too weakly to be individually identified [75, 76, 77, 78]. It may also include the gravitational waves emitted during the formation of primordial intermediate-mass black holes ($\sim 600\,M_{\odot}$)[79], occurring at the end of inflation. The cosmological background may also include radiation from cosmic strings and relic gravitational waves from the early Universe, as described in Chapter 3.

6.3 Noise in Pulsar Timing Data

Many different types of uncertainty enter into the measurement of the pulse arrival times combine to create a significant noise in the pulsar timing data. This section describes some types of noise commonly encountered in pulsar timing.

6.3.1 Model Errors

Pulsar timing is based on our capacity to accurately predict the 'normal' pulsar signal time of arrival at Earth, the departures from which are obtained and analyzed. These constitute the timing residuals. A slight error exists in the spin-down models, which describe the rotational evolution of the pulsars under study. This error will

yield additional residuals to those created by gravitational waves propagating through space. The model can be refined from the data, but this refinement will not be perfect and noise will therefore remain at some level.

6.3.2 Glitches and Timing Noise

Although the rotational periods of pulsars are usually very consistent with spin-down models, irregularities can occur. They come in two types: glitches which are characterized by a sudden increase in the rotational velocity, followed by a period of relaxation [80, 81]; and timing noise, which was thought to be continuous and erratic fluctuation in the rotation rate [80], but has recently been shown to be quasi-periodic [82]. Unlike glitches, the timing noise irregularities oscillate over large time scales ($1 - 10\,years$). The mechanisms underlying glitches and timing noise are not yet fully understood, and therefore cannot presently be incorporated into spin-down models.

6.3.3 Instrumental Noise

Much uncertainty in analysis is induced by the use of imperfect instruments. The difficulty in calibration of instruments for such a precise experiment will certainly play a role in the accuracy of the data [66]. Also, since PTAs rely on time measurements, irregularities in terrestrial standards will also add to this noise [83].

Finally, it is worth noting that although the noise spectrum is often considered 'white', it has been shown that it is actually slightly 'red', meaning its amplitude decreases with frequency. This makes the analysis additionally complex.

6.4 Current Achievements

Although PTAs have not yet achieved a direct detection of gravitational waves, the studies of existing data sets have already produced some interesting results. First, the non-detection of the stochastic background so far has provided many clues: this has placed constraints on theories for the formation of primordial intermediate-mass black holes [67], and recently, given insights into the abundance of cosmic strings [84] and into the properties of their tension [85]. Also in 2004, Jenet et al. [86] utilised data sets from the timing of pulsar PSR B1855+09 to disprove the hypothesis by Sudou et al. [87] that a supermassive black hole binary was present in galaxy 3C 66B. For a more complete review of Pulsar Timing Arrays and their achievements, see [67, 68].

The quantity of information that has been drawn from what is just the beginning of the PTA era provides reassurance of the future potential. With longer data sets, the uncertainty in the residuals will diminish. Combined with the rapid improvement of instruments and understanding of pulsars, and with the development of a new generation of pulsar timing arrays (SKA), it seems likely that a direct detection of gravitational wave may be imminent. The next chapter explores in detail the

information on massive black hole binaries which can be extracted by studying their gravitational radiation using the precise timing of an array of millisecond pulsars.

CHAPTER 7

CHARACTERISING MASSIVE BLACK HOLE BINARIES WITH PULSAR TIMING ARRAYS

7.1 Introduction

The PTA operating range makes it an excellent tool to search for stochastic backgrounds produced by a population of slowly evolving supermassive black hole binaries (MBHBs) [75, 76, 77]. The idea is that the fluctuating time of arrivals caused by the gravitational waves will produce a correlated response across the PTA, with a characteristic dependence on the angle between each pair of pulsars [58]. Considerable work has gone into producing bounds on the amplitude of the stochastic background [58, 88, 89, 35] and the development of improved analysis techniques for future searches [66, 90, 91].

With any population there are always members that are nearer and brighter, and it has been predicted that several black hole binary systems should be individually resolvable when the diffuse background is detected [92]. As a prelude to the first detection, upper bounds have been placed on the maximum amplitude of individual systems using the Parkes Pulsar Timing Array [93]. When a detection is made, it has been shown that an analysis of the timing residuals imparted at the Earth can be used to constrain the amplitude of the signals to $\sim 30\%$, and the direction to $\Delta\Omega \sim 40\,\mathrm{deg}^2$ for a 100 pulsar array and a network signal to noise ratio of SNR $= 10$ [94, 95]. But the timing residuals imparted at the Earth only tell part of the story. In addition to

the disturbance at the Earth there is also the disturbance at the pulsar to consider. The pulsar component of the signal is usually ignored as it depends on the poorly constrained distance to each pulsar. In cross-correlation studies the pulsar terms average to zero as the projected distance to each pular is different, resulting in a different frequency and phase response to individual binaries. We show that it is possible to include the pulsar terms in the analysis by enlarging the parameter space to include the distance to each pulsar in the array. This doubles the signal power and allows the measurement of the mass and distance to the binary. As an added bonus, the pointing accuracy improves by an order of magnitude, improving the prospects for finding electromagnetic counterparts.

The outline of the paper is as follows: Section 7.2 describes the response of the detector to a signal from a black hole binary system. An overview of the Bayesian inference techniques used to estimate the errors in the parameter recovery is given in Section 7.3. Section 7.4 displays and discusses the results. The main results are summarised and future directions are outlined in Section 7.5.

7.2 Gravitational Waves from Supermassive Black Hole Binaries

Assuming circular orbits, the orbital velocity of a black hole binary in the PTA frequency band scales as

$$v \simeq 2.5 \times 10^{-2} \left(\frac{f}{10^{-8} Hz} \right)^{1/3} \left(\frac{M}{10^{8} M_{\odot}} \right)^{1/3}, \tag{7.1}$$

where $M = m_1 + m_2$ is the total mass, f is the gravitational wave frequency, and we are using units where $G = c = 1$. We conclude from this that the orbital dynamics is only mildly relativistic, and that the gravitational wave emission is well described by the lowest order post-Newtonian formulae. Another way of seeing this is to look at the time to merger, which scales as

$$t_c = 2 \times 10^6 \,\text{years} \left(\frac{10^{-8}\,\text{Hz}}{f} \right)^{8/3} \left(\frac{10^8 M_\odot}{\mathcal{M}} \right)^{5/3} . \tag{7.2}$$

Here $\mathcal{M} = (m_1 m_2)^{3/5}/M^{1/5}$ is the chirp mass, which ranges from $0.44M$ for equal mass systems to $0.22M$ for mass ratios of 1:10. These considerations suggest that the gravitational wave signal can be modeled as a simple sinusoid of fixed frequency [94, 95, 93]. Allowing for moderate orbital eccentricity introduces the complication of having to consider multiple sinusoids at harmonics of the orbital period, but the essential picture is unchanged.

A more important effect that was not considered in these earlier studies is the contribution to the signal from gravitational waves disturbing the pulsars. This introduces a new time-scale into the problem in the form of the projected Earth-pulsar distance, $d\,(1 - \cos(\mu))$, where d is the distance to the pulsar and μ is the angle between the line of sight to the pulsar and the line of sight to the black hole binary. This time-scale is typically of order a few thousand years. When the pulsar term is included, the effective baseline grows from tens, to tens of thousands of years (the temporal equivalent of aperture synthesis). The extended baseline makes it possible to measure the frequency change, and hence, the chirp mass. The minimum detectable

rate of frequency change [96]

$$\dot{f}_{\rm min} \simeq \frac{1}{{\rm SNR}\, T^2}\,, \tag{7.3}$$

sets the minimum chirp mass that can be measured:

$$\begin{aligned} \mathcal{M}_{\rm min} &= 5.8\times 10^6 M_\odot \left(\frac{20}{\rm SNR}\right)^{3/5} \times \\ &\left(\frac{10^4\,{\rm years}}{T}\right)^{6/5} \left(\frac{10^{-8}\,{\rm Hz}}{f}\right)^{11/5}\,. \end{aligned} \tag{7.4}$$

With the chirp mass determined, the amplitude of the signal can be used to solve for the distance to the black hole binary. The μ dependence in the effective distance provides additional information about the sky location of the binary, and this, combined with the increased SNR from using the full signal, leads to a significant improvement in the angular resoltuon of the PTA.

The GW signal from a mildly relativistic black hole binary on a circular orbit is characterized by eight parameters: the distance to the BH binary D; the sky location ϕ and $\cos(\theta)$; the angular frequency ω_o of the binary orbit when observations begin at Earth; the orbital inclination $\cos(\iota)$; the orbital phase at the line of nodes θ_n; the orientation of the line of nodes ϕ_n and the chirp mass $\mathcal{M}$. The signal can be written as the sum of two sub-signals [97, 98], which we refer to as the pulsar signal and the Earth signal. The former is due to the disturbance caused by the gravitational wave at the pulsar, the later to the disturbance at the Earth:

$$R(t_e) = r_p(t_p) + r_e(t_e). \tag{7.5}$$

In the plane wave limit, which pertains when $D \gg d$, t_p is given by

$$t_p \approx t_e - d\,(1 - \cos(\mu))\,, \tag{7.6}$$

where t_e is the time at the Earth and μ is the angle between the line of sight to the pulsar and the line of sight to the binary. The two parts of the residuals are explicitly given in [9, 86]:

$$r(t) = \frac{1}{2\,(1+\cos(\mu))}\,(\hat{a}\otimes\hat{a}) : \left(r_+(t)\mathbf{e}^+ + r_\times(t)\mathbf{e}^\times\right)\,. \tag{7.7}$$

Here $\mathbf{e}^{+,\times}$ are the GW polarization tensors, $\hat{a}$ is the unit vector pointing from the Earth to the pulsar, and

$$r_+(t) = \alpha(t)\,(A(t)\cos(2\phi) - B(t)\sin(2\phi)) \tag{7.8}$$

$$r_\times(t) = \alpha(t)\,(A(t)\sin(2\phi) + B(t)\cos(2\phi))\,, \tag{7.9}$$

with

$$A(t) = -\frac{1}{2}\sin\left[2\,(\Theta(t)-\Theta_n)\right]\left[3+\cos(2i)\right] \tag{7.10}$$

$$B(t) = 2\cos\left[2\,(\Theta(t)-\Theta_n)\right]\cos(i). \tag{7.11}$$

The amplitude $\alpha(t)$ can be expressed as:

$$\alpha(t) = \frac{\mathcal{M}^{\frac{5}{3}}}{D\omega(t)^{\frac{1}{3}}}. \tag{7.12}$$

Finally, the orbital frequency and the orbital phase evolve according to

$$\Theta(t) = \Theta_o + \frac{1}{32\mathcal{M}^{\frac{5}{3}}}\left(\omega_o^{-\frac{5}{3}} - \omega(t)^{-\frac{5}{3}}\right) \tag{7.13}$$

$$\omega(t) = \left(\omega_o^{-\frac{8}{3}} - \frac{256}{5}M_c^{\frac{5}{3}}t\right)^{-\frac{3}{8}}\,. \tag{7.14}$$

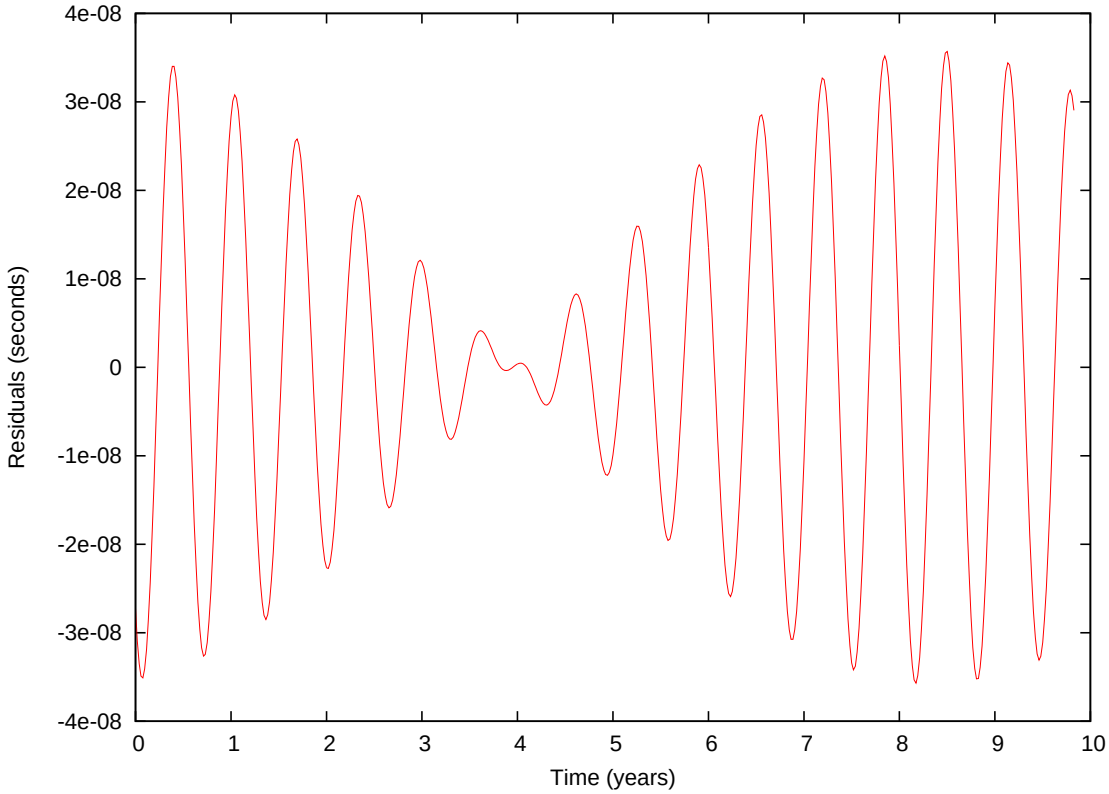

Figure 7.1: Residuals for a MBHB with chirp mass $\mathcal{M} = \sqrt{2} \times 10^8 M_\odot$, frequency of the gravitational perturbation at Earth $f = 5.0736 \times 10^{-8}$ Hz and frequency of the gravitational perturbation at the pulsar $f = 4.7145 \times 10^{-8}$ Hz

Unless the angle μ is very small, the signal at the pulsar will have a measurably different frequency compared to the signal at Earth, since the binary system will have evolved in the elapsed time $\Delta t = d(1 - \cos(\mu))$ (Note: this quantity can be positive or negative depending on who "sees" the signal first). Figure 7.2 shows an example of the noise free timing residuals obtained from a MBHB system with $\mathcal{M} = \sqrt{2} \times 10^8 M_\odot$. The orbital frequency of the system when it emits the perturbation that reaches the earth at the beginning of the measurement is 2.5368×10^{-8} Hz. The distance of the

binary from earth is $1.77\,Mpc$. Its sky location is given by $\phi = 0.3$ and $\theta = 1.42$. Its orbital inclination is $\pi/2$, the orbital phase and orientation of the line of nodes are both $\pi/3$. The superposition of the two signals is apparent from the beat envelope. It is possible to recover all the parameters characterizing the MBHB from the timing residuals seen in a PTA, so long as the pulsar contributions to the signal are used.

At first sight it may seem impossible to include the pulsar terms in a coherent analysis. To have phase errors in the pulsar terms less than $\Delta\Theta$ radians requires that we know the distance to each pulsar to order $\Delta d \sim \Delta\Theta/f$. Setting $\Delta\Theta = 0.1$ and $f = 10^{-8}$Hz gives $\Delta d \sim 0.1$ parsecs, or a fractional error of $\Delta d/d \sim 0.01\%$. This is far smaller than the accuracy that is currently available from electromagnetic observations. Techniques such as parallax measurements and astrometry achieved a precision of about 10%. Recently [69] have been able to estimate the distance to a specific pulsar with 1% error using the kinematic distance derived from pulsar timing data. This accuracy is not typical, and the method is only valid for nearby pulsars. But it turns out that highly accurate pulsar distance estimates are not required if we include the distance to each pulsar, d_i, as model parameters to be solved for from the GW data. The technique works as follows: for any one pulsar the phase matching of the pulsar terms produces a series of secondary maxima in d_i corresponding to 2π increments in the accumulated phase. As the estimate for d_i moves further away from the correct solution along this line of secondary maxima the predicted GW frequency and amplitude of the pulsar term starts to deviate from the true value, and the height

of the secondary maxima drop. In other words, it is the overall frequency/amplitude envelope that fixes the distance to the pulsar, and not the phase matching. Indeed, we will see that the secondary maxima are so close together that the individual peaks in the posterior distribution for d_i blend together into a continuum. The blending is even more pronounced in the marginalized posterior distributions for d_i where the correlations between d_i and μ are integrated out. We will see that it is possible to use the GW data to provide estimates for the pulsar distances, while simultaneously deriving useful estimates for the chirp mass and black hole location.

The common challenge with all GW detectors is to isolate a signal which is relatively weak compared to the noise surrounding it. The noise is composed of instrumentation or measurement noise and the background confusion noise generated by the superposition of all the unresolved MBHBs signals [75, 99, 77, 66, 35, 100]. The measurement noise is simulated as a white noise with a standard deviation of $\sigma = 100\,ns$ for all pulsars. An array of 20 pulsars each with a timing rms of about $100\,ns$ is a reasonable estimate of what will be achieved by PTAs in the near future [101, 70]. It is also thought to be close to the threshold for the detection of the diffuse background [66]. Models for the background [100, 94] suggest that its power spectral density can be described as:

$$S_{bg}(f) = \frac{3H_o^2}{16\pi}\frac{h_o^2}{\rho_c} f_0^{\frac{4}{3}} f^{-\frac{7}{3}} \left(1 + \frac{f}{f_o}\right)^{2\gamma}, \tag{7.15}$$

where h_o, f_o and γ are model dependent. This result differs significantly from earlier studies (e.g. [99]) which predicted a $f^{-\frac{7}{3}}$ power-law. In figure 7.2, we compare the

power spectral density of the signal generated by the MBHB described above with white instrument noise and four different models of background noise (e.g. VHM, VHMhopk, KBD, BVRhf, for a description of these models see [102, 103, 104, 105, 106]).

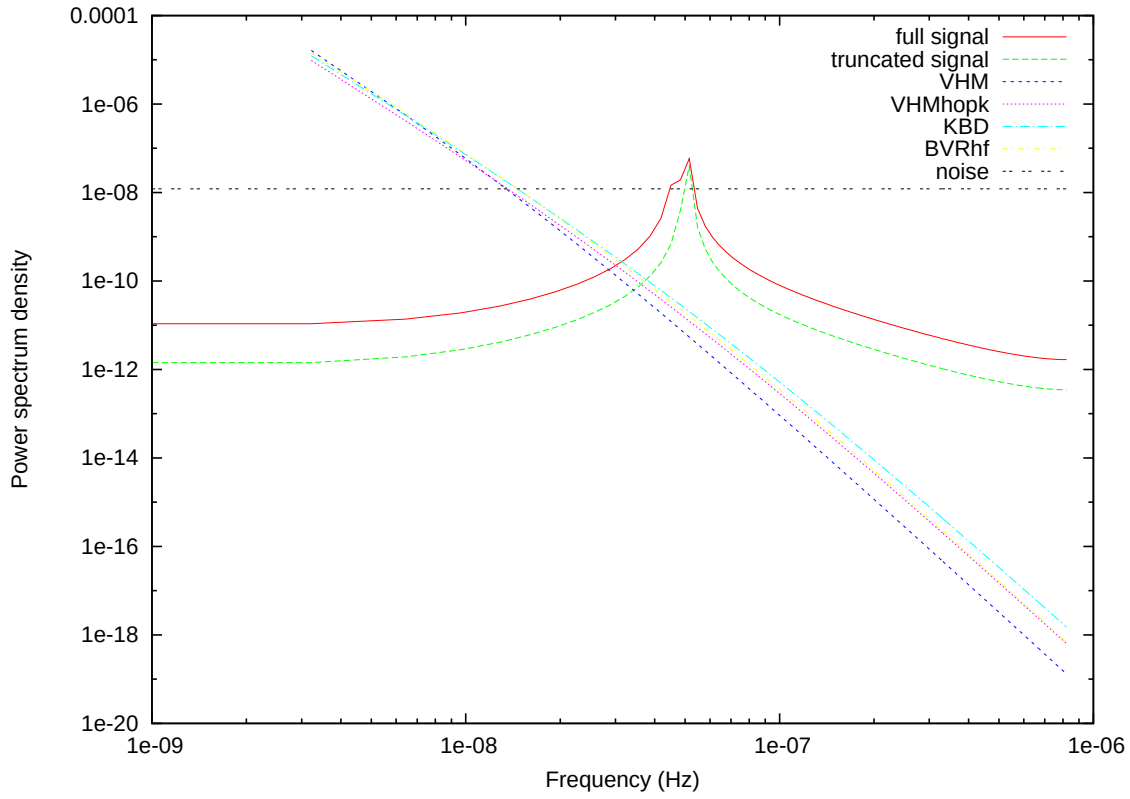

Figure 7.2: Power spectral density of the full (solid line) and truncated (dashed line) signal from a binary compared with the power spectral density of the instrument white noise and four models of background noise (VHM, VHMhopk, KBD, BVRhf). The spectral density described here is found from the residuals issued from the timing of one pulsar in an array of 20 pulsars. The cumulative SNR (over the full array) is 20 for the full signal and 14 for the truncated signal

The square of the signal to noise ratio doubles when using the full signal compared to the truncated signal, which signifies that including the distances to the pulsars in

the parameter space could contribute to the detection of more sources. For most of the frequency window of interest, the background noise is much smaller than both the signal and the white noise [75, 66, 35]. For the sake of simplicity, we will ignore it, as it will not greatly affect the estimation of the parameters for a detected source. One would need to include it however in order to determine the number of detectable sources, which will be studied in a future paper.

7.3 Bayesian Inference and Parameter Estimation

To determine how well we can estimate the parameters of a MBHB from noisey pulsar timing data we need to compute the posterior distribution for the model parameters. The posterior distribution $p(\vec{x}|s)$ gives the probability of observing parameters $\vec{x}$ given data s. It is defined by

$$p(\vec{x}|s) = \frac{p(s|\vec{x})p(\vec{x})}{\int d\vec{x}\, p(s|\vec{x})p(\vec{x})\mathrm{d}\vec{x}}. \tag{7.16}$$

Here $p(\vec{x})$ is the prior distribution, which is the mathematical representation of the prior knowledge of the system, and $p(s|\vec{x})$ is the likelihood evaluated at $\vec{x}$. It is the probability that a system with parameter $\vec{x}$ will yield a signal s in the detector.

To generate the posterior distribution, a Markov Chain Monte Carlo (MCMC) algorithm [107, 108, 109, 91] is used to explore the parameter space. The MCMC consists of proposing "jumps" from one location $\vec{x}_i$ in the parameter space to another $\vec{x}_{i+1}$. The jumps have a finite probability $\kappa(\vec{x}_{i+1}|\vec{x}_i)$ of being accepted that is given

by the Hasting ratio:

$$\kappa(\vec{x}_{i+1}|\vec{x}_i) = \min(1, H) \tag{7.17}$$

where

$$H = \frac{p(\vec{x}_{i+1})p(s|\vec{x}_{i+1})q(\vec{x}_i|\vec{x}_{i+1})}{p(\vec{x}_i)p(s|\vec{x}_i)q(\vec{x}_{i+1}|\vec{x}_i)}. \tag{7.18}$$

Here $q(\vec{y}|\vec{x})$ is the proposal distribution: the probability that a jump from $\vec{x}$ to $\vec{y}$ will be proposed. For a more detailed description of MCMC techniques see [110].

7.3.1 Prior distribution

Some information is known prior to the analysis. For instance, there is a higher probability the source will be located far from the Earth, as the area of a sphere increases as the square of its radius. To account for this, the prior distribution on D is chosen to be proportional to D^2 out to some large distance $D_{\max}$ that is well outside the horizon for PTA detections. The sources are assumed to be uniformly distributed on the sky, with random orientations. A more informative prior on the distance and sky location could be built using galaxy catalogs. For the distances to the N pulsars, the prior follows from electromagnetic observations, which we take to be a collection of Gaussians centered around the measured value d_i^{EM} with a standard deviation $\sigma_i = \alpha d_i^{EM}$:

$$p(d_i) \propto \prod_{i=1}^{N} e^{-\frac{\left(d_i^{EM} - d_i\right)^2}{2{\sigma_i}^2}}, \tag{7.19}$$

where d_i is the proposed distance to the pulsar i. For our simulated PTA we draw d from the range $0.5 - 1.5\,\mathrm{kpc}$, and include errors in the estimated d^{EM} that are con-

sistent with our choice of prior. We will consider some examples where the fractional distanced error $\alpha = 0.1$ for all the pulsars, and other examples where α takes different values for different pulars. We will focus on arrays with $N = 20$ pulsars.

7.3.2 Likelihood

The likelihood $p(s|\vec{x})$ is by definition the probability of observing a signal s from a source with parameters $\vec{x}$. For Gaussian noise it is given by:

$$p(s|\vec{x}) = C \exp\left[-\frac{1}{2}\left((s - R(\vec{x})) \,|\, (s - R(\vec{x}))\right)\right], \tag{7.20}$$

where C is a normalization constant, $R(\vec{x})$ is the waveform described in Section 7.2 for a set of parameters $\vec{x}$, and the noise weighted inner product is defined as:

$$(a|b) = 2\int_0^\infty \left(\tilde{a}_i^*(f)\tilde{b}_j(f) + \tilde{a}_i(f)\tilde{b}_j^*(f)\right) S_{nij}^{-1}(f)df. \tag{7.21}$$

A summation over the indexes i and j from 1 to N is implied. $S_{nij}(f)$ is the spectral density of the noise correlation matrix $C_{ij}(\tau) = \int n_i(t)n_j(t+\tau)dt$ where $n_i(t)$ is the noise in the signal from pulsar i. S_{nij} is not typically diagonal since the background noise is correlated between the pulsars. However the instrument noise is uncorrelated. Since we ignore the background noise, S_{nij} becomes diagonal.

7.3.3 Proposal Distribution

A combination of six proposal distributions $q(\vec{y}|\vec{x})$ is used. The first makes use of the Fisher Information Matrix approximation to the posterior distribution. The Fisher matrix indicates the level of correlation between the parameters, and the diagonal elements of its inverse give a rough approximation of the error expected in

the estimation of each parameter. The Fisher matrix is the expectation value of the negative Hessian of the log posterior evaluated at the posterior mode:

$$\Gamma_{ij} = -\langle \partial_i \partial_j \log\, p\,(\vec{x}|s) \rangle = (\partial_i R | \partial_j R) - \partial_i \partial_j \log\, p\,(\vec{x}) \tag{7.22}$$

In the current setting the prior only contributes to the diagonal elements of the Fisher matrix, adding a term $1/\sigma_i^2$ to the elements representing the pulsars distances. The eigenvectors of the Fisher matrix define a new set of uncorrelated parameters. The eigenvalues indicate the curvature of the likelihood surface along each eigenvector. When the curvature is high, the likelihood changes a lot for a small variation of the "eigen-parameter", and a big jump is unlikely to get accepted. To effectively explore the likelihood surface, jumps along those eigenvectors are proposed, which are scaled by their eigenvalues. The second proposal distribution is similar, but with a bigger scaling. Since the jumps are bigger they are less likely to be accepted, but when accepted they explore the parameter space faster. The third proposal consists of drawing a new parameter set from the prior distributions. The fourth proposal pick selects one of the pulsars and draws a new pulsar distance from the prior distribution. The fifth proposal distribution is similar to the fourth, but uses a proposal centered around the true value. It prevents the MCMC from searching exclusively around the values predicted by the prior. Finally, tiny jumps are sometimes proposed along each parameter. These tiny jumps are very likely to be accepted, and this helps prevent the chain from getting stuck in a location where the Fisher matrix estimates are particularly poor approximations to the posterior distribution.

7.3.4 Parallel tempering

A parallel tempering scheme [111] is implemented to improve mixing and convergence of the Markov Chains. It consists of running a number of chains in parallel, each of them with a "temperature" $T = 1/\beta$ which modifies the likelihood:

$$p_\beta(s|\vec{x}, \beta) = p(s|\vec{x})^\beta. \tag{7.23}$$

The temperature effectively "smooths" the likelihood map. The higher the temperature, the more likely a jump is going to be accepted. The chains then communicate by swapping with each other. The swaps have a probability of being accepted given by a Hasting ratio:

$$H = \frac{p(s|\vec{x}_i, \beta_j)p(s|\vec{x}_j, \beta_i)}{p(s|\vec{x}_i, \beta_i)p(s|\vec{x}_j, \beta_j)}\,. \tag{7.24}$$

The indicies i and j refer to the individual chains. Here 10 chains are used, with temperatures exponentially spaced between $T = 1$ and $T = 10$.

7.4 Results

The addition of the pulsar distances to the parameter space allows us to use the pulsar signals in the analysis. It follows that information about the evolution of the orbital frequency over a long period of time and the relative phases between the Earth signal and the pulsar signals can be extracted. This information is enough to independently determine the distance to the binary and the chirp mass.

We use a simulated PTA comprised of $N = 20$ randomly chosen pulsars drawn uniformly in sky location and with distances in the range $0.5-1.5\,\mathrm{kpc}$. The parameters

describing the array are listed in Table 7.1. With 20 uniformly distributed pulsars the array has a fairly uniform antenna pattern. Increasing the size of the array to 40 pulsars would further improve the sky coverage, but the effect is not very significant. To investigate these effects we studied the spread in SNR across the sky for a particular source, by considering 3072 different sky locations using 50 randomly drawn arrays of pulsars. In each case the SNR corresponding to the sky location was calculated, and normalized by the average SNR to produce the histograms seen in Figure 7.3. The variation in SNR across the sky is smaller for the larger PTA, but not by a significant amount. In either case, we do no expect to see a significant correlation between the sky location and black hole distance parameters, and this expectation is borne out in our analysis. The distance and sky location of the 20 pulsars used in our analysis are listed in Table 7.1.

The distance to the binary is only present in the amplitude of the signal. It makes its determination very dependent on the inclination angle ι. For values of the inclination angle close to 0 or π, the determination of the distance to the black hole binary system is very poor. At $\iota = 0$ and $\iota = \pi$, the Fisher matrix becomes singular. Figure 7.4 displays the error in the distance to the binary predicted by the Fisher information matrix as a function of the inclination.

For an ideal value of $\pi/2$ for the inclination and a SNR of 20, our MCMC predicted an error of $\sim 7\%$ in the distance estimation, which is in agreement with the Fisher prediction. The error on the chirp mass was $\sim 2\%$. The orbital frequency was

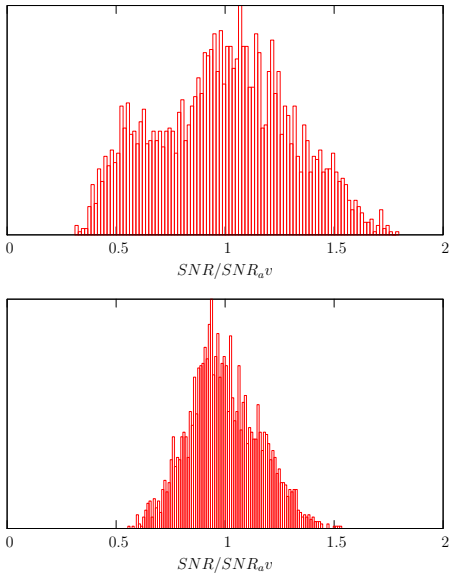

Figure 7.3: SNR spread across the sky for arrays of 20 pulsars (top panel) and 40 pulsars (bottom panel)

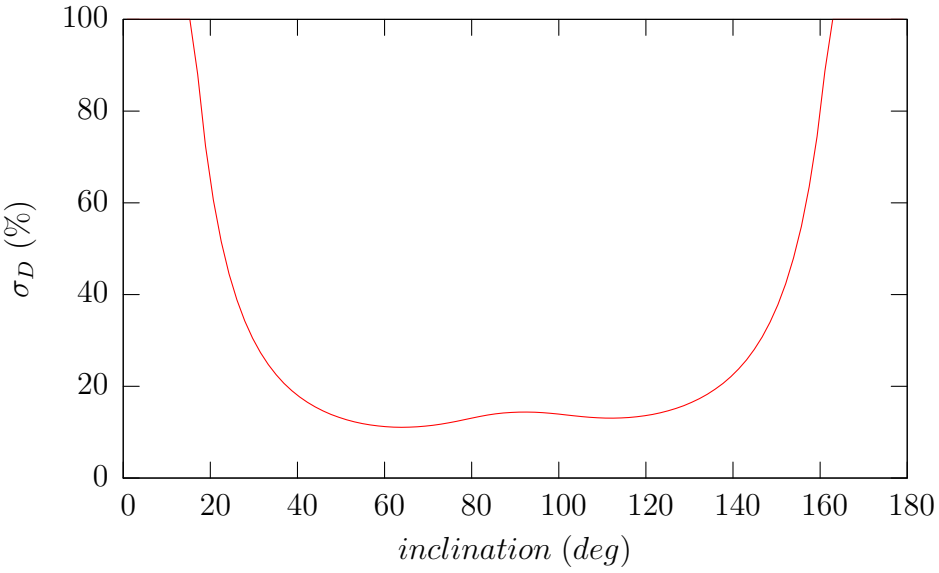

Figure 7.4: Error in the determination of the distance to the binary σ_D as a function of the inclination. The error is estimated using the Fisher information matrix.

Table 7.1: The positions and distances for the 20 pulsars that define the array used in the analysis. Here d is the true distance to the pulsar, while d_{EM} is the prior estimate of the distance from traditional astronomical methods.

	$d\,(kpc)$	$d_{EM}\,(kpc)$	ϕ	$\cos\,\theta$
pulsar 1	0.987	1.010	1.17	−0.27
pulsar 2	1.391	1.371	5.49	0.95
pulsar 3	1.008	1.299	6.28	−0.25
pulsar 4	1.128	1.057	5.21	−0.99
pulsar 5	1.075	1.111	5.87	0.63
pulsar 6	0.651	0.629	5.23	−0.48
pulsar 7	0.957	0.895	0.02	0.67
pulsar 8	1.138	0.955	5.13	−0.37
pulsar 9	1.133	0.995	3.24	0.10
pulsar 10	0.516	0.771	5.23	−0.72
pulsar 11	1.184	1.084	4.53	0.09
pulsar 12	1.674	1.491	5.85	−0.52
pulsar 13	1.455	1.437	3.57	0.48
pulsar 14	0.544	0.507	2.83	−0.70
pulsar 15	0.897	0.925	0.34	−0.28
pulsar 16	0.756	0.688	4.71	−0.98
pulsar 17	1.318	1.331	6.21	0.09
pulsar 18	0.882	0.920	1.46	0.14
pulsar 19	0.676	0.641	0.23	−0.64
pulsar 20	0.852	0.757	5.60	0.09

extremely well determined ($\sim 0.3\%$). Figure 7.4 shows the marginalized posterior distribution for the black hole distance and the chirp mass for three binaries with different chirp masses, $10^8 M_\odot$,$5 \times 10^8 M_\odot$ and $10^9 M_\odot$ respectively (Sources 1, 2 and 3 in Table 7.2). The marginalized posterior distributions are represented by the boxed histograms while the smooth line represents the Fisher matrix estimates. The distances were chosen in order to ensure a SNR of 20 for each case. The heaviest source is sufficiently relativistic that we should have included higher order post-Newtonian terms in the waveform model, but we defer this analysis to a future study.

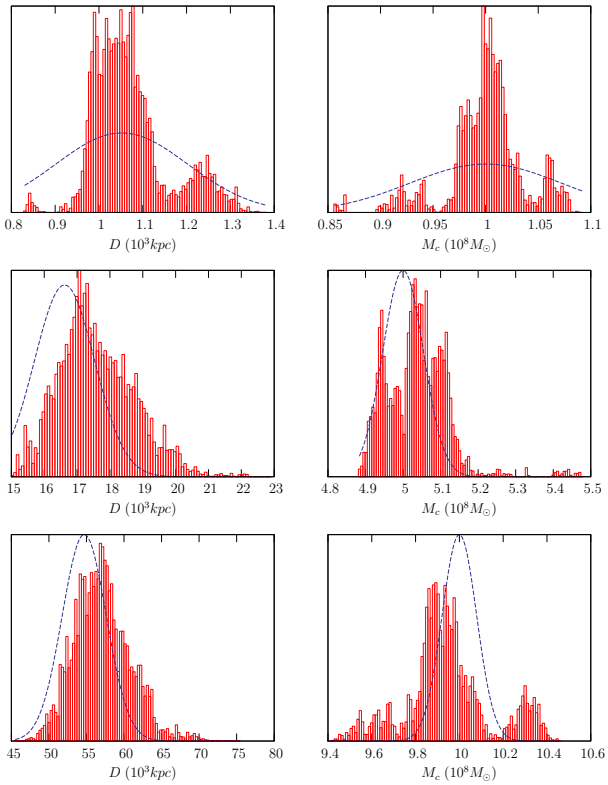

Figure 7.5: Posterior distributions of D and $\mathcal{M}$ with $\iota = \pi/2$ for three binaries with different chirp mass: $10^8 M_\odot$ (first row), $5 \times 10^8 M_\odot$ (second row), $10^9 M_\odot$ (third row). The distances to the three binaries are normalised so that the three SNRs are equal to 20. The MCMC derived posterior distributions (histograms) are compared to the Fisher matrix estimates (dashed curves).

The Fisher information matrix is seen to provide a good approximation to the posterior distribution for the black hole parameters. The differences can in part be attributed to imperfect convergence in the MCMC runs, which suffer from the high dimensionality of the parameter space and strong correlations between many of the model parameters. In some cases the posterior distribution peaks are shifted from their injected values. This is caused by the priors for the distances to the pulsars, which are not always peaked close to their true values, as we will show below.

Unfortunately, most black hole binaries will not have an inclination of $\iota = \pi/2$. For a more realistic error prediction, we perform the same analysis for similar binaries whose inclinations are this time chosen to be $\pi/4$. We otherwise use the same sets of parameters (Sources 4, 5 and 6 in Table 7.2). The distances D change slightly in order to conserve an SNR of 20. The results are given in figure 7.4.

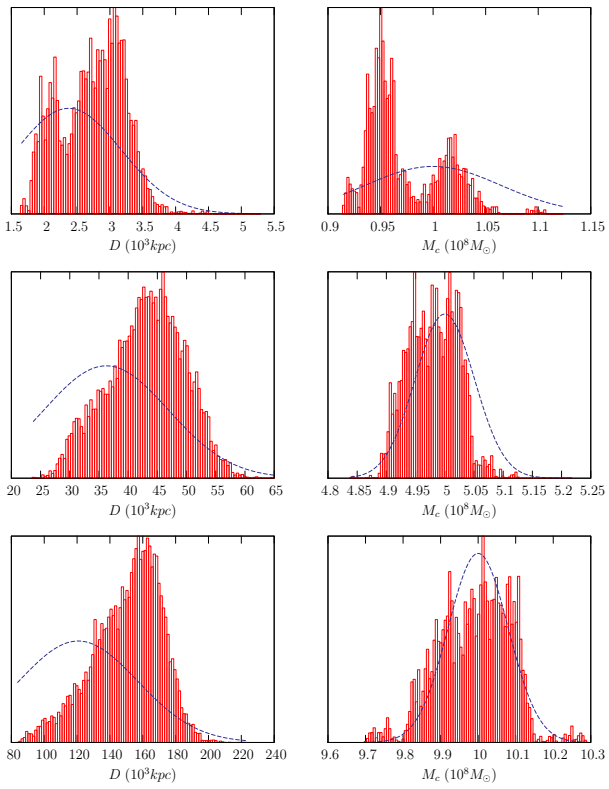

Figure 7.6: Posterior distributions of D and $\mathcal{M}$ with $\iota = \pi/4$ for three binaries with different chirp mass: $10^8 M_\odot$ (first row), $5 \times 10^8 M_\odot$ (second row), $10^9 M_\odot$ (third row). The distances to the three binaries are normalised so that the three SNRs are equal to 20. The MCMC derived posterior distributions (histograms) are compared to the Fisher matrix estimates (dashed curves).

The error for the distance D is predictably bigger. It rises from less than 10% to about 15%. The Fisher matrix estimates the error to be as large as 30%. Again one

has to take into consideration the Fisher matrix gives only a rough approximation to the posterior distribution. The posterior distributions obtained for the three different binaries are consistent, which indicates the MCMCs have reasonably converged. The measurements of the frequency and chirp mass were not significantly affected by the change in inclination, which confirms they are weakly correlated.

Table 7.2: The parameters for the 6 black hole binary examples we are considering. The merger times t_c can be computed from these parameters: Sources 1,4 $t_c = 4.39 \times 10^4$ years; Sources 2,5 $t_c = 3.0 \times 10^3$ years; Sources 3,6 $t_c = 9.46 \times 10^2$ years.

Source	$D\,(10^3\,kpc)$	$\mathcal{M}\,(10^8\,M_\odot)$	$\omega_o\,(10^{-7}\,s^{-1})$	$i\,(rad)$	$\phi\,(rad)$	$\cos\theta$	$\theta_n\,(rad)$	$\phi_n\,(rad)$
1	1.05	1.0	1.328	$\pi/2$	3.98	−0.83070	1.05	6.08
2	16.6	5.0	1.328	$\pi/2$	3.98	−0.83070	1.05	6.08
3	54.7	10	1.328	$\pi/2$	3.98	−0.83070	1.05	6.08
4	2.37	1.0	1.328	$\pi/4$	3.98	−0.83070	1.05	6.08
5	36.2	5.0	1.328	$\pi/4$	3.98	−0.83070	1.05	6.08
6	121	10	1.328	$\pi/4$	3.98	−0.83070	1.05	6.08

In addition to the decoupling of the binary distance and chirp mass from the amplitude, the addition of the pulsar terms increase considerably the precision of the determination of the binary position. The pulsar terms are evaluated at t_p, which is the time at which the disturbance from the gravitational wave occurred. It is given by $t_p = t - d(1 - \cos(\mu))$, where μ is the angle between the line of sight to the pulsar and the line of sight to the binary. It is therefore a function of the position of the binary. The pulsar signals give previously non-existent information on the chirp mass and distances to the pulsars, but also help refine the measurement of the binary sky location. To illustrate this, figure 7.7 compare the posterior distribution with the Fisher estimation for the two position parameters, for a case in which the full signal was used and a case in which the signal from the disturbance at the pulsar was

omitted. When the pulsar signals are added, the SNR naturally increases. Here the distance to the binary was normalized each time to get a SNR of 20 for both cases. The effect from the information encoded in the new term in the signal can then be dissociated from the effect due to the increase in the SNR. A mid-range chirp mass and frequency were used ($\mathcal{M} = 5 \times 10^8 M_\odot$ and $\omega_o = 2\pi/1.5\,\text{years}$), and an inclination of $\iota = \pi/4$.

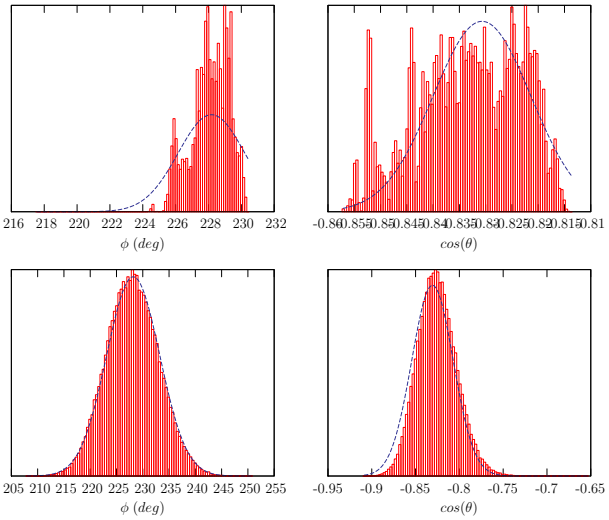

Figure 7.7: Position error for full (upper panel) and truncated signal (lower panel).

To compare our results to [95], we calculate the pulsar timing array angular resolution given by

$$\Delta\Omega = 2\pi\sqrt{(\Delta\cos\theta\Delta\phi)^2 - (C^{\phi\cos\theta})^2}, \tag{7.25}$$

where $C^{\phi\,\cos\theta}$ is a off-diagonal term of the covariance matrix (the inverse of the Fisher information matrix). For the errors in the individual sky location parameters we use the Fisher matrix estimates, which are in very good agreement with the posterior

distributions. For the truncated signal we find $\Delta\Omega = 41.3\,\mathrm{deg}^2$, which is consistent with [95], while the full signal yields $\Delta\Omega = 6.5\,\mathrm{deg}^2$. The measurement is therefore improved by a factor of 6.4. Accounting for the increase in the SNR when the pulsar terms is added to the truncated signal, the angular resolution goes from $\Delta\Omega = 6.5\,\mathrm{deg}^2$ to $\Delta\Omega = 5.8\,\mathrm{deg}^2$. This is a considerable improvement (by about an order of magnitude), which highlights the importance of utilizing the full signal.

It was previously mentioned that the full signal also gives information about the distance to the pulsars. In the situations described above we assumed a 10% error in each of the pulsar distances, which correspond to the high end of today's accuracy in measurements using parallax and other methods. We expect the pulsar distances to be further constrained by the gravitational wave analysis. The Fisher information matrix predicts that for most pulsars, the error in the distance measurement will be constrained to a few percent. The level of improvement depends on the location of the pulsar with respect to the line of sight to the binary. If the Earth , pulsar and binary are aligned, then $t_p = t$, and no new information is given by the pulsar term in the signal. Figure 7.8 compares the Fisher matrix estimates to the MCMC derived posterior distribution and to the prior distribution, for a few relevant pulsars:

A few things are clear at first sight. First, when the pulsar's sky location is close to the line of sight to the binary ($\cos\mu \approx \pm 1$), the prior is recovered from the posterior distribution, which means that no new information was acquired from the gravitational wave signal, as expected. Then, for the pulsars that are not close to

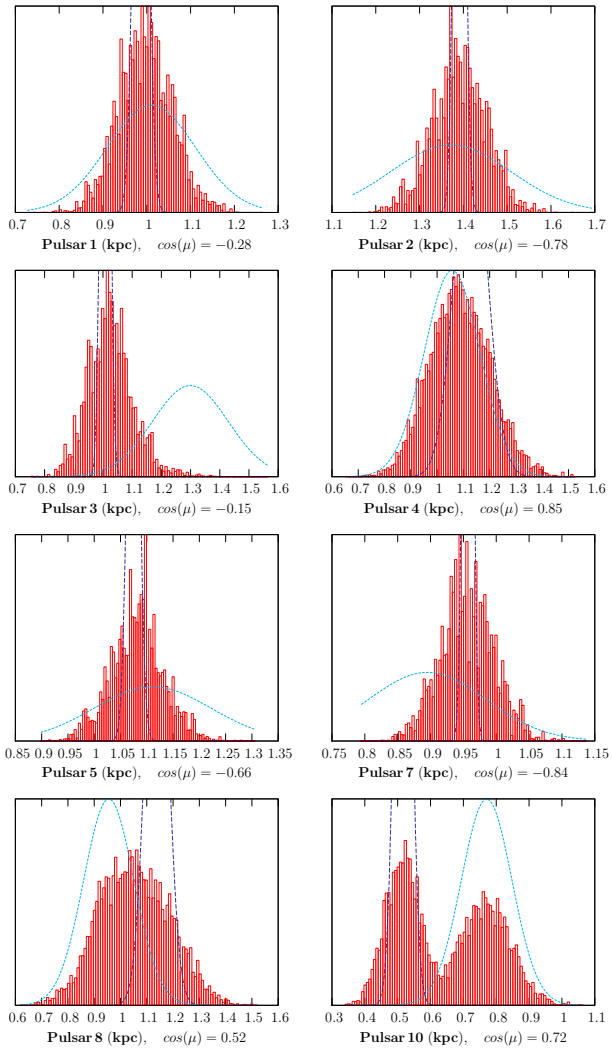

Figure 7.8: Marginalized posterior distributions for the distances to 8 of the 20 pulsars in the array (histograms) compared to the prior distributions (dotted curves) and the Fisher matrix estimates (dashed curves). The priors have a standard deviation of 10%, which correspond to the confidence in the measurement from electromagnetic astronomy. For some of the pulsars, the study of the gravitational wave signal slightly improves the distance determination.

the line of sight, the peak of the posterior distribution can be shifted from the true value of the distance. This occurs when the true value (value at which the gaussian extracted from the Fisher information matrix is centered) is located a few sigmas away

from the prior-predicted value. As mentioned earlier, these shifts will induce a shift in the posterior distribution of the binary distance, chirp mass and orbital frequency with respect to their true values. As a sanity test, the priors were centred to the right values for all the pulsars' distance. As anticipated, the posterior distribution for the binary parameters are in this case centered on their right values as well. Finally, and maybe most importantly, the posterior distribution from the MCMC is consistently much broader than the error predicted by the Fisher information matrix. For most pulsars, the posterior distribution is as wide as the prior, which means that only limited information concerning the distances could be extracted from the gravitational wave signal. To explain the discrepancy, the pulsar term of the residuals is rewritten as:

$$r_p(t) = \frac{\mathcal{M}^{\frac{5}{3}}}{D\omega^{\frac{1}{3}}(t_p)} \cos\left(\omega(t_p)t_p + \Phi\right), \tag{7.26}$$

with $t_p = t - d(1 - \cos\mu)$. If one varies the distance to the pulsar d such that

$$\omega(t'_p)t'_p = \omega(t_p)t_p + 2\pi, \tag{7.27}$$

then only the amplitude and frequency are slightly changed. This results in a series of secondary maxima in the likelihood, which for this particular pulsar are spaced by $\Delta d \sim 0.017\,\mathrm{kpc}$, which correspond to 1.7% of the distance. The change in frequency and amplitude between adjacent maxima is small compared to the measurement uncertainity in these quantities, and it is not until multiple secondary maxima have been traversed that the likelihood drops significantly. The separation of the secondary maxima is comparable to the Fisher matrix prediction for the error in d, which means

that where the Fisher matrix predicts the posterior distribution to drop, the MCMC will find another maximum, almost as good as the primary. The error in the detection of each local maximum blends with the error in the detection of its neighbor. They form an "error envelop" which is limited in its width by the change in the frequency and amplitude of the pulsar signal. Even though the gain in the precision of the measurement of the distances to the pulsars is not as significant as predicted by the Fisher matrix analysis, it is still noticeable for a few pulsars.

To explore the limitation of the determination of the distances due to the periodicity of the residuals, we set the priors for five pulsars to be Gaussians with standard deviations randomly drawn from the range $\alpha = [0.005, 0.03]$. For ten pulsars, the standard deviation is drawn from the interval $\alpha = [0.09, 0.15]$, and for the remaining five pulsars, the prior is chosen to be less constraining, $\alpha = [0.20, 0.25]$. Table 7.3 lists the estimated distances to the pulsars d^i_{EM}, their true distances d^i, and the estimated error in the existing measurement represented by the standard deviation of the prior distribution $\sigma_{\rm prior}$.

After analysis of the signal using the parallel tempering MCMC, the estimation of the distance is this time improved significantly for some of the pulsars (#'s 7, 17, 18, 19, 20). The measurement is particularly improved for pulsars with a less constraining prior, as long as their line of sight is not too close to the line of sight to the black hole ($\cos\,\mu \sim 1$). When the prior distance is far away from the real value, the MCMC detect the discrepancy, and the posterior distribution is double peaked (pulsar 10),

Table 7.3: The table lists the distances of the 20 pulsars forming the array used in the analysis as well as the confidence level of their prior. d is the real distance to the pulsar, while d_{EM} is the prior estimation of the distance by traditional astronomical method (e.g.: parallax, astrometry). σ_{prior} is the estimated error in the measurement of the prior (in percent with respect to d_{EM})

Pulsar	$d\,(kpc)$	$d_{EM}\,(kpc)$	σ_{prior}
1	1.009	1.010	0.53
2	1.374	1.371	1.22
3	1.242	1.299	1.96
4	1.070	1.057	1.75
5	1.109	1.111	0.52
6	0.655	0.629	11.7
7	0.965	0.895	11.2
8	1.139	0.955	10.0
9	1.135	0.995	10.1
10	0.494	0.771	10.9
11	1.184	1.084	10.0
12	1.700	1.491	11.4
13	1.455	1.437	10.0
14	0.547	0.507	10.8
15	0.895	0.925	10.6
16	0.827	0.688	20.4
17	1.301	1.331	23.3
18	0.841	0.920	20.6
19	0.725	0.641	24.1
20	0.935	0.757	18.8

indicating that the distance was priorly poorly estimated. The posterior distribution of pulsar 7 is identical whether the five first pulsars have a tight prior or not. This seems to indicate that the improvement on the determination of the distances is still limited by the periodicity of the strength of the residuals with respect to the pulsars distances. For this reason, the posterior distribution remains broader than the Fisher estimation. Figure 7.9 display the posterior distribution for the distances to a few relevant pulsars against the Fisher estimations and the priors.

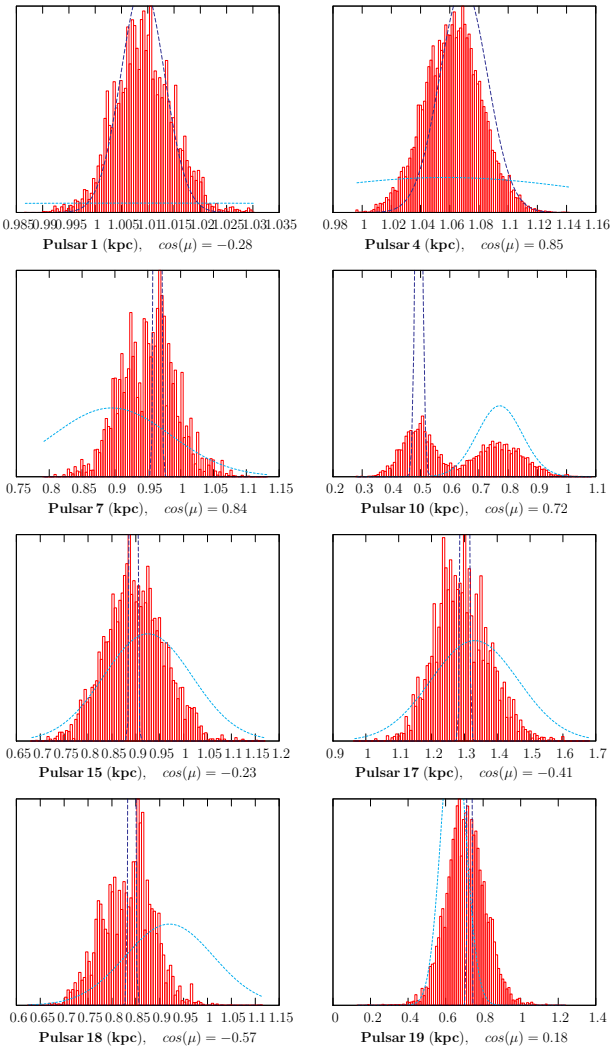

Figure 7.9: Marginalized posterior distributions (histograms) for the distances to 8 of the 20 pulsars in the array compared to the prior distributions (dotted curves) and the Fisher matrix estimates (dashed curves). Pulsars $1 \rightarrow 5$ were assumed to have distances that were well determined by electromagnetic observations. As a consequence, the measurement of the distances to the some of the remaining pulsars can be significantly improved by folding in the gravitational wave analysis of the timing residuals.

The errors on the binary parameters $(D, \mathcal{M}, \omega, \phi, \cos\theta)$ were not significantly affected by the change in the pulsars priors.

7.5 Conclusion

This chapter presented a novel method of analyzing the signals obtained from the timing of an array of pulsars. It consists of considering the distances to the pulsars to be unknown parameters constrained by a prior distributions obtained from existing measurements. This allows to fully take advantage of every part of the signal generated by the gravitational signature of a massive black hole binary, and therefore to optimize the estimation of its parameter and possibly allow for the detection of weaker sources. Unlike previous studies found in the literature [90, 95], we find the gain from this approach to be significant. In particular, we can place a constraint on the distance to the binary ($< 20\%$) as well as a strong one on its chirp mass ($< 5\%$), parameters which have been previously considered as indistinguishable in the Newtonian limit. In addition, one is able to refine the measurements of the distances to the pulsars. The refinement becomes significant for pulsars whose distances are originally poorly estimated. It also follows that the more MBHBs detected, the more trustworthy the estimations for the distances to the pulsars are, which in turns allow for stronger constraints on the MBHBs detected. The biggest contribution of the pulsar signals, however, was to the localization of the source in the sky. To use the full signal can reduce the angular window by an order of magnitude. One could also repeat the study for a more general case of MBHB. For example it would be straight forward to add an eccentricity to the binary's orbit. The parameter space would then acquire two extra dimensions: the eccentricity and the phase of periastron. In

a future paper, we will use our parallel tempering MCMC search to give a precise estimation of the optimal number of sources one can hope to extract from different models of astrophysical background.

CHAPTER 8

CONCLUSION

This thesis covered two aspects of the use of gravitational waves to study cosmology. The first aspect concerns the direct observation of signal from inflation. It was found in chapter 4 that using the Big Bang Observer, whose primary goal is to detect and study the cosmic gravitational background and would be designed to efficiently do so, a background with an energy density as low as $\Omega_{gw} = 2.2 \times 10^{-17}(5\mathrm{yr}/T)^{1/2}(70\,\mathrm{km\,s^{-1}\,Mpc^{-1}}/H_0)^2$ could be detected. To achieve this result, the six spaceships forming the primary constellation of the BBO (figure 2.6) were used to create pairs of fully noise independent interferometers. It was also concluded that the relative orientation of these interferometers did not affect the optimal sensitivity achieved. The second is the characterisation of massive black hole binary systems through the study of their gravitational radiation using pulsar timing arrays. The novel approach introduced in chapter 7, in which the distances to the pulsars in the array are set as parameters in the analysis, improve significantly the estimation of the black hole parameters. The sky location can be determined with a precision an order of magnitude better than previous studies. The chirp mass of the system can also be determined independently of the distance to the binary with a error of about 5% for slow evolving orbits, for which the post-Newtonian terms are negligible. It was roughly estimated that for a mid-range frequency ($1.5\times10^{-8}\,hertz$), a chirp mass of the order $10^6 M_\odot$ would be sufficient to separate it from the distance

to the black holes. As a comparison, if the distances to the pulsars were not included in the parameter space, an unlikely big chirp mass ($10^9 M_\odot$) would be necessary to achieve similar results. The sensitivity of the detector is also increased, since the full signal is now used instead of being truncated. The square of the signal to noise typically doubles, allowing the detection of fainter sources.

This novel approach to the study of massive black hole binaries with pulsar timing arrays opens new directions for future research. For example, it would be interesting to know how many binaries pulsar timing arrays could hope to detect. To do so, population of binaries could be simulated using different population models, and using a Markov Chain Monte Carlo, the parameter space could be spanned in search of bright enough sources. Since the different population models are related to the different cosmology models, this study would ultimately contribute to placing constraints on existing theories.

REFERENCES CITED

[1] Jeff Crowder and Neil J. Cornish. Beyond LISA: Exploring future gravitational wave missions. *Phys. Rev.*, D72:083005, 2005.

[2] Bernard F. Schutz. *A first course in general relativity.* Cambridge University Press, 1985.

[3] Michele Maggiore. Gravitational Waves. Vol. 1: Theory and Experiments. Oxford University Press, October 2007. 572p. (ISBN-13: 978- 0-19-857074-5).

[4] R. A. Hulse and J. H. Taylor. Discovery of a pulsar in a binary system. *Astrophys. J.*, 195:L51–L53, 1975.

[5] L. L. Smarr and Blandford R. The binary pulsar: Physical processes, possible companions and evolutionary histories. *Astrophys. J.*, 207:574, 1976.

[6] J. H. Taylor and J. M. Weisberg. A new test of general relativity: Gravitational radiation and the binary pulsar PS R 1913+16. *Astrophys. J.*, 253:908–920, 1982.

[7] P. C. Peters and J. Mathews. Gravitational radiation from point masses in a Keplerian orbit. *Phys. Rev.*, 131:435–439, 1963.

[8] Lee Samuel Finn. The response of interferometric gravitational wave detectors. *Phys. Rev.*, D79:022002, 2009.

[9] H. Wahlquist. THE DOPPLER RESPONSE TO GRAVITATIONAL WAVES FROM A BINARY STAR SOURCE. *Gen. Rel. Grav.*, 19:1101–1113, 1987.

[10] Neil J. Cornish. Alternative derivation of the response of interferometric gravitational wave detectors. *Phys. Rev.*, D80:087101, 2009.

[11] Craig J. Hogan. Big bang nucleosynthesis and the observed abundances of light elements. 1996.

[12] Bruce Allen and Joseph D. Romano. Detecting a stochastic background of gravitational radiation: Signal processing strategies and sensitivities. *Phys. Rev.*, D59:102001, 1999.

[13] Michele Maggiore. Gravitational wave experiments and early universe cosmology. *Phys. Rept.*, 331:283–367, 2000.

[14] Scott A. Hughes, Szabolcs Marka, Peter L. Bender, and Craig J. Hogan. New physics and astronomy with the new gravitational-wave observatories. 2001.

[15] Michael S. Turner. Ten things everyone should know about inflation. 1997.

[16] Tristan L. Smith, Marc Kamionkowski, and Asantha Cooray. Direct detection of the inflationary gravitational wave background. *Phys. Rev.*, D73:023504, 2006.

[17] T. W. B. Kibble. Topology of Cosmic Domains and Strings. *J. Phys.*, A9:1387–1398, 1976.

[18] A. Vilenkin and E. P. Shellard. *Cosmic Strings and Other Topological Defects*. Cambridge University Press, 2000.

[19] R. R. Caldwell, R. A. Battye, and E. P. S. Shellard. Relic gravitational waves from cosmic strings: Updated constraints and opportunities for detection. *Phys. Rev.*, D54:7146–7152, 1996.

[20] Xavier Siemens et al. Gravitational wave bursts from cosmic (super)strings: Quantitative analysis and constraints. *Phys. Rev.*, D73:105001, 2006.

[21] Joey Shapiro Key and Neil J. Cornish. Characterizing the Gravitational Wave Signature from Cosmic String Cusps. *Phys. Rev.*, D79:043014, 2009.

[22] Crescenzo Tortora, E. Piedipalumbo, and V. F. Cardone. Lens modelling and H_0 estimate in quadruply lensed systems. *Mon. Not. Roy. Astron. Soc.*, 354:343–354, 2004.

[23] Allan Sandage. Bias Properties of Extragalactic Distance Indicators XII: Bias Effects of Slope Differences and Intrinsic Dispersion on Tully-Fisher Distances to Galaxy Clusters with Application to the Virgo Cluster. 2007.

[24] A. Dinculescu. A tentative derivation of the main cosmological parameters. *Astrophys. Space Sci.*, 323:289–292, 2009.

[25] S. H. Suyu et al. Dissecting the Gravitational Lens B1608+656. II. Precision Measurements of the Hubble Constant, Spatial Curvature, and the Dark Energy Equation of State. *Astrophys. J.*, 711:201–221, 2010.

[26] Craig J. Copi, David N. Schramm, and Michael S. Turner. Big bang nucleosynthesis and the baryon density of the universe. *Science*, 267:192–199, 1995.

[27] Subir Sarkar. Big bang nucleosynthesis and physics beyond the standard model. *Rept. Prog. Phys.*, 59:1493–1610, 1996.

[28] G. Fiorentini, E. Lisi, Subir Sarkar, and F. L. Villante. Quantifying uncertainties in primordial nucleosynthesis without Monte Carlo simulations. *Phys. Rev.*, D58:063506, 1998.

[29] Latham A. Boyle and Alessandra Buonanno. Relating gravitational wave constraints from primordial nucleosynthesis, pulsar timing, laser interferometers, and the CMB: implications for the early universe. *Phys. Rev.*, D78:043531, 2008.

[30] R. K. Sachs and A. M. Wolfe. Perturbations of a cosmological model and angular variations of the microwave background. *Astrophys. J.*, 147:73–90, 1967.

[31] Edward W. Kolb and Michael S. Turner. The Early universe. *Front. Phys.*, 69:1–547, 1990.

[32] Bruce Allen. The stochastic gravity-wave background: Sources and detection. 1996.

[33] Bruce Allen and Scott Koranda. Temperature fluctuations in the cosmic background radiation from inflationary cosmological models. *Phys. Rev.*, D50:3713, 1994.

[34] S. E. Thorsett and R. J. Dewey. Pulsar timing limits on very low frequency stochastic gravitational radiation. *Phys. Rev.*, D53:3468–3471, 1996.

[35] Frederick A. Jenet et al. Upper bounds on the low-frequency stochastic gravitational wave background from pulsar timing observations: Current limits and future prospects. *Astrophys. J.*, 653:1571–1576, 2006.

[36] Michael S. Turner. Detectability of inflation-produced gravitational waves. *Phys. Rev. D*, 55(2):R435–R439, Jan 1997.

[37] Tristan L. Smith, Marc Kamionkowski, and Asantha Cooray. Direct detection of the inflationary gravitational wave background. *Phys. Rev.*, D73:023504, 2006.

[38] C. Cutler and J. Harms. BBO and the Neutron-Star-Binary Subtraction Problem. *Phys. Rev.*, D73:042001, 2006.

[39] N. Seto, Cornish N. J., and E. S. Phinney. *gr-qc/xxx*, 2005.

[40] Eanna E. Flanagan. The Sensitivity of the laser interferometer gravitational wave observatory (LIGO) to a stochastic background, and its dependence on the detector orientations. *Phys. Rev.*, D48:2389–2407, 1993.

[41] Bruce Allen and Joseph D. Romano. Detecting a stochastic background of gravitational radiation: Signal processing strategies and sensitivities. *Phys. Rev.*, D59:102001, 1999.

[42] S. Phinney and et al. The Big Bang Observer: Direct detection of gravitational waves from the birth of the Universe to the Present. *NASA Mission Concept Study*, 2004.

[43] Thomas A. Prince, Massimo Tinto, Shane L. Larson, and J. W. Armstrong. The LISA optimal sensitivity. *Phys. Rev.*, D66:122002, 2002.

[44] Neil J. Cornish and Jeff Crowder. LISA data analysis using MCMC methods. *Phys. Rev.*, D72:043005, 2005.

[45] Neil J. Cornish and Shane L. Larson. Space missions to detect the cosmic gravitational-wave background. *Class. Quant. Grav.*, 18:3473–3496, 2001.

[46] Carlo Ungarelli and Alberto Vecchio. Studying the anisotropy of the gravitational wave stochastic background with LISA. *Phys. Rev.*, D64:121501, 2001.

[47] Neil J. Cornish. Detecting a stochastic gravitational wave background with the laser interferometer space antenna. *Phys. Rev.*, D65:022004, 2002.

[48] Neil J. Cornish and Ronald W. Hellings. The Effects of orbital motion on LISA time delay interferometry. *Class. Quant. Grav.*, 20:4851–4860, 2003.

[49] Daniel A. Shaddock, Massimo Tinto, Frank B. Estabrook, and J. W. Armstrong. Data combinations accounting for LISA spacecraft motion. *Phys. Rev.*, D68:061303, 2003.

[50] K. M. Gorsky, B. D. Wandelt, E.. Hivon, F. K. Hansen, and A. J. Banday. *http://healpix.jpl.nasa.gov/*.

[51] Curt Cutler. Angular resolution of the LISA gravitational wave detector. *Phys. Rev.*, D57:7089–7102, 1998.

[52] Naoki Seto. Correlation analysis of stochastic gravitational wave background around 0.1-Hz - 1-Hz. *Phys. Rev.*, D73:063001, 2006.

[53] John David Jackson. *Classical Electrodynamics Third Edition*. John Wiley & Sons, Inc, 1999.

[54] Sean M. Carroll. Spacetime and geometry: An introduction to general relativity. San Francisco, USA: Addison-Wesley (2004) 513 p.

[55] F. L. Estabrook and H. D. Wahlquist. *General Relativity and Gravitation*, 6:439, 1975.

[56] M. V. Sazhin. *Sov. Astron.*, 22:36, 1978.

[57] Steven L. Detweiler. Pulsar timing measurements and the search for gravitational waves. *Astrophys. J.*, 234:1100–1104, 1979.

[58] R. W. Hellings and G. S. Downs. UPPER LIMITS ON THE ISOTROPIC GRAVITATIONAL RADIATION BACKGROUND FROM PULSAR TIMING ANALYSIS. *Astrophys. J.*, 265:L39–L42, 1983.

[59] R. S. Foster and D. C. Backer. *Astrophys. J.*, 361:300, 1993.

[60] F. Jenet et al. The North American Nanohertz Observatory for Gravitational Waves. 2009.

[61] R. D. Ferdman et al. The European Pulsar Timing Array: current efforts and a LEAP toward the future. *Class. Quant. Grav.*, 27:084014, 2010.

[62] J. P. W. Verbiest et al. Status Update of the Parkes Pulsar Timing Array. *Class. Quant. Grav.*, 27:084015, 2010.

[63] R. N. Manchester. Detection of Gravitational Waves using Pulsar Timing. 2010.

[64] P. Hall. The square kilometre array: An international engineering perspective. In Peter Hall, editor, *The Square Kilometre Array: An Engineering Perspective*, pages 5–16. Springer Netherlands, 2005. 10.1007/1-4020-3798-8_2.

[65] Chris L. Carilli and S. Rawlings. Science with the Square Kilometer Array: Motivation, Key Science Projects, Standards and Assumptions. 2004.

[66] Fredrick A. Jenet, George B. Hobbs, K. J. Lee, and Richard N. Manchester. Detecting the stochastic gravitational wave background using pulsar timing. *Astrophys. J.*, 625:L123–L126, 2005.

[67] George Hobbs. Pulsars as gravitational wave detectors. 2010.

[68] G. Hobbs et al. The international pulsar timing array project: using pulsars as a gravitational wave detector. *Class. Quant. Grav.*, 27:084013, 2010.

[69] J. P. W. Verbiest et al. Precision timing of PSR J0437-4715: an accurate pulsar distance, a high pulsar mass and a limit on the variation of Newton's gravitational constant. 2008.

[70] J. P. W. Verbiest, M. Bailes, W. A. Coles, G. B. Hobbs, W. van Straten, D. J. Champion, F. A. Jenet, R. N. Manchester, N. D. R. Bhat, J. M. Sarkissian, D. Yardley, S. Burke-Spolaor, A. W. Hotan, and X. P. You. Timing stability of millisecond pulsars and prospects for gravitational-wave detection. *MNRAS*, 400:951–968, December 2009.

[71] K. S. Thorne and V. B. Braginskii. Graviational-wave bursts from the nuclei of distant galaxies and quasars - proposal fro detection using doppler tracking of interplanetary spacecraft. *Astrophys. J.*, 204:L1–L6, 1976.

[72] Motohiro Enoki and Masahiro Nagashima. The effect of orbital eccentricity on gravitational wave background radiation from cosmological binaries. *Prog.Theor.Phys.*, 117:241–256, 2007.

[73] Bence Kocsis, Merse E. Gaspar, and Szabolcs Marka. Detection Rate Estimates of Gravity-waves Emitted During Parabolic Encounters of Stellar Black Holes in Globular Clusters. *Astrophys. J.*, 648:411–429, 2006.

[74] Thibault Damour and Alexander Vilenkin. Gravitational wave bursts from cusps and kinks on cosmic strings. *Phys. Rev.*, D64:064008, 2001.

[75] Mohan Rajagopal and Roger W. Romani. Ultralow frequency gravitational radiation from massive black hole binaries. *Astrophys. J.*, 446:543–549, 1995.

[76] J. Stuart B. Wyithe and Abraham Loeb. Low-frequency gravitational waves from massive black hole binaries: Predictions for LISA and pulsar timing arrays. *Astrophys. J.*, 590:691–706, 2003.

[77] Andrew H. Jaffe and Donald C. Backer. Gravitational waves probe the coalescence rate of massive black hole binaries. *Astrophys. J.*, 583:616–631, 2003.

[78] Motohiro Enoki, Kaiki T. Inoue, Masahiro Nagashima, and Naoshi Sugiyama. Gravitational waves from supermassive black hole coalescence in a hierarchical galaxy formation model. *Astrophys. J.*, 615:19, 2004.

[79] Ryo Saito and Jun'ichi Yokoyama. Gravitational wave background as a probe of the primordial black hole abundance. *Phys. Rev. Lett.*, 102:161101, 2009.

[80] F. D'alessandro. Rotational irregularities in pulsars a review. *Astrophysics and Space Science*, 246:73–106, 1996. 10.1007/BF00637401.

[81] G. Hobbs, A. G. Lyne, and M. Kramer. An analysis of the timing irregularities for 366 pulsars. 2009.

[82] Andrew Lyne, George Hobbs, Michael Kramer, Ingrid Stairs, and Ben Stappers. Switched magnetospheric regulation of pulsar spin-down. 2010.

[83] Alexander E. Rodin. The optimal filters for the construction of the ensemble pulsar time. *Mon. Not. Roy. Astron. Soc.*, 387:1583–1588, 2008.

[84] M. S. Pshirkov and A. V. Tuntsov. Local constraints on cosmic string loops from photometry and pulsar timing. *Phys. Rev.*, D81:083519, 2010.

[85] Richard Battye and Adam Moss. Updated constraints on the cosmic string tension. *Phys. Rev.*, D82:023521, 2010.

[86] Fredrick A. Jenet, Andrea Lommen, Shane L. Larson, and Linqing Wen. Constraining the properties of the proposed supermassive black hole system in 3c66b: Limits from pulsar timing. *Astrophys. J.*, 606:799–803, 2004.

[87] Hiroshi Sudou, Satoru Iguchi, Yasuhiro Murata, and Yoshiaki Taniguchi. Orbital Motion in the Radio Galaxy 3C 66B: Evidence for a Supermassive Black Hole Binary. *Science*, 300:1263, 2003.

[88] D. R. Stinebring, M. F. Ryba, Joseph H. Taylor, and R. W. Romani. THE COSMIC GRAVITATIONAL WAVE BACKGROUND: LIMITS FROM MILLISECOND PULSAR TIMING. *Phys. Rev. Lett.*, 65:285–288, 1990.

[89] A. N. Lommen. New limits on gravitational radiation using pulsars. 2002.

[90] Melissa Anholm, Stefan Ballmer, Jolien D. E. Creighton, Larry R. Price, and Xavier Siemens. Optimal strategies for gravitational wave stochastic background searches in pulsar timing data. *Phys. Rev.*, D79:084030, 2009.

[91] Rutger van Haasteren, Yuri Levin, Patrick McDonald, and Tingting Lu. On measuring the gravitational-wave background using Pulsar Timing Arrays. 2008.

[92] A. Sesana, A. Vecchio, and M. Volonteri. *MNRAS*, 394:2255, 2009.

[93] D. R. B. Yardley et al. The Sensitivity of the Parkes Pulsar Timing Array to Individual Sources of Gravitational Waves. 2010.

[94] A. Sesana and A. Vecchio. Gravitational waves and pulsar timing: stochastic background, individual sources and parameter estimation. *Class. Quant. Grav.*, 27:084016, 2010.

[95] Alberto Sesana and Alberto Vecchio. Measuring the parameters of massive black hole binary systems with Pulsar Timing Array observations of gravitational waves. *Phys. Rev.*, D81:104008, 2010.

[96] Ryuichi Takahashi and Naoki Seto. Parameter estimation for Galactic binaries by LISA. *Astrophys. J.*, 575:1030–1036, 2002.

[97] R. W. Hellings. SPACECRAFT DOPPLER GRAVITY WAVE DETECTION. 1. THEORY. *Phys. Rev.*, D23:832–843, 1981.

[98] R. W. Hellings. ELECTROMAGNETICALLY TRACKED FREE MASS GRAVITATIONAL WAVE ANTENNAS. 1982. In *Les Houches 1982, Proceedings, Gravitational Radiation*, 485-493.

[99] E. S. Phinney. A practical theorem on gravitational wave backgrounds. 2001.

[100] A. Sesana, A. Vecchio, and C. N. Colacino. *MNRAS*, 390:192, 2008.

[101] R. N. Manchester. The Parkes Pulsar Timing Array. *AIP Conf. Proc.*, 983:584–592, 2008.

[102] Alberto Sesana, Marta Volonteri, and Francesco Haardt. The imprint of massive black hole formation models on the LISA data stream. *Mon. Not. Roy. Astron. Soc.*, 377:1711–1716, 2007.

[103] Marta Volonteri, Francesco Haardt, and Piero Madau. The Assembly and Merging History of Supermassive Black Holes in Hierarchical Models of Galaxy Formation. *Astrophys. J.*, 582:559–573, 2003.

[104] Savvas M. Koushiappas, J. S. Bullock, and A. Dekel. Massive black hole seeds from low angular momentum material. *Mon. Not. Roy. Astron. Soc.*, 354:292, 2004.

[105] Mitchell C. Begelman, Marta Volonteri, and Martin J. Rees. Formation of Supermassive Black Holes by Direct Collapse in Pregalactic Halos. *Mon. Not. Roy. Astron. Soc.*, 370:289–298, 2006.

[106] Marta Volonteri, Ruben Salvaterra, and Francesco Haardt. Constraints on the Accretion History of Massive Black Holes from Faint X-ray Counts. *Mon. Not. Roy. Astron. Soc.*, 373:121–127, 2006.

[107] N. Metropolis, A. W. Rosenbluth, M. N. Rosenbluth, A. H. Teller, and E. Teller. Equation of state calculations by fast computing machines. *J. Chem. Phys.*, 21:1087–1092, 1953.

[108] W. K. Hastings. *Biometrika*, 57:97, 1970.

[109] M. Newman and G. Barkema. *Monte Carlo Methods in Statistical Physics*. Oxford University Press Inc., 1999.

[110] D. Gamerman. *Markov Chain Monte Carlo: Stochastic Simulation of Bayesian-Inference*. Chapman & Hall London, 1997.

[111] Robert H. Swendsen and Jian-Sheng Wang. Replica monte carlo simulation of spin-glasses. *Phys. Rev. Lett.*, 57(21):2607–2609, Nov 1986.